UNIVERSIDAD DE CHILE
FACULTAD DE CIENCIAS FÍSICAS Y MATEMÁTICAS
DEPARTAMENTO DE GEOLOGÍA

PHYSICO-CHEMICAL AND ENVIRONMENTAL CONTROLS ON SILICEOUS SINTER FORMATION AT THE HIGH-ALTITUDE EL TATIO GEOTHERMAL FIELD, NORTHERN CHILE

TESIS PARA OPTAR AL GRADO DE MAGÍSTER EN CIENCIAS, MENCIÓN GEOLOGÍA

MEMORIA PARA OPTAR AL TÍTULO DE GEÓLOGO

CONSTANZA BEATRIZ NICOLAU DEL ROURE EYLERTS

PROFESOR GUÍA:
MARTIN REICH MORALES

PROFESOR CO-GUÍA:
BRIDGET Y. LYNNE

MIEMBROS DE LA COMISIÓN:
DIEGO MORATA CÉSPEDES
JACOBUS LE ROUX

SANTIAGO DE CHILE
2013

RESUMEN

Los depósitos de sínter silíceo son rocas formadas por la evaporación y enfriamiento de aguas termales alcalinas cloruradas, de pH cercano a neutro y ricas en sílice disuelta. Las texturas y morfología que muestran estos depósitos están fuertemente influenciadas por las condiciones ambientales de formación, y por las características hidrodinámicas del agua termal. La ocurrencia en superficie de depósitos sínter revela la existencia de sistemas hidrotermales de alta temperatura en profundidad, y, por lo tanto, su estudio se relaciona a la exploración geotérmica y mineral. A pesar de que actualmente existen numerosos proyectos de exploración en la Zona Volcánica Central de Los Andes, poco se han estudiado las características particulares de los depósitos de sínter que se han formado en este ambiente. El campo geotermal El Tatio, que se ubica en el Altiplano del norte de Chile, a gran elevación, se caracteriza por presentar condiciones climáticas extremas (gran oscilación térmica y alta tasa de evaporación) y una geoquímica de aguas termales particular (alta concentración de sílice disuelta, arsénico y boro). Estas características hacen que El Tatio sea un lugar ideal para estudiar la influencia de las condiciones ambientales y la geoquímica de aguas termales sobre las características de los sínteres silíceos.

En el presente estudio se presentan análisis de laboratorio (ICP-OES, ICP-MS, SEM and DRX) y mediciones en terreno, las características mineralógicas, químicas y texturales de los depósitos de sínter silíceo de El Tatio, y las características hidrodinámicas de las aguas termales a partir de las cuales ellos se forman. Adicionalmente, se desarrolla un experimento *in situ* para estimar la tasa de precipitación de sílice en El Tatio.

Los sínteres silíceos de El Tatio están formados principalmente por micro- y nano-esferas de ópalo-A, y presentan un alto grado de desorden estructural, evidenciado por altos valores de FWHM (7.8-12.5 °2ϴ), que se atribuye a la incorporación de cationes como Ca^{2+} y Na^+ en su estructura. Otras fases cristalinas, como la halita y el yeso, también son comunes en El Tatio. Minerales de calcio y arsénico, como la cahnita, ocurren como relleno de cavidades y formando laminaciones continuas dentro del sínter. La ocurrencia de estas fases minerales se debe a la alta concentración de elementos como boro, arsénico y calcio en las aguas termales, y su formación se relaciona con la formación de los sínteres silíceos a través de procesos de evaporación total. Los depósitos de sínter de El Tatio se caracterizan también por presentar texturas asociadas a temperaturas bajo cero, y relacionadas a las condiciones hidrodinámicas y a la temperatura del flujo de agua termal.

Estas características contrastan con las de los sínteres formados a baja elevación, lo que resalta la importancia de comprender el origen de la mineralogía y texturas particulares de los sínteres formados a alta elevación para poder utilizarlos exitosamente como herramienta de exploración. El estudio integrativo de los sínteres formados en campos geotermales activos del norte de Chile, que incluya tanto la caracterización mineralógica y textural de los depósitos, como la caracterización de las aguas termales y la estimación de tasas de precipitación de sílice, proporciona nuevos conocimientos acerca de los procesos que influyen en la formación de los depósitos de sínter silíceo en el contexto andino.

ABSTRACT

Siliceous sinter deposits are hot spring rocks formed by evaporation and cooling of alkali-chloride, near-neutral and silica-saturated thermal waters. Sinter textures and morphology are greatly influenced by the environmental conditions and the hydrological characteristics of the thermal water flow. Sinter deposits reveal the presence of a high temperature hydrothermal reservoir at depth, and therefore are commonly used in geothermal and ore exploration. Despite the fact that there is active geothermal exploration in the andean Central Volcanic Zone, the characteristics of siliceous sinter deposits formed under the particular environmental conditions of this location have been understudied. The El Tatio Geothermal Field is located in the Altiplano of northern Chile, at high altitude and exposed to severe climatic conditions (high atmospheric thermal variability and high evaporation rate), and the thermal water that discharge there show high concentration of dissolved silica, arsenic and boron. Thus, the El Tatio geothermal field is an ideal setting to study the influence of the environmental conditions and chemical characteristics of thermal waters over the characteristics of the siliceous sinter deposits.

This study characterizes the mineralogy, chemistry and textures of El Tatio sinters and the hydrodynamics of thermal waters trough field measurements and laboratory determinations (ICP-OES, ICP-MS, SEM and XRD). Additionally, an experiment was developed at the site of study, to determine the silica precipitation rate at El Tatio.

The El Tatio sinters are mainly constituted by micro- and nano-scale opal-A spheres, and show a very low degree of structural order (FWHM vary from 7.8 to 12.5 °2Θ), possibly due to the incorporation of cations, such as Ca^{2+} and Na^+, into the sinter structure. Crystalline phases are common in the El Tatio sinters, especially halite and gypsum. Calcium and arsenic-rich minerals, some of which correspond to an arsenic borate called cahnite, are found filling cavities and constituting laminations within the sinter deposits. The occurrence of these accessory mineral phases is related to the high concentration of boron, arsenic and calcium in the discharging thermal water, and their formation is possible due to the sinter formation process through evaporation to dryness. Some of the distinctive macro- and micro-textures identified in El Tatio sinters are related to environmental conditions, particularly sub-zero temperatures, while others are linked exclusively to water temperature and hydrodynamics.

These characteristics contrast with those of low-altitude sinters, and highlight the importance of understanding the origin of the particular mineralogical and textural characteristics of Andean sinters to successfully use them in geothermal exploration. The integrative study of siliceous sinter deposits at active geothermal fields of northern Chile, that includes mineralogical and textural determinations along with thermal water characterization and experimental silica precipitation rate measurements, provides new insights about the nature of siliceous sinter formation in the andean context.

AGRADECIMIENTOS

Al terminar este largo proceso de equivocaciones y aprendizaje que ha sido mi paso por la universidad, no puedo dejar de recordar a quienes han hecho que valga la pena levantarme cada día, a los responsables de que me interesara la ciencia desde el principio, y a quienes me enseñaron que nada es imposible.

En primer lugar quisiera agradecer a mi familia, por enseñarme que la constancia y el esfuerzo pueden lograr muchas cosas, por apoyarme en todo, y por aguantarme en los momentos de estrés, que fueron varios. A mi mamá, por su preocupación diaria y por hacerme sentir bien cuando me pongo pesimista. A mi papá, por su paciencia al enseñarme, y por su cariño incondicional. A mis hermanos por estar siempre ahí para mí. Katy, no sabes cuánto te admiro. Edu, eres el mejor hermano chico.

A quienes me han acompañado todos estos años, desde chica, Javi, Clau, Conti, Pai, gracias por sus colapsos y su alegría, Ángeles, Lucía, Nicole, gracias por enseñarme a disfrutar la vida todos los días. A mis amigos de plan común, en especial a la Kimi y la Babi, por convertirse en amigas de la vida. A los que estuvieron en los terrenos y las clases en geología, especialmente a Pipe, Pancha, Estrella, Cata, Nati, Manena. A los que conocí en el postgrado, Pame, Monse, Eduardo, Pablo, Alida, Feña Soto, Diego, Tapia, Pita, Viole, Anneli, Oscar, Dani, Fofito, Checho, gracias por mostrarme lo lindo de la ciencia y la investigación, en especial a la Feña Alvarez, por su paciencia. A todos los que de alguna manera son responsables de que mis años en la Universidad de Chile fueran enriquecedores tanto académicamente como en lo personal, a los que cambiaron mi visión de la sociedad y del rol que quiero cumplir en ella.

A mis profesores, que fueron fuente de inspiración. A mi profesor guía, Martin Reich, a quien agradezco su confianza en este proyecto que surgió tan repentinamente, y por su dedicación. A mi profesora co-guía, Bridget Lynne, por confiar en mí, por su rigurosidad científica y por acogerme tan cariñosamente durante mi pasantía en Nueva Zelanda. Al grupo de geoquímica por la constante discusión científica. A quienes me acompañaron en terreno en El Tatio, Oscar, Feña Soto, Feña Álvarez, y en especial a Pablo, sin ti este proyecto no habría nacido. A los miembros de la comisión, Jacobus Le Roux y Diego Morata, gracias por sus comentarios y su disposición a mejorar este trabajo. Y por último, quisiera reconocer a las instituciones participaron en este proyecto: a CONICYT por el financiamiento del arancel a través de su Beca de Magíster, al Centro de Excelencia en Geotermia de los Andes (FONDAP - CEGA), por el financiamiento de esta tesis y de mi pasantía, al Insitute of Earth Sciences and Engineering y la University of Aukland.

Finalmente, quiero agradecer a mi compañero de vida. Cristóbal, gracias por hacer que mi pesimismo se desvanezca, por hacerme reír, y por tu infinita paciencia.

TABLE OF CONTENTS

iii

iv

CHAPTER I INTRODUCTION

The western border of South America has been a convergent margin since Jurassic times (e.g. Coira *et al.*, 1982), where Nazca plate subducts beneath the South American plate. This regime cause volcanic activity primarily expressed along successive volcanic arcs as the one located nowadays along The Andes, generating an increased geothermal gradient linked to the development of geothermal systems near the modern volcanic arc (Lahsen, 1976; Hauser, 1997).

The energy potential related to geothermal systems in Chile is estimated in the order of 16,000 MW for 50 years, based on the existence of fluids at temperatures greater than 150 °C trapped at less than 3 km of depth (Lahsen, 1986). The main geothermal systems identified in northern Chile are Surire, Puchuldiza, Pampa Lirima, Irruputunco, Apacheta and El Tatio (Figure 1). Among these, the El Tatio geothermal field was the first to be explored for geothermal energy. Two exploration wells were drilled in El Tatio between 1969 and 1971, finding thermal fluids at 263 °C at 800 m depth (Lahsen and Trujillo, 1975).Based on this finding, the energy potential for this particular system has been estimated between 100 and 400 MW (Lahsen, 1988; Huttrer, 1995), although this field is not currently in exploration or exploitation and has been recently declared National Monument. Siliceous sinter deposits are a common feature in this particular geothermal field, covering a large area around the thermal springs.

Siliceous sinters are hot spring deposits composed of one or more silica phases that may include opal-A, opal-A/CT, opal-CT, opal-C, chalcedony, moganite and quartz, although the initial phase is always opal-A (Herdianita *et al.*, 2000; Campbell *et al.*, 2001; Lynne *et al.*, 2003; Lynne and Campbell, 2004; Rodgers *et al.*, 2004; Lynne *et al.*, 2005, 2006, 2007b, 2008; García-Valles *et al.*, 2008). The subsequent and more mature phases are formed by post-depositional diagenesis, which is not time-dependent and is greatly influenced by heat, fluid circulation and burial (e.g. Lynne and Campbell, 2004; Lynne *et al.*, 2008).Accessory minerals such as halite, sylvite, calcite, native sulphur, cinnabar and pyrite, and biological, lithic or mineral detritus can also be present in

minor quantities (García-Valles *et al.*, 2008; Tobler *et al.*, 2008; Handley *et al* 2005; Hampton *et al.*, 2004).
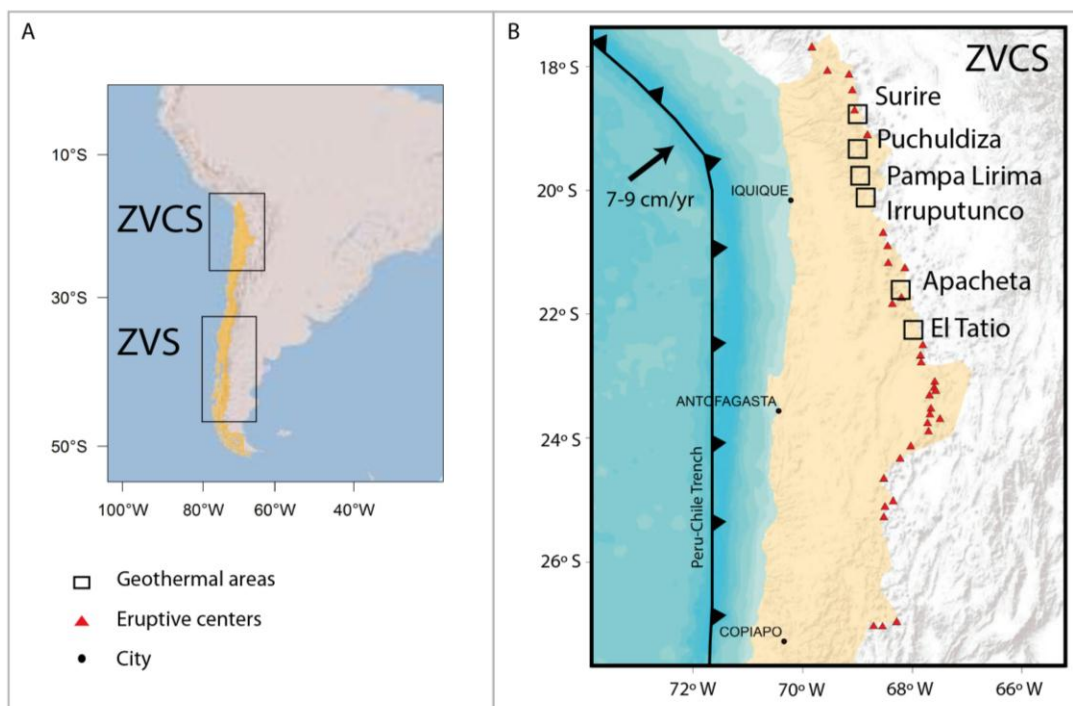
Figure 1. Main geothermal areas of Chile. A: Southern Central Volcanic Zone (ZVCS) and Southern Volcanic Zone location (ZVS) in Chile. B: Main eruptive centers and geothermal areas in nothern Chile. (Modified from Aravena and Lahsen, 2013)

Siliceous sinter form by evaporation and cooling processes, leading to oversaturation and precipitation of amorphous silica from silica-rich near neutral pH thermal waters (e.g. Jones *et al.*, 2000; Guidry and Chafetz, 2003; Mountain *et al.*, 2003; Tobler *et al.*, 2008; Schinteie *et al.*, 2007). This precipitation results in the development of macroscopic features near and around thermal water discharges, including geyser mounds, sinter terraces, pool rims and discharge aprons (e.g. Cady and Farmer, 1996; Lowe *et al.*, 2001; Guidry and Chafetz, 2003b; Lynne and Campbell, 2003; Lynne, 2012). Other siliceous deposits are found around acidic springs, these deposits are referred to as silica residue. They form by *in situ* re-precipitation of silica originated by dissolution of silicate rocks due to steam condensate acidified by sulfuric acid (White *et al.*, 1956, Rodgers *et al.,* 2004).

Sinter deposits are common in modern geothermal fields around the world where silica is currently depositing, such as the Old Faithful geyser in Yellowstone, U.S.A., Champagne Pool in Waiotapu, New Zealand and the El Jefe geyser at El Tatio, Chile. There are also examples of older sinters related to ancient hydrothermal activity such as the Paleozoic Rhynie chert in Scotland (Trewin, 1994 and Rice *et al.*, 1995), the Devonian to Carboniferous Drummond Basin sinters in Australia (Walter *et al.*, 1996), the Jurassic sinter in Argentina (Guido and Campbell, 2011), the Pleistocene Steamboat Springs sinters from Nevada, U.S.A. (11,493 ± 70 yrs; Lynne *et al.*, 2008), and the recent Opal Mound sinters from Utah, USA (1,920 ± 160 and 1,630 ± 90 yrs; Lynne *et al.*, 2005).

These deposits record environmental and hydrological conditions at the moment of their formation, along with the attributes of the biological population that thrives in thermal springs(Walter, 1976; Cady and Farmer, 1996; Hinman and Lindstrom, 1996;Konhauser and Ferris, 1996, Jones *et al.*, 1997; Jones *et al.*, 1998; Campbell *et al.*, 2001, Konhauser *et al.*, 2001, Lowe *et al.*, 2001, Jones *et al.*, 2002; Guidry and Chafetz, 2003b; Lynne and Campbell, 2003 and Handley *et al*, 2005). Therefore, the study of sinter deposits can also contribute to understand the development of life in extreme environments, and thus the origin of life in Earth (e.g. Konhauser *et al.*, 2003).They are also of interest in an astrobiological context, considering recent evidence suggesting hydrothermal activity and solphatara-like environments on Mars (e.g., Farmer 1996, 2000; McCollom and Hynek 2005). In addition, rocks with coatings of amorphous silica have been identified via thermal IR spectroscopy on Mars surface (Kraft *et al.*, 2003; Michalski *et al.*, 2005). This has been porposed as an indicator of past aqueous activity on Mars, and one interpretation is that they formed under hydrothermal conditions akin to sinters formed by hot springs on Earth (Squyres *et al.*, 2008; Preston and Genge, 2010).

In general, the presence of extensive siliceous sinter deposits reveals the existence of a geothermal system at more than 175 °C at depth (Fournier and Rowe, 1966), and may be related to the occurrence of epithermal ore deposits (White *et al.*, 1992; Fournier *et al.*, 1994: Nicholson, 1988; Herdianita *et al.*, 2000; Guido *et al.*, 2002; Pirajno,

2010).Therefore, active and historic siliceous sinter deposits can be used as tracers for high-temperature geothermal systems.

The Andean Central Volcanic Zone has active exploration for hydrothermal deposits and energy resources, but the characteristics of siliceous sinter deposits formed under the particular environmental conditions of this location have been understudied. Thus, the understanding of eventual particularities in the mineralogy and textures of high-altitude Andean siliceous sinters is crucial to successfully use them in geothermal exploration

The El Tatio Geothermal Field is located in the Altiplano of northern Chile, at high altitude and exposed to severe climatic conditions. It presents numerous thermal features, including fumaroles, geysers, hot springs, hot pools, boiling pools, mud pools and sinter deposits, covering an area of more than 100 km². Previous studies propose that siliceous sinter deposits found at El Tatio are mainly composed by opal-A and opal-CT (Fernández-Turiel *et al.*, 2005, García-Valles *et al.*, 2008), but the presence of rare boron and arsenic minerals such as sassolite [H_3BO_3], nobleite [$CaB_6O_{10}\cdot4H_2O$], realgar [AsS] and teruggite [$Ca_4MgAs_2B_{12}O_{22}(OH)_{12}\cdot12(H_2O)$] is also reported (García-Valles *et al.*, 2008).

Thermal waters that discharge at El Tatio are near neutral pH, alkali-chloride and display high concentrations of silica (up to 102 mg/l; Tassi *et al.*, 2010), arsenic (up to 60mmol/l), boron(up to 17mmol/l) and antimony (up to 34μmol/l)(Landrum *et al.*, 2009).Despite the fact that numerous studies have studied the aqueous and gas geochemistry of El Tatio features (e.g. Cusicanqui *et al.*,1975; and Giggenbach, 1978;Cortecci *et al.*, 2005; Tassi *et al.*, 2005, 2010) few works have focused on the sinter deposits (Glennon and Pfaff, 2003; Jones and Renaut, 1997; Fernández-Turiel *et al.*, 2005; García-Valles *et al.*, 2008). Thus, little is known about the physico-chemical factors that control silica precipitation and accumulation in high-altitude systems.

This study reports new mineralogical and geochemical data of the high-altitude siliceous sinter deposits from the El Tatio geothermal field. This work aims at: (1)

4

providing constraints on the development of siliceous sinter deposits in the Andean context, and (2) understanding the effects of high altitude, high solar radiation, extreme climatic conditions and high concentration of elements such as As, B, Sb in waters over the morphology, chemistry, silica phases and textures present in the associated siliceous sinter deposits. The main objective of this work is to determine the relation between environmental conditions and physico-chemical characteristics of the thermal fluids with the chemical composition, mineralogy and textures of siliceous sinter deposits at the El Tatio geothermal field.

This study proposes that physic-chemical characteristics of thermal waters, such as temperature, pH and chemical composition, have an impact over the mineralogy and chemical composition of the associated siliceous sinter deposits, and that environmental conditions and hydrodynamic characteristics of water discharge are reflected in the sinter textures. Specific objectives for this study are: (1) characterize the selected siliceous sinter deposits in terms of their chemical composition, mineralogy and textures, (2) characterize the thermal waters associated to sinters, in terms of their physico-chemical and hydrodynamic features and, (3) compare and contrast the sinter chemical and mineralogical characteristics with water compositions, (4) correlate the hydrodynamic and environmental conditions of surface waters with the resulting sinter textures, (5) provide an estimation of silica precipitation rates at El Tatio, (6) compare El Tatio sinter textures, chemistry and mineralogy with those of other lower altitude sinters in New Zealand and Yellowstone.

I.1. Study area

The El Tatio geothermal field (22°20'S y 68°W) is located at 4.270 meters above mean sea level, 95 km east of the town of Calama, in the El Loa Province, Antofagasta Region, northern Chile. The main access routes are B-245 from San Pedro de Atacama, and, from Calama, route CH-21 to Chiu Chiu and then routes B-169, B-159 and B-245 (Figure 2).

The climate in this area is characterized by low precipitation (<100 mm/year). Rainfall is particularly seasonal, because this area is under the influence of the South American Summer Monsoon, with rains occurring from November to March (Zhou and Lau, 1998) and particularly focused from December to March (Fernández-Turiel *et al.*, 2005). The mean annual temperature ranges from 8 to 11 °C. Daily temperature variation reaches 35 °C. In winter the temperature can fall to -30 °C (Fernández-Turiel *et al.*, 2005).
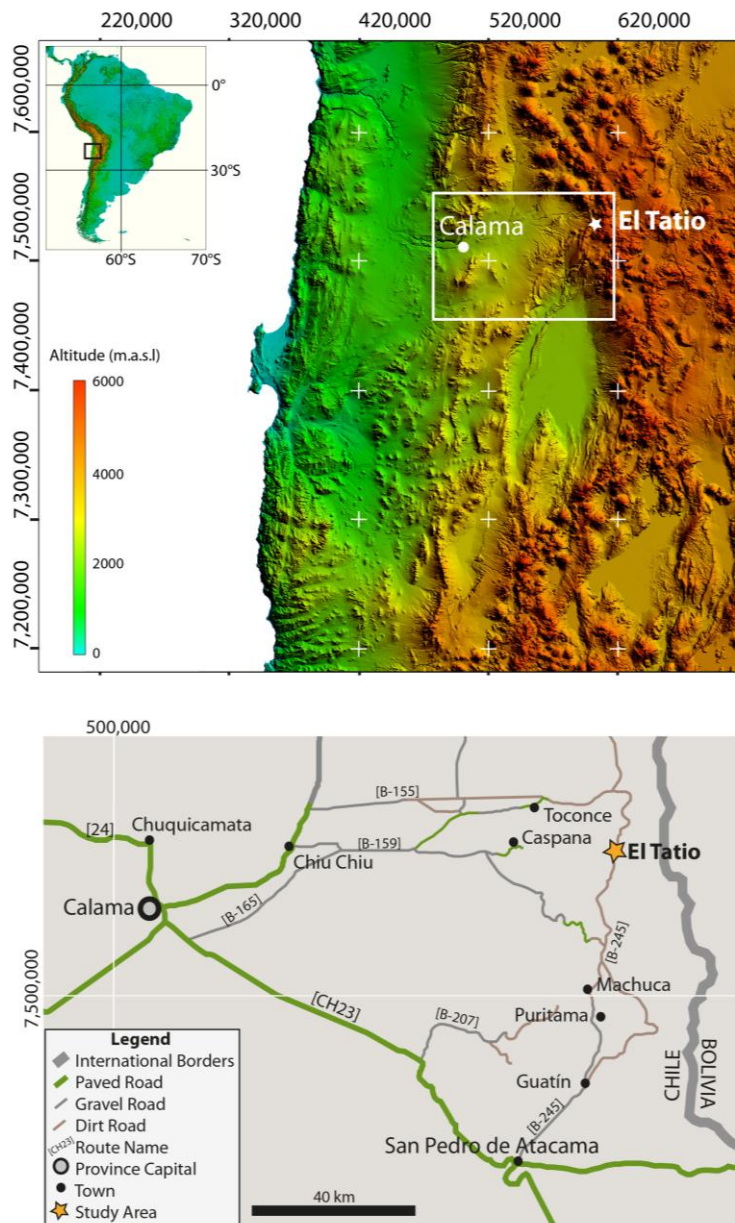
Figure 2. Study site location. The upper image shows the location of the study site in a regional context. The white case shows the area of the map below. The lower image shows the location of main towns and cities close to the study area, and the access routes to El Tatio.

CHAPTER II   METHODS

In this study, five selected sites at El Tatio are described in terms of the physico-chemical/hydrodynamic characteristics of thermal waters and their associated siliceous sinter deposits. Sinter and water samples were collected and analyzed using a variety of techniques, in order to determine their chemical composition, mineralogy and textures (Figure 3). At each site, water temperature and pH were measured, and water samples were collected and analyzed in terms of their major, minor and trace element composition.
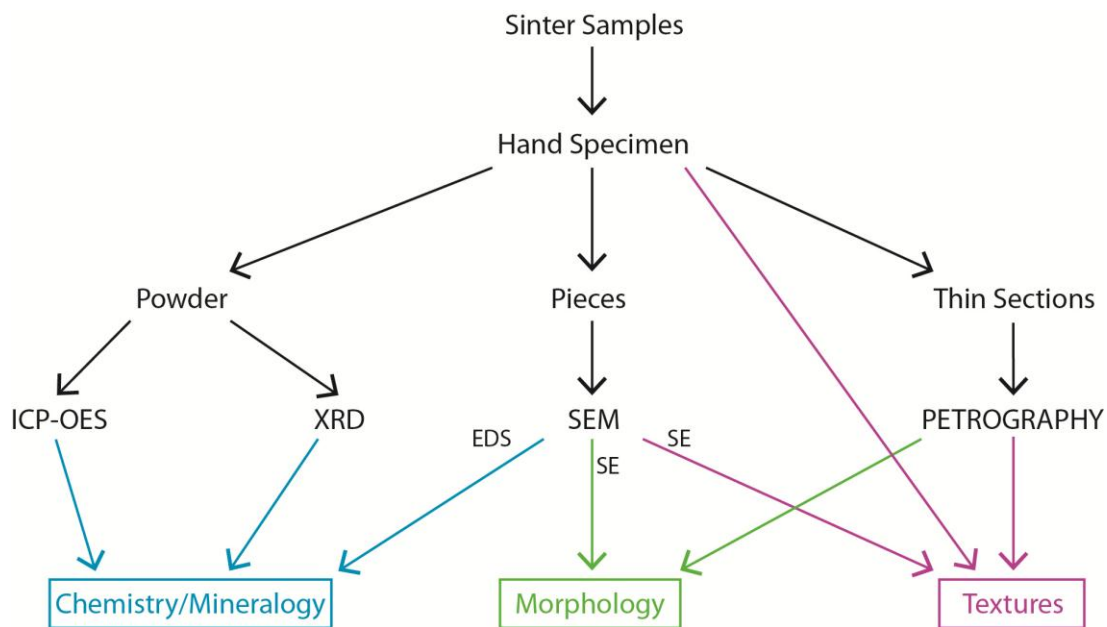
Figure 3. Flow diagram of the protocols followed for the determination of sinter chemistry, mineralogy, morphology and textures. ICP-OES: Inductively Coupled Plasma-Optical Emission Spectrometry, XRD: X-Ray Diffraction, SEM: Scanning Electron Microscopy, EDS: Energy-Dispersive X-ray Spectroscopy, SE: Secondary Electrons.

II.1.Macroscopic characterization of sinter textures

Sinter depositional textures were identified and described first at a macroscopic scale for each sample. Some samples were cut with a diamond saw to examine the inside of columns or surfaces transverse to laminations. The specific terms used to describe sinter textures were taken from references and are defined in CHAPTER III.

II.2.   Petrography of sinter samples

Polished thin sections were made from each sinter sample at the Geology Department at Universidad de Chile. The direction towards the surface or the center of the pool was logged when appropriate. Thin sections were inspected under an Olympus CX51 polarizing microscope to identify sinter textures and determine the presence of minerals and/or lithic material. Photographs were taken using the MShotCO-90 software.

II.3.   Scanning Electron Microscopy (SEM) of sinter samples

Before SEM observation, sinter hand samples were washed using tap water, dried at ambient temperature, broken into millimeter- to centimeter-scale pieces, and mounted on aluminum stubs using epoxy. This procedure was followed to obtain a fresh irregular surface suitable for identifying silica phases and textures under SEM.

One set of samples was coated with a platinum layer and then examined using a FEI Quanta 200 F Field-Emission-Gun SEM, equipped with an EDS SiLi Detector (Lithium drifted) with a Super Ultra-Thin Window, at the Earth and Materials Science Department, University of Auckland, New Zealand. The other set of samples were coated with a gold layer and examined using a FEI Quanta 200 MK2 SEM, at the Universidad de Chile, Chile.

In both cases, secondary electron (SE) detection was used to obtain topographic images of the fresh sample surface, in order to recognize the morphology of silica and other mineral phases, and their textural relationships. Energy-dispersive X-ray spectrometry (EDS) was used to determine the main chemical components of mineral phases. SEM data was obtained with the support of Catherine Hobbis at the University of Auckland and Christian Nievas at Universidad de Chile.

II.4.   X-Ray Diffraction (XRD) analysis of sinter samples

For silica phase determination of sinter samples, dry samples were grounded in a mortar and pestle and scanned at 0.6 °2ɵ/min, with a step size of 0.01 °, from 10 to 40 °2ɵ, in a Phillips Diffractometer model PW1130/00, at the University of Auckland, New Zealand. Operating conditions were 40 kV and 20 mA, using CuKα radiation (λα = 1.54051 Å). Following the methods in Lynne (2007), XRD traces were not electronically manipulated; for each sample the Full Width at Half Maximum (FWHM) was measured fitting the curve and base line manually.

In order to detect the presence of other mineral phases, the same samples were scanned with a step size of 0.02°, a time of 3 seconds, and from 2 to 80 °2ɵ. These additional XRD analyses were carried out in a Siemens Diffractometer model D-5000, in the Physics Department of the Universidad de Chile, and the conditions were 40 kV and 30mA. The identification of mineral phases was undertaken using MacDiff4.2.6 and The American Mineralogist Crystal Structure Database (Downs and Hall-Wallace, 2003).

II.5.   Chemical analysis of sinter samples

The analyzed samples using XRD were sent to Activation Labs Ltd. in Canada for bulk chemical analysis. The sample weight was insufficient to analyze duplicates. The detection limits of each element vary and are shown in APPENDIX I.

Sulphur determination was attained through Combustion Infrared Detection method. Accelerator material was added to a 0.2 g sample. The inductive elements of the sample and accelerator couple with the high frequency field of the induction furnace. The pure oxygen environment and the heat generated by this coupling cause the sample to combust. During combustion, sulphur-bearing elements are reduced, releasing sulphur, which binds with oxygen to form SO_2. Sulphur is then measured as sulphur dioxide in the infrared cell. An Eltra CS-800 was used for analysis.

Boron content measurement was attained using the Prompt Gamma Neutron Activation Analysis (PGNAA) method. One-gram samples are encapsulated in a polyethylene vial and placed in a thermalized beam of neutrons produced from a nuclear reactor. Samples were measured for the Doppler broadened prompt gamma ray at 478 keV using a high purity GE detector and compared to certified reference materials used to calibrate the system. A minimum of four standards are analyzed with every work order. The detection limit reported is a function of the counting times required for each.

Chloride determination was attained using the Instrumental Neutron Activation Analysis (INAA). A one-gram aliquot was weighed into a medium polyethylene vial and irradiated at a thermal flux of 7×10^{12} n cm-2 s-1 in a computer-controlled rabbit system. After the appropriate decay time (i.e., to allow aluminum and other very short lived isotopes to decay), the samples were counted sequentially. Values were corrected for decay and compared to a standard calibration (two standards were analyzed with every batch).

Mercury measurement was attained using Cold Vapor Flow Injection Mercury System (FIMS). A 0.5-grams sample was digested with aqua regia at 90 °C and the Hg in the resulting solution oxidized to the stable divalent form. Since the concentration of Hg was determined via the absorption of light at 253.7 nm by Hg vapor, Hg (II) was reduced to the volatile free atomic state using stannous chloride. Argon was bubbled through the mixture of sample and reductant solutions to liberate and to transport the Hg atoms into an absorption cell. The cell was placed in the light path of an Atomic Absorption Spectrophotometer (AAS). The maximum amount absorbed (peak height) is directly proportional to the concentration of mercury atoms in the light path. Hg analysis was performed using a Perkin Elmer FIMS 100 cold vapor Hg analyzer.

All other element and oxide contents measurements were attained through a lithium metaborate/tetraborate fusion process followed by Inductively Coupled Plasma-Optical Emission Spectrometry (ICP-OES) for main elements or Inductively Coupled Plasma-Mass Spectrometry (ICP-MS) for trace elements analysis. The fused sample were diluted and analyzed by a Perkin Elmer Sciex ELAN 6000, 6100 or 9000 ICP-MS. Three blanks

and five controls (three before the sample group and two after) were analyzed per group of samples.

II.6.   Chemical analysis of thermal water samples

Thermal water samples were taken from eruptive and quiescent pools as near as possible to the vent or seep. Water was filtered using 0.45 μm filter (millipore cellulose nitrate membrane) and then collected in 200 ml polyethylene bottles previously rinsed with discharging water and sealed with air-tight caps. Samples for cation analysis were acidified with 2 ml of HNO_3 after filtration. Sampling procedures used in this study were done following that of previous studies (e.g. Giggenbach and Gouguel, 1989). The temperature and pH of each site were measured in the field.

The major, minor and trace element composition of thermal water samples were determined using a combination of analytical techniques at the Geology Department, Universidad de Chile. Anion concentrations were determined using a Metrohm 861 Advanced Compact Ion Chromatographer (IC), while cation concentrations were determined using a Perkin Elmer Optima 7300V Inductively Coupled Plasma Optical Emission Spectrometer (ICP-OES).Carbonate species concentrations were measured by acidimetric titration with back titration, following the Giggenbach and Gouguel (1989) method to avoid the contribution of other acids.

II.7.   Silica precipitation field experiment

In order to estimate the silica precipitation rates and determine the chemical composition and textures of newly formed sinter, an *in-situ* field experiment was undertaken at one hot spring pool and discharge channel. Previously weighted glass slides were situated along the channel, at four spots, about 3 meters apart. At each spot a set of six glass slides were situated. Half of the slides were positioned perpendicular to the water flow direction, while the other half was positioned parallel to the discharge (**¡Error! No se encuentra el origen de la referencia.**). The set-up phase of this 10-month experiment took place during January 2012.

Figure 4. Site of silica accumulation rate experiment at El Tatio, Chile. The image shows the location of the glass and stick sets along the discharge channel. Upper pictures illustrate the orientation of glass slides with respect to water flow (white arrows) and show the disposition of glass slides at each position along the channel.

Three sample collection stages were followed: March, October and November 2012, and during each visit glass slides were collected into sterilized 500 ml plastic tubes. Additionally, one glass slide perpendicular to the water flow was added to each spot in March 2012, and removed a year later in April 2013.

Samples were dried at room temperature. The mass of silica precipitate was estimated by discounting the original weight of the glass slide from the total weight of the samples once dried. Slides collected in March were examined under the FEG-SEM at the University of Auckland, New Zealand. The slides collected in October and November were examined under SEM observation at the Geology Department of the Universidad de Chile, under the conditions that are specified in the "Scanning Electron Microscopy of sinter samples" section.

Environmental conditions such as the ambient temperature and humidity, and the wind velocity and direction were measured on site at the beginning of the experiment using a thermo-anemometer and a portable hygrometer. Evaporation rate was estimated by a simple procedure: a known amount of water (e.g. 1 ml or 0.5 ml) was poured onto a dry sinter surface at the field; the wetted area and the time that it takes to dry were measured. In addition, the hydrodynamic conditions of the water flow, such as the degree of turbulence and the water flow velocity, were also noted at the field site, along with the physico-chemical parameters, such as temperature and pH.

CHAPTER III   BACKGROUND

III.1.   Silica in hot spring waters

The origin of dissolved silica in thermal waters is related to water-rock interaction processes that occur in geothermal systems. Thermal waters dissolve primary rock-forming minerals and precipitate secondary minerals in a multi-step process leading to chemical equilibrium. Dissolution reactions of rock-forming minerals incorporate cations and silica to thermal fluids, although the final concentration of SiO_2 is controlled by the solubility of quartz in the reservoir (Figure 5; Fournier and Rowe, 1966; Iler, 1979; Anórsson, 2000).
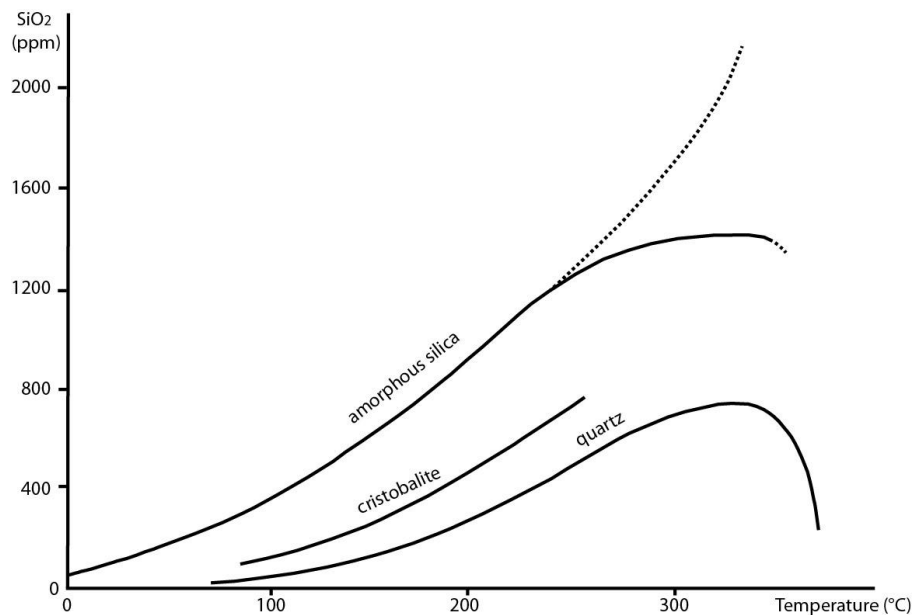
Figure 5. The solubilities of quartz cristobalite and amorphous silica at the vapour pressure of the solution (Fournier and Rowe, 1966)

In thermal waters in equilibrium with quartz or amorphous silica at high temperatures, silica is generally found as monosilicic acid, $H_4SiO_4^o$ (Ellis and Mahon, 1977). The concentration of monomeric silica in cooled geothermal waters decrease with time and approaches to the steady-state concentration for equilibrium with amorphous silica at 25 °C (Krauskopf, 1956). According to Iler (1979), this value is 70 - 130 ppm of SiO_2 at 25 °C. If silica present in solution exceeds the amorphous silica solubility, it polymerizes through a series of reactions to produce polymeric silicic acids (Ellis and

Mahon, 1977). The polymerization of silicic acid begins with the formation of cyclic molecules that then aggregate to form three dimensional molecules, maximizing the number of O-Si-O bonds and minimizing the number of SiOH groups (Iler, 1979).

According to White *et al.* (1956), the rate of polymerization is influenced by pH, temperature, degree of super-saturation, ion concentration and the presence of previously formed colloidal silica and particulate material. The rate of polymerization decreases at pH < 5 and pH > 9, and increases with the amount of nuclei in solution. At pH > 6, the presence of dissolved Ca^{2+} and Na^+ or organic molecules catalyze the polymerization reaction due to interparticle bonding through the cations (Iler, 1979; Rodgers *et al.*, 2004). Dilution of thermal water by mixing with fresh cold water reduces the concentration of silica and therefore also reduces the rate of polymerization (Ellis and Mahon, 1977), while, according to White *et al.* (1956), the presence of previously formed silica nucleus increases the polymerization rate, similarly to heterogeneous nucleation on crystals.

III.2.   Mechanisms of sinter formation

Silica precipitation is largely governed by abiotic factors, such as temperature, pH and cation concentration, that affect the degree of silica saturation and polymerization (White *et al.*, 1956; Iler, 1973; Brown and McDowell, 1983; Mroczek and Reeves, 1994). However, biotic components can provide reactive sites for biologically passive silica precipitation (Konhauser and Ferris, 1996; Farmer, 1999; Phoenix *et al.*, 2000; Benning *et al.*, 2004a, b).

Silica precipitation can occur sub-aerially or sub-aqueously through different mechanisms. According to Handley and Campbell (2011) the process of sinter formation in sub-aqueous conditions involves silica precipitation due to gravitational settling of aggregated colloids, silica super-saturation, or silica nucleation over substrates. Colloid aggregation processes involve Brownian and London Forces, which are diffusive and temporarily attractive forces, respectively (Hunter, 1993). Colloids form by silica polymerization driven by evaporation and cooling of water in menisci, subaerial water

films and pooled water influenced by splash and spray (Hinman and Lindstrom 1996; Lowe *et al.* 2001; Mountain *et al.*, 2003). Higher silica saturation promotes more numerous and smaller colloids (Makrides *et al.*, 1980).

In sub-aerial conditions, silica precipitation occurs mainly by evaporation to dryness. In this case, environmental factors such as wind and surface waves have a great influence on the precipitation rate and sinter textures (e.g. Handley *et al.*, 2005).

III.3.   Characteristics of siliceous sinter deposits

III.3.1.   Sinter fabrics and textures

According to Handley and Campbell (2011), depending on the state of polymerization of silica at the moment of its deposition, different sinter textures can originate. Deposition of soluble silica (monomeric silica or polymeric silica) produces a glass-like "vitreous" sinter fabric, and is common in acidic fluids or near-vent settings, whereas the deposition of colloids leads to the formation of porous granular sinter. Mixed solutions produce dense cemented granular sinter due to the precipitation of soluble silica at colloid joints, where the negative radius of curvature has lower interfacial energy (Iler, 1979; Rodgers *et al.*, 2002).

Hydrodynamic (flow rate conditions) and physico-chemical conditions (e.g. pH and temperature) have an impact on the biologic population that thrives in thermal waters, whose silicification and preservation ultimately influence the sinter textures (Cady and Farmer 1996; Campbell *et al.* 2001; Lowe *et al.* 2001; Lowe and Braunstein 2001; Lynne *et al.*, 2003; Guidry and Chafetz 2003a; Lynne 2012).

Microbial communities that thrive in thermal waters comprise of various types. Low-temperature (<35 °C) microbes consist of cyanobacteria with an inner tubular filament and a thick outer sheath, with a total exterior diameter of >8 μm (Figure 6A), and form black or dark brown microbial mats, called *Calothrix* (Cassie, 1989; Cady and Farmer, 1996; Lynne *et al.*, 2003, 2012).

Mid-temperature (35-59 °C) microbes form orange microbial mats with a microscopic morphology consisting of thin-sheathed filamentous cyanobacteria with exterior diameter <5 µm called *Leptolyngbya* (previously called *Phormidium*) (Figure 6B; Walter, 1976; Cady and Farmer, 1996; Lowe *et al.*, 2001; Hinman and Lindstrom, 1996; Campbell *et al.*, 2001; Lynne and Campbell, 2003; Lynne, 2012). Coniform microbial mats also inhabit mid-temperature thermal waters but they require deep and quiet environmental conditions (Figure 6C; Cady and Farmer, 1996; Lynne, 2012).
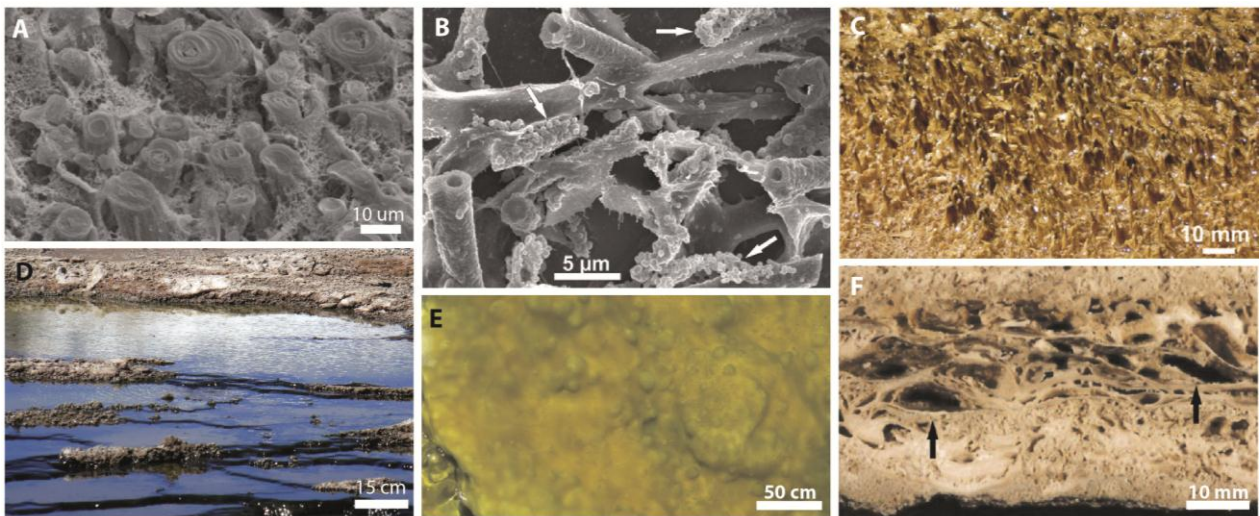
Figure 6. Low- (<35 °C) and mid-temperature (35-59 °C) microbes and sinter textures.A: SEM images of low-temperature microbes from dark brown mat at Orakei Korako. Exterior filament diameter is ~8 µm. B: SEM image of mid-temperature microbes from orange mat display exterior filament diameters of <3 µm (arrows indicate newly deposited opal-A nano-spheres). C: Modern hot spring setting revealing coniform microbial mats thriving in thermal water around the edge of a pool. Yellowstone National Park, U.S.A. D: Modern micro-terracette environment that hosts black microbial mats in low temperature setting at El Tatio, Chile. E: Living orange microbial mat at Orakei Korako, New Zealand. Bubbles are formed by trapped oxygen released during photosynthesis. F: Preserved bubble mat sinter at Orakei Korako, New Zealand. Oval voids (black arrows) indicate the sites where oxygen was trapped prior to silicification. (A, B, C, E and F images taken from Lynne, 2012)

High-temperature (>59 °C) microbial mats are commonly light pink and consists of <1 µm diameter filaments (Cady and Farmer, 1996). Fast flowing discharge channels are commonly inhabited by long filamentous microbes referred to as streamers (Smith *et al.*, 2003; Lynne *et al.*, 2005). The presence of diatoms is also reported in several siliceous sinter deposits (Jones *et al.*, 2001; Schinteie *et al.*, 2007).

In low-temperature distal apron settings, plant-rich sinter can originate by silicification of plant material (Lynne, 2012).Sinter formed in shallow and slow flowing channels from distal apron settings usually shows a micro-terracette morphology (Figure 6D) and palisade sinter texture, that consist of closely packed, vertically stacked micro-pillar structures(Lynne, 2012).

Mid-temperature discharge channels and aprons show a "bubble mat" sinter texture, which is originated by the silicification of orange and green microbial mats (*Leptolyngbya*) that liberate gas through photosynthesis (Figure 6E; Walter, 1976; Lowe *et al.*, 2001; Hinman and Lindstrom, 1996; Lynne, 2012). Bubble mat sinter texture consists of curved laminations with oval voids, which can be observed at a macroscopic scale (Figure 6F; Lynne, 2012). Silica encrustation of mid-temperature coniform microbial filaments produces coniform texture.

In high-temperature (>60 °C) settings, various sinter textures can be produced depending on the hydrodynamic conditions:

(1) At non-overflowing, high temperature pools and discharge channels a lily-pad texture develops due to small waves produced by wind or upwelling water. Lily-pad structures consist of low, flat-topped digitate rims that grow towards the center of the pool (Figure 7A; Renaut *et al.*, 1996; Lowe and Braunstein, 2003; Lynne, 2012).

(2) At intermittently overflowing pools and channels, digitate sinter rims form as silica precipitates over the pool rims during overflowing events (Lowe and Braunstein, 2003; Lynne, 2012). Digitate sinter texture consists of irregular-shaped surfaces with smooth knobs and ridges separated by crevices and discontinuous horizons of laminated sinter (Figure 7B, C; Braunstein, 1999; Braunstein and Lowe, 2001; Lowe and Braunstein, 2003).

(3) At near vent splash zones (>90 °C), spicular, columnar or bulbous digitate sinter texture may originate (Braunstein and Lowe, 2001; Lowe and Braunstein,

2003; Jones and Renaut 2003; Lynne 2012).These textures, called geyserite, form sub aerially, by rapid cooling and evaporation of the ejected water droplets. They are characterized by an internal structure formed by multiple stacked convex laminations (Figure 7B, D-F; Braunstein, 1999; Braunstein and Lowe, 2001; Lowe and Braunstein, 2003).
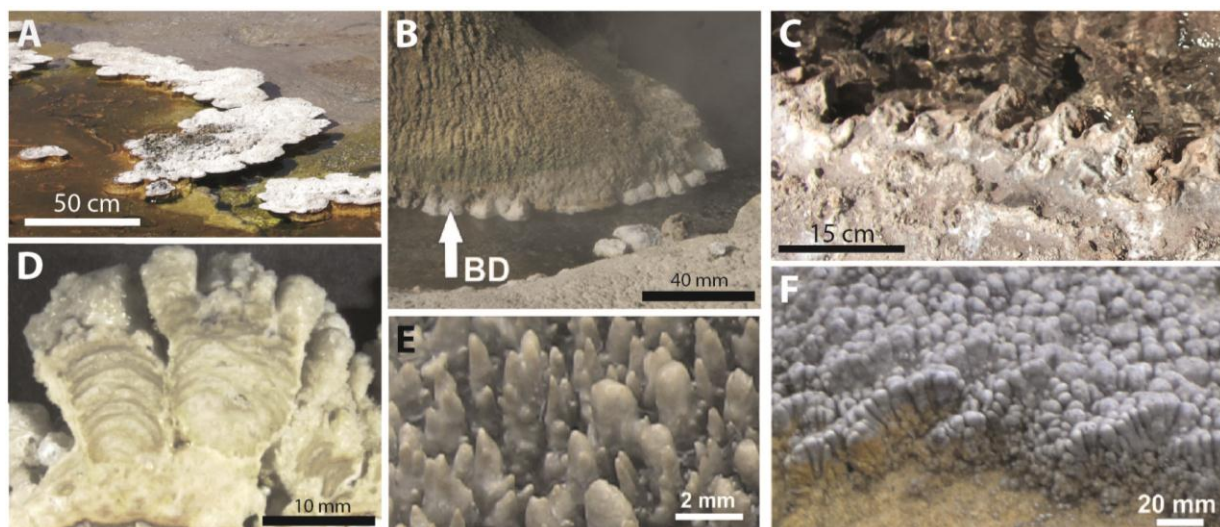
Figure 7. High-temperature (>60°C) sinter textures. A: Flat, lily-pad sinter structures protruding toward center of hot pool at Yellowstone National Park, U.S.A. B: Bulbous digitate sinter (BD) forms at air–water interface at Diamond Geyser, Orakei Korako, New Zealand. C: Digitate sinter rim in a high temperature pool at El Tatio, Chile. D: Cross-sectional view of columnar sinter shows multiple-stacked convex laminations within each column, Orakei Korako, New Zealand. E: Columnar geyserite around rim of an eruptive hot pool at Yellowstone National Park. F: Modern needle-like spicular geyserite sinter texture at Waiotapu, New Zealand. (A, B, D, E and F images taken from Lynne, 2012)

Columnar texture refers to up to 10 mm high and wide columns, vertically or sub-vertically oriented, with smooth rounded top surfaces, that form above water-air interface (Figure 7D and F; Lynne, 2012).

Spicular texture consists of fine needle-like spicules, formed above water-air interface. Branches of spicules may radiate outwards from a central core (Figure 7E; Jones and Renaut, 2003; Lowe and Braunstein, 2003; Lynne, 2012).

Bulbous digitate texture develops around the pool rims of eruptive hot pools and geysers at the water-air interface. Individual bulbous digits are characterized by smooth, gently sloping tops (Figure 7B; Lynne, 2012).

Intermittent flow in low- to mid-temperature hot spring settings leads to the formation of silica oncoids or pisolites, which are loose, rounded, concentrically laminated sinter fragments that form by rolling around during eruptive cycles and then dry while resting on a previously formed sinter surface (Renaut *et al.*, 1996; Walter *et al.*, 1996; Jones and Renaut, 1997; Campbell *et al.*, 2001, 2004; Lynne *et al.*, 2008).The cementation of these fragments leads to the formation of sinter with oncoidal texture (Lynne, 2012). Intermittent flow conditions may also generate breccia sinter. This texture is formed by sinter terrace fragments, re-cemented by silica. Sinter can be deposited, then dried and broken by hydrothermal eruptions, freezing, or wild life action after which the fragments are re-cemented by silica precipitated from the newly active hot spring (Rimstidt and Cole, 1983; Campbell *et al.*, 2001; Lynne *et al.*, 2008, Lynne, 2012).

III.3.2.   Morphology and crystallinity of silica phases

Siliceous sinter deposits are mainly constituted by one or more silica phase, including opal-A, opal-CT, opal-C and quartz. The phase that initially precipitates is opal-A, being the less mature phase, that undergoes a series of dissolution, re-precipitation and re-crystallization processes that change one phase into another, concluding in quartz, the most mature phase (Figure 9; Cady and Farmer, 1996; Campbell *et al.*, 2001; Guidry and Chafetz, 2003; Lynne and Campbell, 2003; Lynne and Campbell, 2004, and Lynne *et al.*, 2005). These changes are morphological and mineralogical and constitute a maturation or diagenetic process (Lynne *et al.*, 2005).

Lynne *et al.* (2005) studied Opal Mound sinter in Roosevelt Hot Springs, U.S.A., finding that the transition from one phase to the next is gradual and that sometimes two consecutive silica phases co-exist (Figure 8). In their study, the preserved diagenetic process began with individual ~8μm diameter smooth opal-A micro-spheres that formed botryoidal aggregates when the micro-spheres merge together. Botryoidal clusters increase their "bumpiness" leading to the formation of bumpy micro-spheres, which is
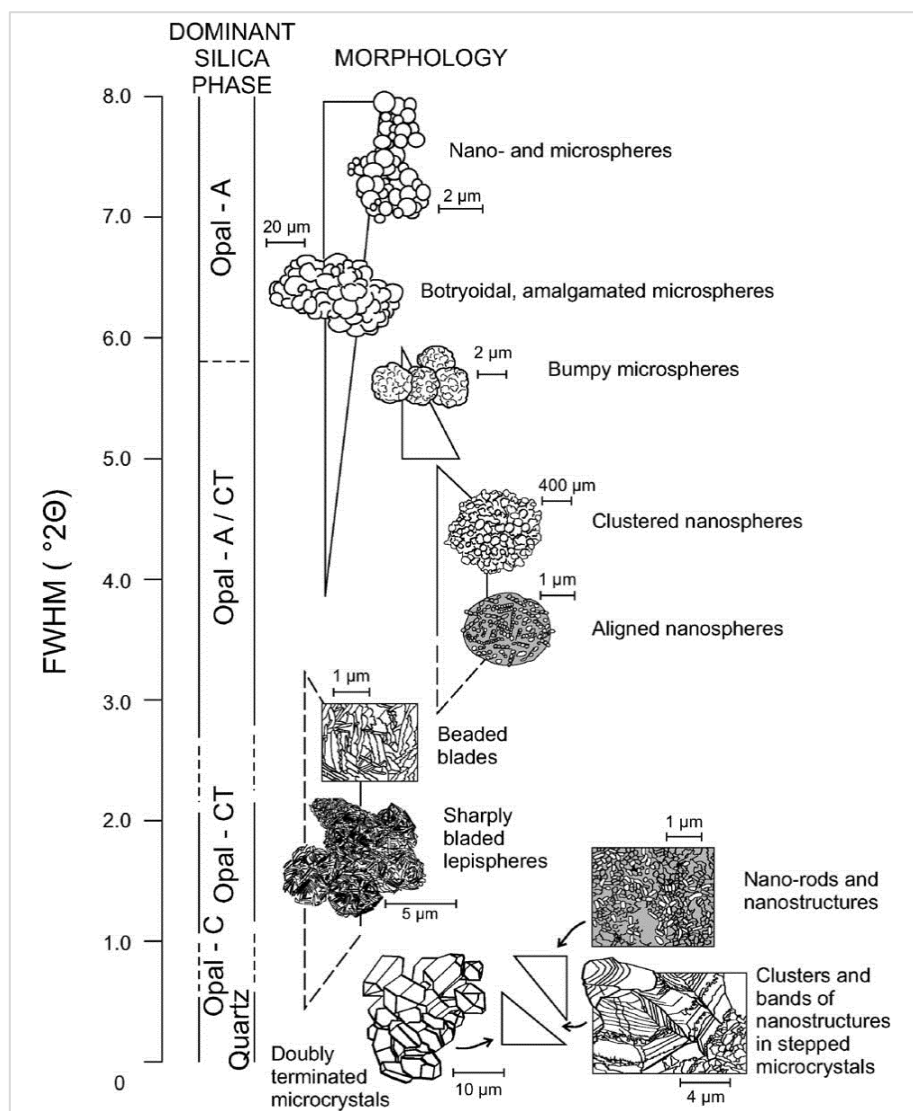
Figure 8. Morphological and mineralogical changes that occur through silica diagenesis. Transformation from one silica phase and morphological state to another occurs progressively and gradationally. Each stage overlaps the previous stage, resulting in the co-existence of two or more morphological states at any one point in the diagenetic pathway (from Lynne *et al.*, 2005, Figure 3).

the transitional phase to opal-A/-CT. Then bumps decrease in size and reorganize into clusters of smooth, initially random, nano-spheres that subsequently align. In the transition to opal-CT, aligned nano-spheres join to form beaded, somewhat jagged plates that are the precursors of sharp blades. Well-developed bladed spheres are the classic example of opal-CT. Reorganization of blades into opal-C elongate, randomly oriented clusters of nano-rods and nano-structures constitutes the transition to doubly terminated quartz micro-crystals. The silica morphological changes through diagenesis

21

are illustrated in Figure 8, while SEM images of these different morphologies are shown in Figure 9.
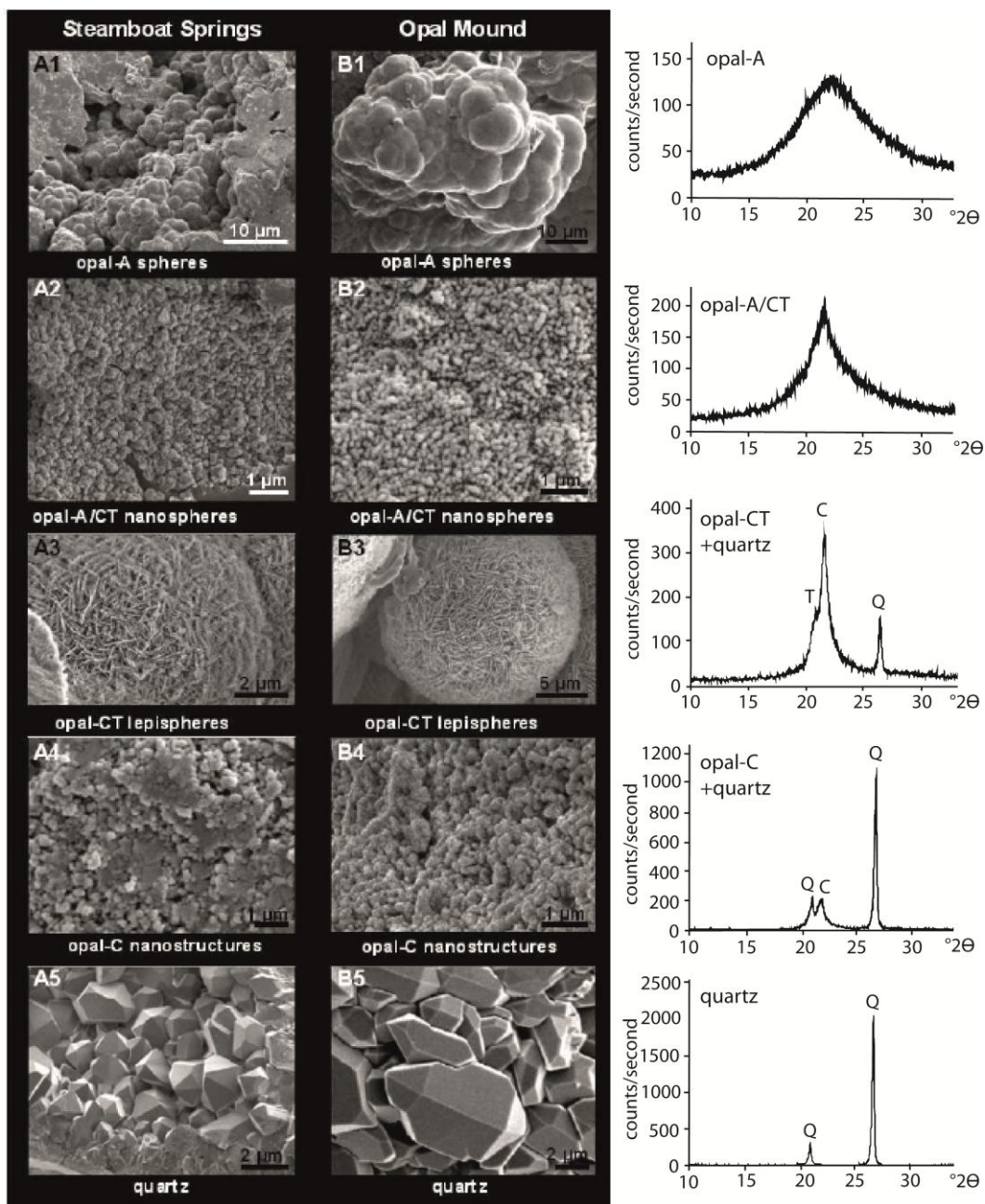
Figure 9. Example of morphological and mineralogical evolution of silica phase through diagenesis. SEM images show the sinter diagenetic transformation from opal-A nano-spheres to quartz crystals in two examples from USA sinters. XRD traces show an increase in lattice order through diagenesis with narrowing peaks in Opal Mound sinter deposit (from Lynne *et al.*, 2005, Figure 2)

The mineralogical maturation of sinters can also be tracked using XRD analysis (Figure 9). The width of the XRD peaks indicates the degree of lattice order/disorder. In

22

this way, non-crystalline opal-A and opal-A/CT produce XRD patterns with characteristic wide bands, or broadbands, while para-crystalline opal-CT and opal-C and microcrystalline quartz produce traces with increasingly sharper, narrow peaks (Lynne, 2007).The Full Width at Half Maximum (FWHM) value corresponds to the measured wideness of the broadband at half of the maximum intensity, and is used to compare the degree of lattice disorder between different non-crystalline phases.

The diffraction bands are centered at different °2Ɵ values depending on the silica phase, this value is labeled the apex position. The apex position is 22.2 °2Ɵ for opal A, decreases to 21.75 °2Ɵ for opal-A/CT, opal-CT and opal-C, and to 20.85 °2Ɵ for quartz (e.g. Lynne and Campbell, 2003, 2004). Typical FWHM values for opal-A, opal-A/CT, opal-CT, opal-C and quartz in sinters are 7.5 °2Ɵ, 4.5 °2Ɵ, 1.8 °2Ɵ, 0.6 °2Ɵ and 0.3 °2Ɵrespectively (Lynne, 2007) although these values are referential, and only correspond to the analyzed siliceous sinters in USA.

Recent studies demonstrate that the sinter diagenesis is not time-controlled, which is illustrated by the presence of quartz (the diagenetically most mature silica phase) in two siliceous sinter deposits of very different ages. The relatively old Steamboat Springs sinters (11,493 ± 70 yrs; Lynne *et al.*, 2008) and the much younger Opal Mound sinter (1,920 ± 160 and 1,630 ± 90 yrs; Lynne *et al.*, 2005) are both composed by opal-A, opal-A/CT, opal-CT, opal-C, moganite, and quartz.

III.3.3.   Sinter chemistry

Several authors have reported major and trace element composition of siliceous sinters of various locations in the past decades. The information presented in (Table 1) constitutes a review of the available published data and corresponds to different geothermal sites around the world: Ohaaki, Tokaanu springs, Waiotapu, Waikite springs and Wairakei in New Zealand; El Tatio in Chile; Takigami, Ohtake, Hachobaru, Makizono and Fushime in Japan; and Yellowstone National Park in USA.

Table 1. Siliceous sinter geochemistry according to the available published data.

		Average	Higher value	Lower value	Standard deviation
SiO_2	wt%	82	94	60	10
TiO_2	wt%	0.04	0.07	0.02	0.02
Al_2O_3	wt%	2.4	10.0	0.2	2.7
Fe_2O_3	wt%	1.5	29.7	0.0	4.1
MnO	wt%	0.2	2.6	0.0	0.5
MgO	wt%	0.3	4.8	0.0	0.9
CaO	wt%	0.6	3.3	0.0	0.7
Na2O	wt%	0.8	2.8	0.1	0.7
K2O	wt%	0.4	1.2	0.0	0.3
B	wt%	0	0	0	0
SO_3	wt%	1482	2897	930	946
As	ppm	603	2070	56	680
Sb	ppm	751	20528	1	3025
Ba	ppm	672	7293	1	1689
Cr	ppm	31	91	12	25
Cu	ppm	12	26	8	5
La	ppm	9	68	1	13
Nb	ppm	14	48	3	12
Ni	ppm	2	2	1	1
Pb	ppm	4	5	2	1
Rb	ppm	6	18	1	4
Sr	ppm	23	86	3	22
Th	ppm	64	315	5	87
V	ppm	4	5	2	2
Y	ppm	21	51	4	19
Zn	ppm	3	5	1	2
Zr	ppm	10	44	1	10
Ag	ppm	11	33	3	8.3
Hg	ppm	1	1	0.7	0
Au	ppm	11	90	0	24

Calculated over the data of Nicholson and Parker, 1990; Yokoyama *et al.*, 1993, 2004; Fournier *et al.*, 1994; McKenzie *et al.*, 2001; and Landrum *et al.*, 2009.

The SiO_2 content of these sinters varies between 60 wt% and 94 wt%, the main minor elements present are usually sulfur, iron, calcium and aluminum, with average values of their oxides around 2 wt% each. They present variable concentration of trace elements, including gold, silver and copper, which are of economic interest; and arsenic, antimony, mercury and lead, which are potentially a health hazard, although only boron, sulfur oxide, arsenic and antimony show high average concentrations (>600 ppm).

Table 1 summarizes the available published data showing the higher, lower and average content of these elements in the siliceous sinter deposits. The complete geochemical database is presented in APPENDIX II. The data includes sinter samples that show a SiO_2 content higher than 60 %.

III.4. El Tatio Geothermal System

The El Tatio geothermal Field is located in the Precordillera of the II Region of Chile, at a high altitude and surrounded by andesitic stratovolcanoes of the High Andes Cordillera. It covers nearly 10 km², with more than 100 hydrothermal features including geysers, hot pools, fumaroles, sinter deposits, mud volcanoes and hydrothermally-altered areas.

The climatic conditions at El Tatio are extreme, with an eight months long dry season and a rainy season from November to March (Zhou and Lau, 1998). Atmospheric thermal variability is high (up to 35°C daily variation; Fernández-Turiel *et al.*, 2005). Evaporation rate at El Tatio is also high, with mean annual evaporation rates of 72.8 mm that reach maxima during October (69.5 mm) (DGA data, 2010).

The first investigations at El Tatio focused at evaluating the energy potential and are almost exclusively on fluid geochemistry (Ellis and Mahon, 1977; Lahsen and Trujillo, 1976). More recently, other studies have addressed the issue of the source and genesis of the thermal waters (Tassi *et al.*, 2005; Cortecci *et al.*, 2005) and the characterization of geothermal features present at the site (Glennon and Pfaff, 2003).

The El Tatio thermal waters are characterized by their near neutral pH, high chlorine (~8000 mg/l), sodium (~4000 mg/l), silica (up to ~220 mg/l) and arsenic (up to ~30 mg/l) contents. Sulphur contents are low, with maximum values of ~70 mg/l (Cusicanqui *et al.*, 1976; Fernández-Turiel *et al.*, 2004; Landrum *et al.* 2005; Cortecci *et al.*, 2005).

The thermal features of the El Tatio geothermal field are mainly located along the Salado river valley and its affluents. The geologic sequence that outcrops in the El Tatio area includes: Jurassic marine sediments, Jurassic-Cretaceous meta-andesites and Cretaceous sediments; Tertiary to Miocene ignimbrites, andesites and volcanic agglomerates; and Plio-Holocene dacitic and rhyolitic ignimbrites, lavas and domes (Lahsen and Trujillo, 1976). Glacial, alluvial and colluvial deposits overlay this geologic sequence and are locally covered by siliceous sinter deposits (Figure 10; Fernández-Turiel *et al.*, 2005, Lahsen and Trujillo, 1976).
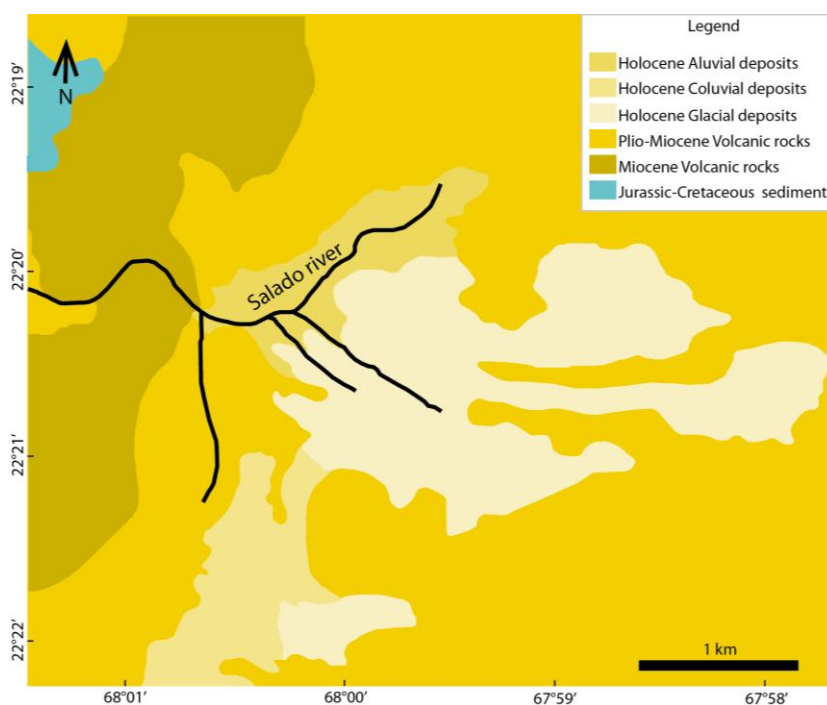
Figure 10. Geologic map of the El Tatio area (Fernández-Turiel *et al.*, 2005)

The hydrogeological model for El Tatio Geothermal System proposed by Cusicanqui *et al.* (1975) and Giggenbach (1978) involves a geothermal reservoir trapped in volcanic and ignimbritic rocks and a second aquifer hosted in a dacitic unit, sealed by silica deposits and clays. Thermal waters derive from precipitation in an area located at 12-20 km to the E-SE of El Tatio (Giggenbach, 1978). Lateral fluid migration is controlled by the permeability of volcanic rocks, and their upwards migration is constrained by NW-SE and SE-SW fractures and by the Serrania de Tucle-Loma Lucero horst. The heat source has been correlated to the Pastos Grandes and Cerro Guacha

caldera systems, located east of El Tatio (Alpers and Withermore, 1990; Ellis and Mahon, 1977, Magaritz *et al.*, 1990).

III.4.1.   El Tatio siliceous sinter deposits

Some of the most evident surficial geothermal features at El Tatio geothermal field are the extensive siliceous sinter deposits. Previous studies have focus on the genesis of siliceous oncoids around geyser vents and hot pools, and sinter mineralogical variability related to diagenesis (Jones and Renaut, 1997; García-Valles *et al.*, 2008; Fernández-Turiel *et al.*, 2005).

According to these studies, siliceous sinter deposits at El Tatio are mainly composed of opal-A, with a minor occurrence of opal-A/CT and opal-CT (Fernández-Turiel *et al.*, 2005; García-Valles *et al.*, 2008). Their chemical composition shows variable concentrations of Cl, Na, Ca, S, As, Sb and B (5 - 20 wt%; Fernández-Turiel *et al.*, 2005, Landrum *et al.*, 2009). Mineralogical studies reveal the common occurrence of opal, halite, sylvite and realgar, and rare accessory minerals such as nobleite [$CaB_6O_{10} \cdot 4H_2O$], teruggite [$Ca_4MgAs_2B_{12}O_{22}(OH)_{12} \cdot 12(H_2O)$] and sassolite [$H_3BO_3$] (Rodgers *et al.*, 2002b; García-Valles *et al.*, 2008). In addition, a variety of biological communities of cyanobacteria (*Leptolyngbya* and *Calothrix*) and diatoms thrive in the hot springs that form sinter deposits, whose existence is extremely dependent to thermal waters physico-chemical conditions(Fernández-Turiel *et al.*, 2005).

CHAPTER IV   RESULTS

Five sampling sites were selected at the El Tatio Geothermal Field (Figure 11) that correspond to sodium-chloride thermal pools with (i) different hydrodynamic characteristics, and (ii) different textures and coloration of their associated siliceous sinter deposit. A field description of each selected site is presented in this section, along with a detailed characterization of sinter and associated water samples. Morphological, mineralogical, and chemical data of the analyzed sinter samples are reported, along with the hydrological and chemical characterization of thermal features and the results of the silica precipitation rate experiment.
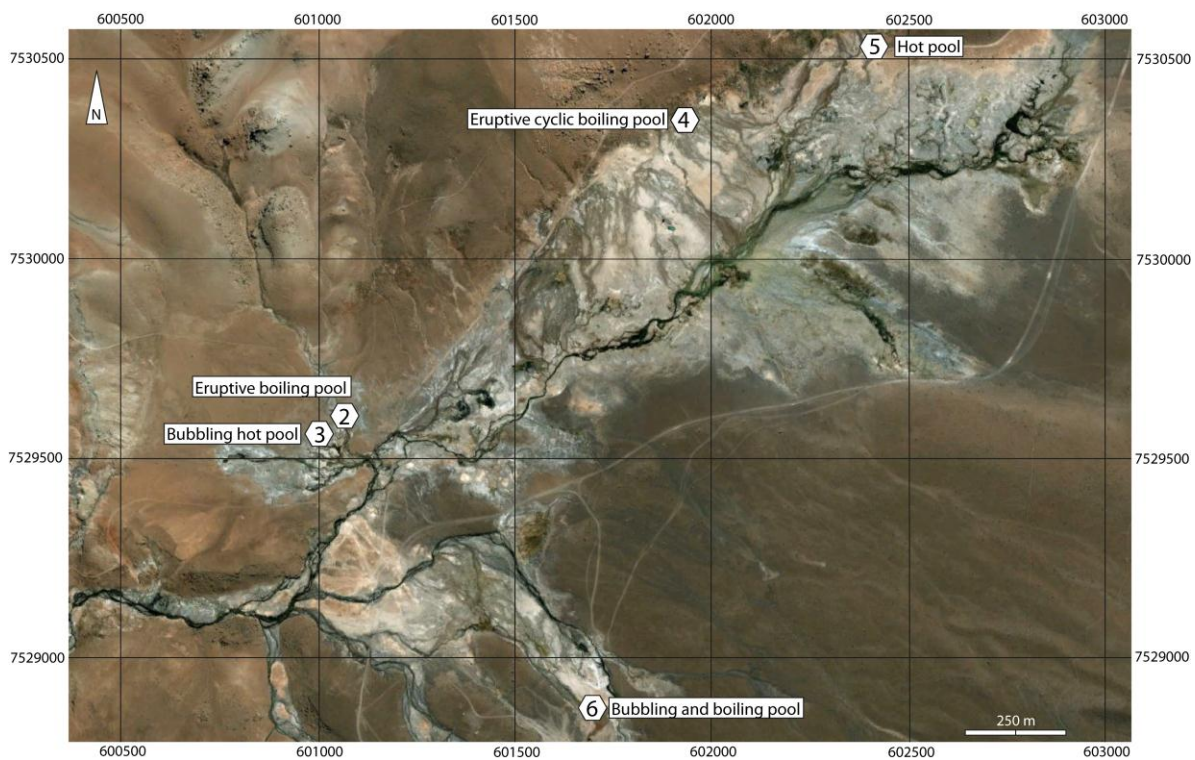
Figure 11.Sampling sites location at the El Tatio geothermal field. Samples were taken from sinter deposits distributed along a NE valley that forms the Salado river. Google Earth® image.

IV.1.   Sampling sites description

The samples thermal pool waters are near neutral pH (6.5 to 7.5) and their temperature ranges from 76.9 to 87.6 °C, the latter correspond to the boiling temperature at 4200 meters above sea level. A brief description of the hydrodynamic conditions of each site and the macroscopic characteristics of the associated sinter deposits are provided in Table 2.

Table 2. Sampling sites characterization.

Site n°	E	N	Pool T (°C)	Pool pH	Site description
2	601057	7529545	86.1	7.4	Eruptive boiling pool. Vent is a NW fracture. Two discharge channels with sinter islands that show lily-pad and spicular texture and sinter rims that show digitate and massive texture. Sinter color is white, although orange coloration is found at the water-air interface.
3	601023	7529497	82.3	6.5	Bubbling hot pool, discharges on only one well defined channel that opens up at 6m length that then forms few centimeters high terraces. Sinter deposit is white grey in general, forming digitate lily-pad on pool rim and near vent discharge channel rim. The bottom of the channel is made of sand at the beginning, when the channel opens there are orange organic mat and streamers, further away there are black organic mat and sinter terraces.
4	601932	7530315	82.7	7.3	Eruptive cyclic boiling pool (~5-10 min cycle). White sinter deposit, mainly geyserite texture in the surface of the deposit. Sinter color is white.
5	602406	7530528	76.9	7.1	Non-boiling, non-bubbling, non-surging hot pool. White sinter deposit forms digitate lily-pad rim at one side, water flows through the other side forming sinter islands. Silicification of plant material.
6	601730	7528814	87.6	7.5	Vigorously boiling and bubbling pool. Sinter deposit forms a pool rim and discharge channel rim. Nodular geyserite texture in near vent areas, lily-pad on pool rims. Terracettes form in overflowing areas. Sinter show a red coloration in sub-aquatic areas and water air interface, and a tan coloration in sub-aerial areas.

IV.2.   Sinter samples characterization

Sinter samples from El Tatio were analyzed using optical microscopy, SEM observation and XRD methods. The inspection of thin sections shows that sinter samples are composed of white, light brown, dark brown and red laminations (<0.1 mm to ~0.25 mm) and variable porosity. The presence of detrital crystals of quartz, plagioclase, pyroxene, phyllosilicates and amphibole is common in all the analyzed thin sections. Filamentous microbes were observed in only one thin section, in sample M3B, although they are commonly observed through SEM. The detailed thin section

petrographic descriptions are presented in APPENDIX III, while SEM observations and XRD results of the analysis of sinter samples are detailed in APPENDIX IV.

SEM observation of the samples reveals that opal-A spheres are the main constituent phase of sinter deposits from all the analyzed sites. The red material that form laminations in sinter from site 3 is entirely composed of flower-like aggregates of bladed Si, As and Fe-rich crystals. The morphology of opal-A spheres includes well-rounded nano- and micro-spheres (Figure 12), bumpy micro-spheres and rough micro-spheres (Figure 13), and spiky micro-spheres (Figure 14).

Nano-spheres and most of the micro-spheres show a smooth surface and their individual diameter can reach 3 μm. Nano-spheres are usually found individually-coalesced (Figure 12A, B). Micro-spheres can occur evenly-coalesced forming well-defined layers (Figure 12C), as randomly-coalesced botryoidal clusters (Figure 12D, E, F), or aggregated forming larger (0.4-5 μm diameter) bumpy micro-spheres (Figure 13A, B, C). Bumpy micro-spheres are found in sites 3, 4 5 and 6 (Figure 13A, B, C). Rough micro-spheres are only found in sites 6 and 3, in sinter laminations (Figure 13D, E). Spiky micro-spheres are only found in sub-aquatic black columns of sample M6.4, and the SEM-EDS chemical analysis indicates a high content of As, Ca and Fe (Figure 14). Silica phase morphologies and sphere sizes for each sample are detailed in Table 3. Sample 3R is omitted from this table because it consists of flower-like Si, As and Ca-rich crystals and not opal-A spheres.

Table 3. Silica phases morphology. Numbers refer to spheres diameter (μm)

Sample ID	Sinter morphology			
	Smooth micro- and nano-spheres	Bumpy micro-spheres	Rough micro-spheres	Spiky micro-spheres
M2.1	0.2-2.2			
M2.3	0.3-2.2			
M3B	0.3-2.3	1-3	2-3	
M3.2	0.2-2	2-3.5		
M4.1	0.3-2.5	2.3-4		
M4.2	0.5-1.5	2-5		
M5	0.2-3	0.4-1.5		
M6.4	0.5-2	2.5 - 5	0.5-3.5	3-7
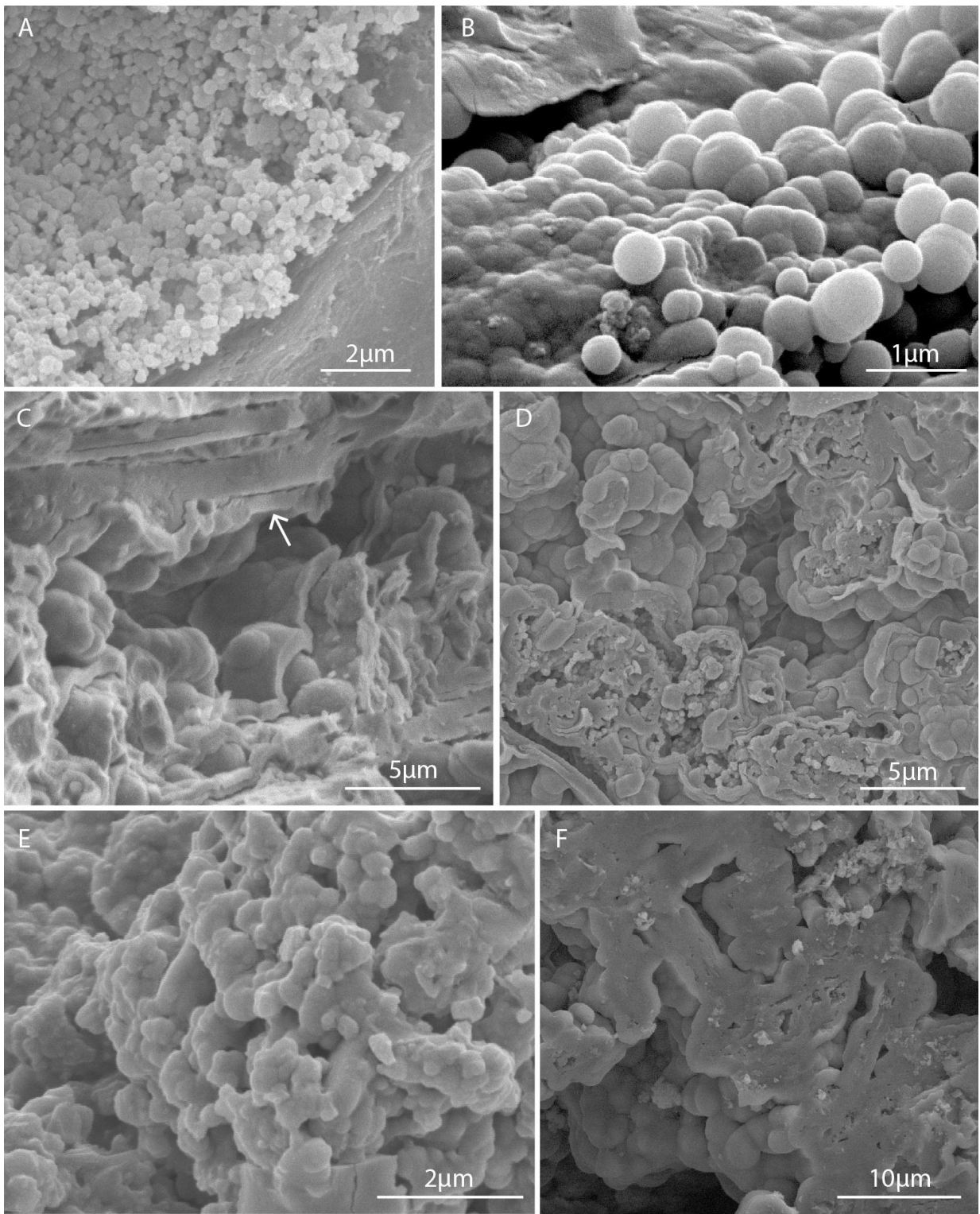
Figure 12. SEM images of individual and coalesced opal-A micro-spheres in El Tatio sinter samples. A-B: Individual smooth opal-A nano-spheres from sample M3.2. C: Coalesced smooth micro-spheres forming massive silica layers (arrow), sample M2.3. D-E: Coalesced smooth opal-A micro-spheres forming botryoidal clusters in samples M2.1, M6.4 and M5
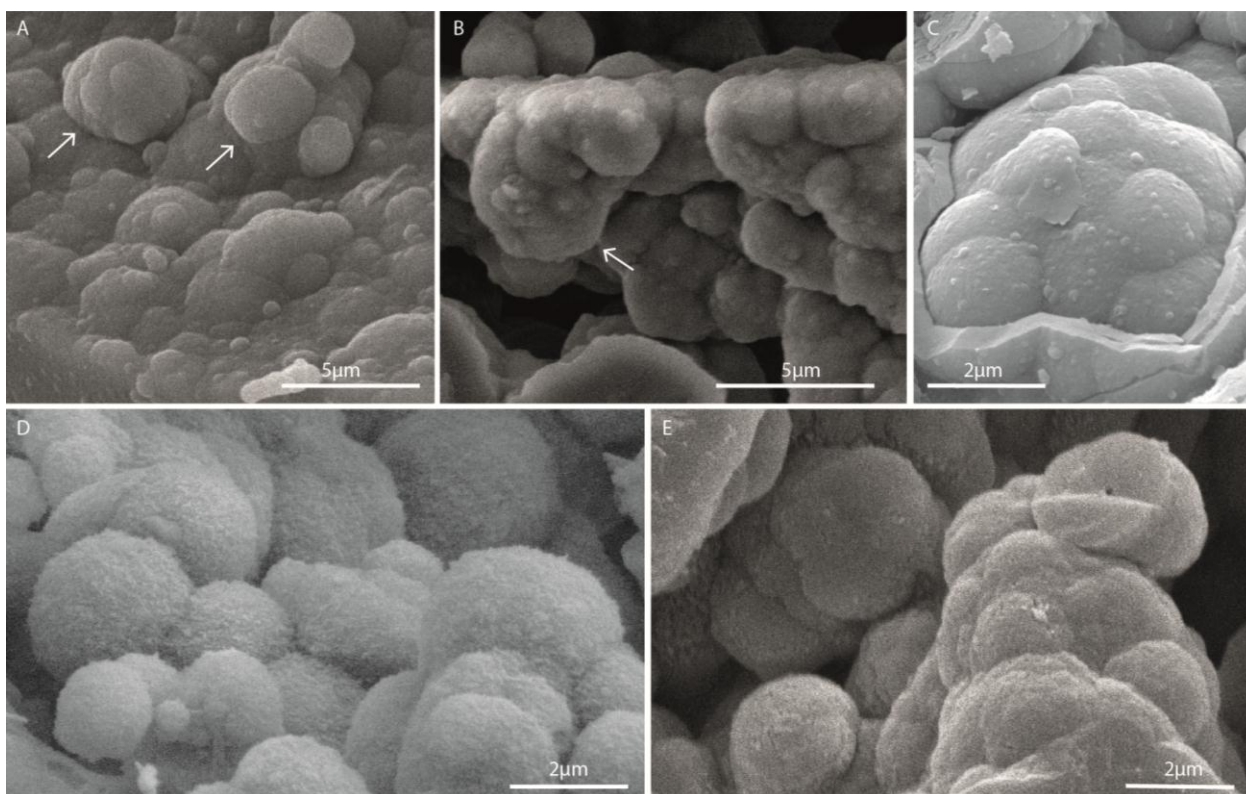
Figure 13. SEM images of bumpy micro-spheres and rough micro-spheres in El Tatio sinter samples. A-B: Smooth bumpy micro-spheres (arrows) in samples M5 and M4.1. C: Bumpy micro-spheres aggregated forming a cluster that is covered by several silica layers in sample M3. D-E: Rough micro-spheres from samples M6.4 and M3.
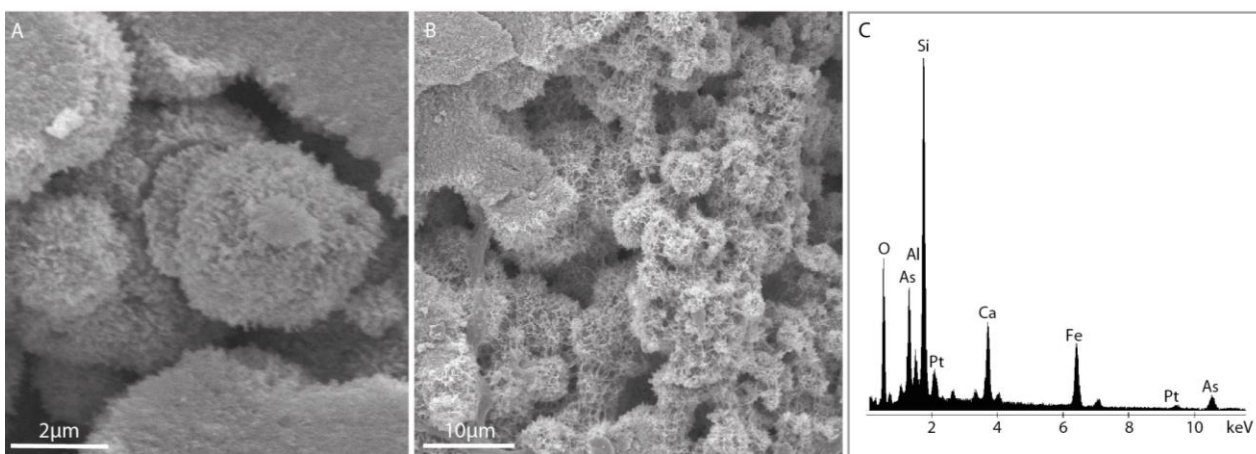
Figure 14. SEM images of spiky micro-spheres in El Tatio sinter samples. A-B: Spiky micro-spheres from sample M6.4. C: SEM-EDS analysis of spiky spheres from B, platinum peak corresponds to sample coating.

Sinter micro-textures identified through SEM observations include micro-columns and ridges (Figure 15A), silicified microbial filaments (Figure 15D), which can be encrusted by low diameter opal-A spheres or replaced by them. Other micro-textures include: massive laminated silica layers with variable thickness (Figure 15C); porous silica layers formed by coalesced opal-A spheres and void space (Figure 15F); lithic rich horizons which are commonly covered by a silica coating and where the presence of microbial filaments is common (Figure 15E); and layers formed by broken silica platelets (Figure 15B) that occur predominantly on sinter surfaces although some deeper horizons.
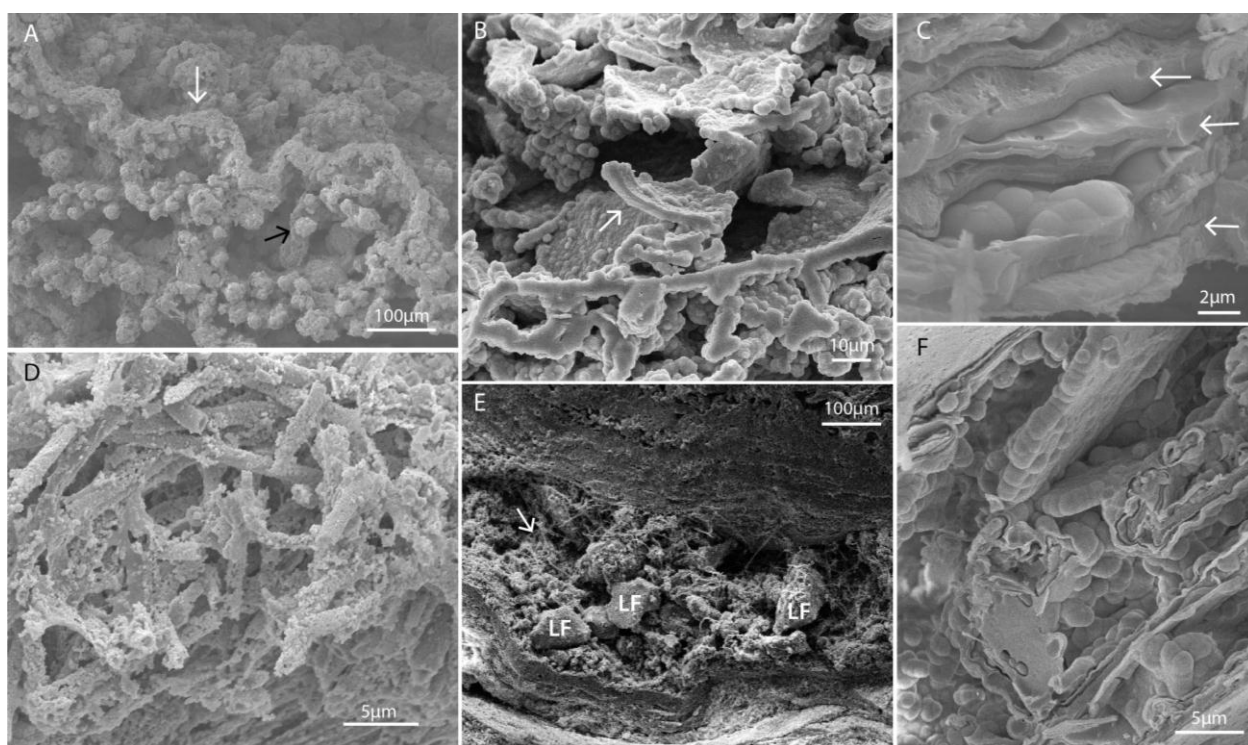
Figure 15. El Tatio sinter micro-textures. A: Micro-columns (black arrow) and ridges (white arrow) from the surface of sample M4.2. B: Silica platelets (arrow) found at the surface of samples M5 and M2.1. C: Massive silica layers (arrows) formed by coalesced opal-A spheres from sample M3.2. D: Mid-temperature microbial filaments encrusted by nanometric opal-A spheres from sample M3.2. E: Lithic fragments (LF) and microbial filaments (arrow) between two massive silica layers from sample M4.1. F: Porous silica layers from sample M2.1.

Accessory evaporitic minerals (gypsum and halite) are common in almost all the sampling sites. Opal-A spheres (Figure 16: A) and other minerals, such as needle-like Si-Ca-As crystals (Figure 16: D and F), tetrahedral Ca-As crystals (Figure 16: D and E) and

lamellar As-Ca crystals (Figure 16: B and C) occur as secondary phases, infilling cavities or fractures. Flower-like aggregates of bladed Si-As-Fe crystals and tetrahedral Ca-As crystals are found in samples M3 and M6.4 as constituents of sinter deposit. F crystals correspond to macroscopic red friable material. SEM-EDS analysis of calcium and arsenic minerals were performed on samples M3 and M6.4. The average chemical composition of these phases is presented in Table 4.
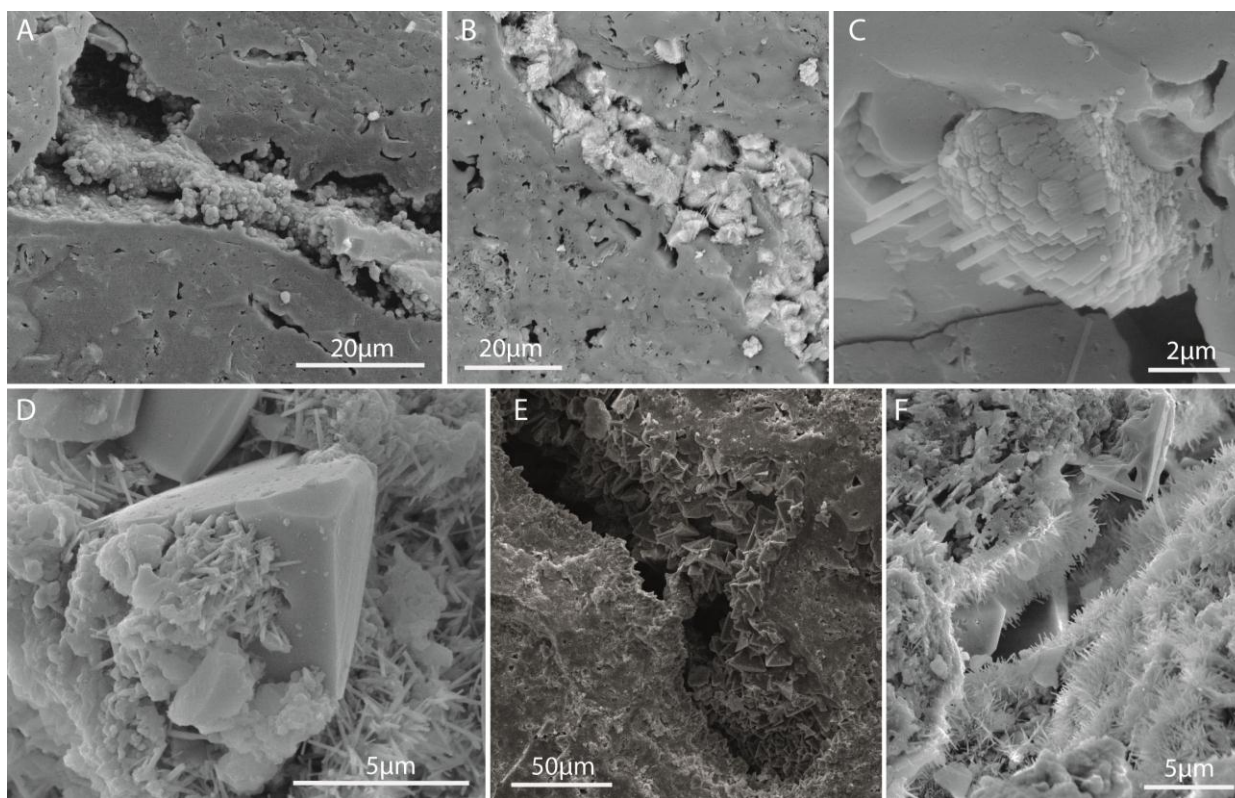
Figure 16. SEM images show opal-A and other minerals in sample M6.4. A: secondary infilling of a cavity by smooth opal-A nano-spheres. B: Lamellar As, Ca crystals infilling a porosity in massive silica. C: Detail of one Lamellar As, Ca crystal. D: detail of a tetrahedral Ca, As crystal (cahnite) and needle-like Si, As, Ca crystals. E: Tetrahedral crystals formed at the walls of a cavity. F: Needle-like crystals and tetrahedral formed at the walls of a cavity.

Table 5 shows the presence of lithic fragments and biological material in sinter samples from El Tatio. Lithic material is commonly found at the base of sinter deposits in a macro-scale and at the base or between laminations at a micro-scale. They are usually rich in Si, Na, Ca, Mg and Fe, and thus it is likely that they correspond to fragments of albite, amphiboles and micas that were also detected through XRD analysis. Biological material is identified through SEM observations, and usually corresponds to microbial filaments of variable diameters; 1 to 5 μm diameter microbes

34

are present at all the sampling sites, whereas >5 µm diameter microbes are only present at distal setting at site 3. Plant material is relatively common and occurs at sites 3, 4 and 6. Silicified pollen particles are found in sinter laminations and columns of sites 3 and 4. Diatom-rich horizons are only found at site 6.

Table 4. Average chemical composition (wt%) of calcium and arsenic accessory minerals

Element	F	N	T	L
O	31	56	53	22
Mg	5			3
Mn				7
Al	4			
Si	17	27		5
Ca	8	8	27	21
Fe	16			2
As	21	8	21	38

F= Flower-like aggregates of bladed Si, Ca, As-rich crystals;
T= Tetrahedral Ca-As crystals; N= Needle-like Si-Ca-As crystals;
L= Lamellar As-Ca crystals

Table 5. Lithic and biological material found in sinter samples from El Tatio.

Sample ID	Lithic material	Biological material			Filament diameter (µm)
M2.1					
M2.3	yes			MF	2.5
M3B				MF	0.8-3
M3R					
M3.2	yes		Pl	Po	MF	0.6-1.5; ~10
M4.1	yes			Po	MF	2.5; ~5
M4.2			Pl	Po		
M5					MF	1-1.5
M6.4		D	Pl		MF	3

D= Diatoms; Pl= Plant material; Po= Pollen particles; MF= Microbial filaments.

The Full Width at Half Maximum (FWHM) values, the maximum peak intensity, and the apex position were calculated from the XRD traces of the analyzed sinter samples. FWHM values vary between 7.8 and 12.5 °2θ. The apex position varies between 22.2 and 23.9 °2θ. The shape of the broadband of XRD traces indicates that the silica phase present in all samples correspond to opal-A (Figure 17). FWHM values and the apex position of each sample, along with the presence of other mineral phases are presented in Table 6.
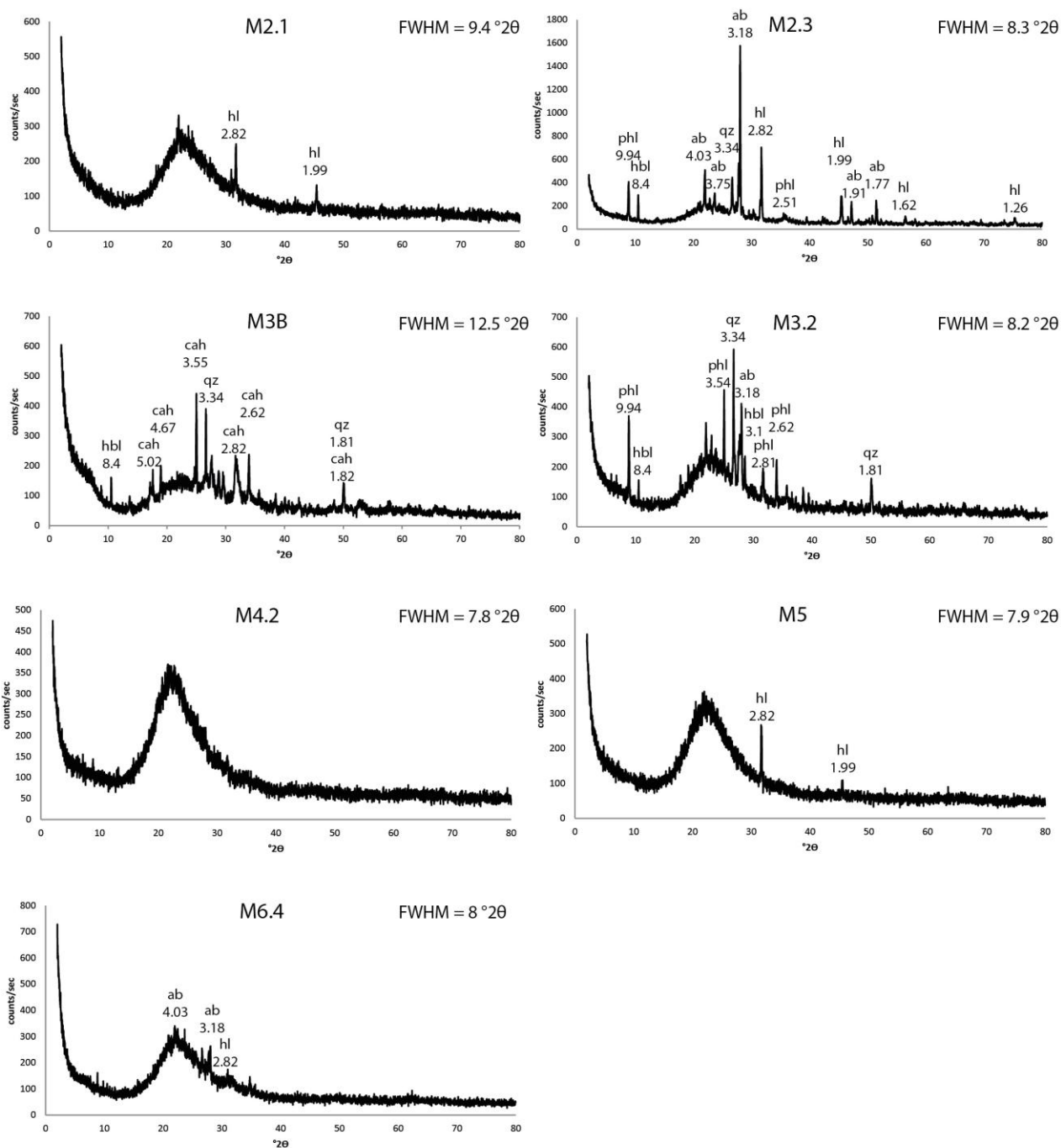
Figure 17. X-ray diffraction traces for El Tatio sinter samples. The broad band corresponds to opal-A. Main peaks are labeled with the mineral phases identified: hl=halite, phl=phlogopite, hbl=hornblende, ab=albite, qz=quartz, cah=cahnite. The numbers under the mineral names correspond to d-spacing.

XRD traces of most of the samples show abundant peaks, which are attributable to the presence of various mineral phases (Figure 17). Halite is present in samples M2.1, M2.3 M5 and M6.4, which is confirmed by SEM observations in samples M2.3 and M5. XRD data of sample M3B show various diffraction peaks that correspond to the rare

36

arsenic-bearing borate cahnite, $Ca_2[B(OH)_4](AsO_4)$. Tetrahedral crystals show an average chemical composition of 53 wt% of O, 27 wt% of calcium and 21 wt% of arsenic obtained by SEM-EDS. It is important to note that light elements (Z<10), such as boron, cannot be detected using this technique.

All the other minerals identified by XRD are attributed to lithic material which is composed of albite, quartz, hornblende and phlogopite. Hornblende and other amphibole peaks such as tremolite, riebeckite and pargasite are very similar; in this case hornblende is the most likely phase because of the composition of the rocks surrounding El Tatio sinter deposits. In addition, phlogopite peaks are similar to other micas like lepidolite, muscovite, siderophillite and illite.

Table 6. Mineralogy and XRD parameters for the El Tatio sinter samples

Sample ID	Silica phase	FWHM (°2θ)	Apex position (°2θ)	Maximum intensity (counts/sec)	Other minerals					
M2.1	opal-A	9.4	22.9	276	G					
M2.3	opal-A	8.3	22.5	230		H				
M3B	opal-A	12.5	23.7	174	G	H				
M3R	-	-	-	-			F			
M3.2	opal-A	8.2	22.8	203		H				
M4.1	opal-A	-	-	-		H				
M4.2	opal-A	7.8	22.4	321	G	H				
M5	opal-A	7.9	22.2	287	G	H				
M6.4	opal-A	8	22.8	327			F	T	N	L

Capital letters indicate the presence of mineral phases: G= Gypsum; H= Halite; F= Flower-like aggregates of bladed Si, Ca, As-rich crystals; T= Tetrahedral Ca-As crystals; N= Needle-like Si-Ca-As crystals; L= Lamellar As-Ca crystals. These minerals were identified by SEM observation and SEM-EDS analyses.

IV.3.   Stratigraphic sequence of sinter samples

Based on the SEM observations, a sequence of the sinter textures and mineralogy is determined. This requires the analysis of a section perpendicular to the laminations, which can be attained for samples M2.1, M2.3, M3, M4.1 and M5. The formation sequence of these samples is shown in Figure 18, where variations of sinter textures and mineralogy and thus the variations of physicochemical and hydrodynamic conditions of sinter formation can be tracked from the surface of the deposit.

The textural variations observed in sample M2.1 are dominated by intercalations of massive and porous layers. Porous silica layers are formed by coalesced opal-A spheres and void spaces between them; their thickness varies between 2 and 30 μm. Individual massive silica layers are 1-2 μm in width, yet they occur stacked. Silica platelets are found at the top of the deposit.

Sample M2.3 is characterized by three separate precipitation cycles that start with massive silica laminations over which lithic fragment-rich layers of variable thickness are deposited, and subsequently overlaid by filament-rich horizons. No platelet surficial horizon was identified, although it was only 1 meter away from sample M2.1.
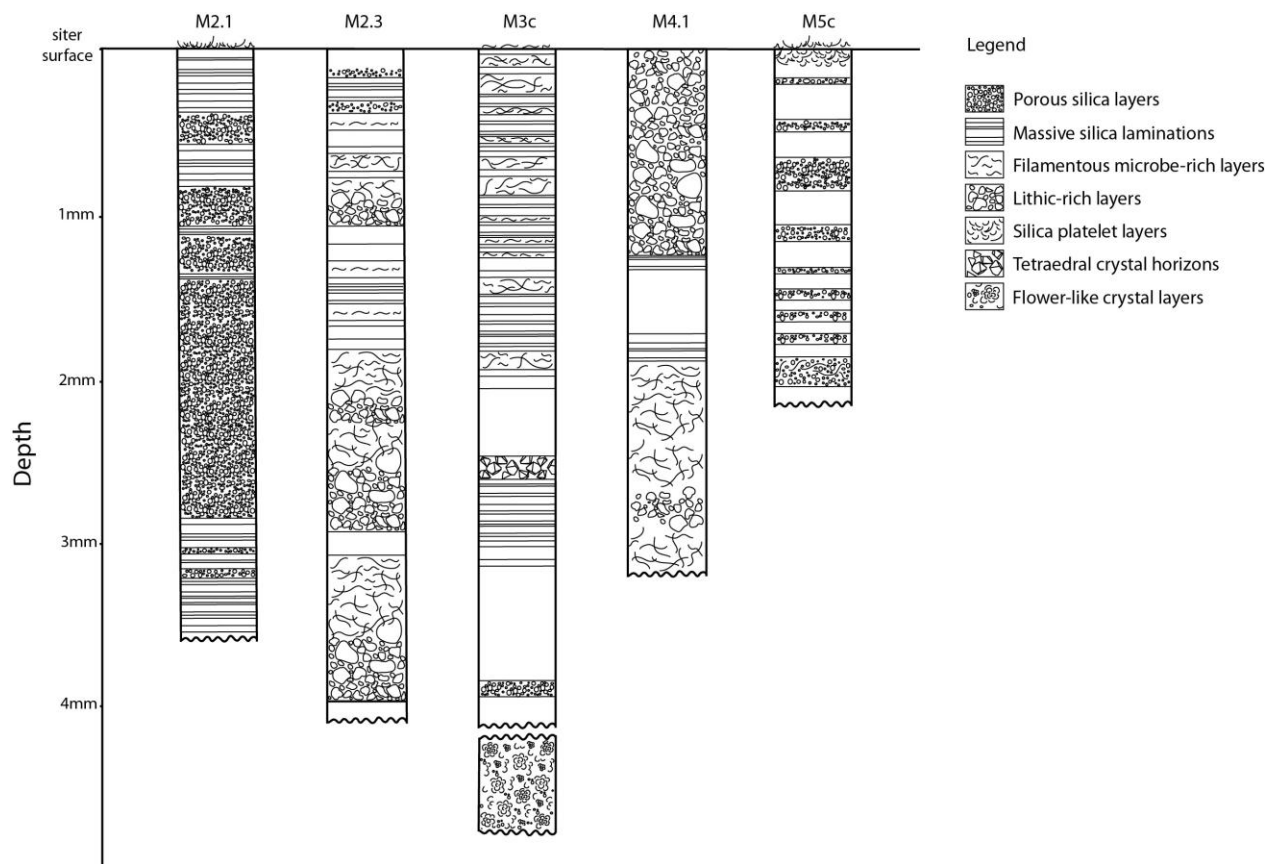
Figure 18. Stratigraphic columns of El Tatio sinter samples.

Macro-to micro-scale inspection of one spicule from sample M3 reveal strong textural and mineralogical variations. At a macroscopic scale, red porous friable horizons are interlayered with white sinter laminations, one of which, located at the base

38

of sample M3c. SEM observations of this red horizon indicate that it is formed by flower-like Si, As and Fe-rich crystals. This is in agreement with the chemistry of red material from sample M3 that is dominated by Fe, as shown in Table 7. The mineralogy of the deposit situated over this red horizon is dominated by opal-A spheres, forming massive and porous layers, some of which show abundant microbial population. Between silica laminations, one 100 μm thick layer formed exclusively by tetrahedral Ca and As-rich crystals and their dissolution products, scarce layers formed only by the dissolution product of tetrahedral crystals are also identified.

Sample M4.1 textures include lithic fragments and microbe-rich layers, massive and laminated silica layers, with no mineralogical variations. There is no regularity in the sequence of textures.

Textures of sample M5 are very similar to those of sample M2.1, showing interlayered porous and massive silica horizons. The hydrodynamic conditions of both sites are also similar, with a relatively quiet non surging pool and some eruptive events which are more frequent at site 2.

Regarding sample M6.4, it is important to note that it was not possible to reconstruct the complete formation sequence due to sample material limitations. However, primary cavities were recognized to host lamellar crystals, tetrahedral crystals, and needle-like crystals or nano-spheres of opal-A.

IV.4.   Chemistry of sinter samples

The chemical composition of the collected samples is summarized in Table 7 and the complete results are presented in APPENDIX I. Silica content of sinter samples varies between 41 wt% and 85 wt%. Sample M3R (red friable material interlayered with white laminations) has a SiO_2 content of 8.1 wt% and thus cannot be classified as sinter. Instead, the total iron content (expressed as Fe_2O_3) of sample M3R is the highest of all samples (18.75 wt%); among the rest of the samples, M3B and M2.3 show the highest content of iron (3.2 wt% and 2.9 wt%, respectively), and samples M4.2 and M5 show the lowest (0.4 wt% and 0.2 wt%, respectively).

In the strictly sinter samples (>40 wt% SiO_2), the chlorine contents range between 0.1 wt% and 2.6 wt%, and sodium content varies between 0.6 wt% and 3.4 wt%. Samples that show the highest (M2.3 with 2.7 wt%) and the lowest content of chlorine (M6.4 with 0.1 wt%) also show the highest (M2.3 with 3.4 wt% Na_2O) and lowest content of sodium (M6.4 with 0.8 wt% Na_2O), suggesting that these elements might be related to the presence of halite in the sinter deposit. Samples M2.3 and M3.2 show the highest contents of aluminum (with 5.9 and 3.9 wt%, respectively) and MgO (with 2.8 and 0.6 wt%, respectively), most likely related to lithic/mineral fragments over which the sinter was formed.

Table 7. El Tatio Geothermal field sinter samples chemistry.

		DL	M2.1	M2.3	M3B	M3R	M3.2	M4.2	M5	M6.4
SiO_2	wt%	0.01	64.15	59.58	41.08	8.10	70.09	73.25	85.04	77.63
Al_2O_3	wt%	0.01	0.62	5.85	0.76	0.81	3.86	0.97	0.67	1.98
$Fe_2O_3^{(T)}$	wt%	0.01	0.87	2.88	3.16	18.75	1.53	0.44	0.23	1.73
MnO	wt%	0.001	0.2	0.146	1.093	0.811	0.184	0.013	0.006	0.043
MgO	wt%	0.01	0.22	0.79	1.64	0.24	0.63	0.08	0.06	0.27
CaO	wt%	0.01	3.46	2.83	7.26	8.59	3.72	0.38	0.56	2.07
Na_2O	wt%	0.01	2.17	3.36	0.55	0.70	1.6	0.72	0.96	0.79
K_2O	wt%	0.01	0.54	1.12	0.31	0.49	0.91	0.5	0.43	0.39
Cl	wt%	0.01	1.54	2.67	0.2	0.71	0.48	0.47	0.56	0.14
Total S	wt%	0.01	0.11	0.06	0.07	0.08	0.13	0.04	0.02	0.05
B	ppm	2	8440	3820	4330	717	5790	2040	2180	1890
Cu	ppm	10	50	110	90	50	220	20	30	< 10
As	ppm	5	> 2000	315	> 2000	> 2000	694	177	334	> 2000
Sb	ppm	0.5	> 200	> 200	> 200	> 200	> 200	> 200	> 200	> 200
Ag	ppm	0.5	0.6	1.2	< 0.5	0.6	2.4	0.8	0.6	< 0.5
Pb	ppm	5	< 5	12	10	56	9	5	< 5	9
U	ppm	0.1	0.3	2	0.3	0.5	1	0.4	0.4	0.9
Hg	ppm	0.005	3.96	4.68	>100	>100	5.28	3.4	0.88	>100

DL=detection limit.

The boron content of all samples is high, reaching 0.8 wt% (8000 ppm) in sample M2.1. Arsenic is higher in samples M2.1, M3B, M3R and M6.4 (>0.2 wt%, >2000 ppm), although all samples show a high content of this element, and the antimony content of all samples exceeds the upper detection limit of 200 ppm.

IV.5.   Thermal water chemistry

Thermal waters at El Tatio geothermal field are classified as sodium-chloride waters based on the Piper classification (Piper, 1953). Table 8 shows the concentration of all the analyzed elements for each sampling site. All samples show high concentrations of dissolved silica (147 - 285 mg/l SiO_2), calcium (156 - 306 mg/l) and potassium (192 – 848 mg/l). The arsenic content is high in all samples (>17 mg/l), but the highest value occur at sites 4 and 5 (31 mg/l). The sulfur content is higher at site 3 (377 mg/l), intermediate at site 2 (104 mg/l) and site 6 (145 mg/l), and low at sites 4 and 5 (<90 mg/l).

Table 8. El Tatio thermal springs geochemistry.

sample ID	site 2	site 3[*]	site 4	site 5	site 6	site 3[**]	site 3[**] B4	site 3[***]
E	601057	601023	601932	602417	601730	601023	601023	601023
N	7529545	7529497	7530315	7530530	7528814	7529497	7529497	7529497
T	86.2	82.3	82.7	76.9	87.6	84	68.3	84.2
pH	7.4	6.5	7.3	7.1	7.4	6.8	7.3	6.5
Ca	157	158	268	292	307	129	130	125
K	239	236	849	534	192	215	216	209
Mg	6.4	5.8	0.3	0.6	2	4.7	4.8	4.5
Na	2230	2200	4678	4212	3555	2064	2080	1976
B	40	41	84	82	71	107	108	104
Ba	8.9	9.4	7.3	3.8	4.4	-	-	-
Fe	0.11	0.16	0.01	0.01	0.01	0	0	0
Li	24	24	61	59	42	20	20	19
Mn	0.5	0.4	0.2	0.1	0.1	0.4	0.4	0.4
Sr	2.3	2.3	4.3	4.6	4.4	2.4	2.4	2.3
Si	69	69	133	104	104	65	65	62
SiO_2	147	147	285	223	223	140	140	133
As	18	18	31	32	25	17	18	18
Cl	4211	3480	9119	8819	6995	4033	3478	3913
Br	16.6	154.5	91.2	93.4	89.3	14.7	14.5	15.0
SO_4	105	378	89	81	146	44	37	39
HCO_3	117	131	4.3	0	32	119	100	135

Temperatures are in °C. Concentrations are expressed in mg/l.
* january 2012; **march 2012; ***april 2013. B4 refer to the fourth position along the discharge channel at the site of the silica precipitation experiment.

Based on the amount of mixing between thermal water and meteoric inputs can be inferred based on the content of conservative elements (e.g., Cl and Li) and bicarbonate. The selected sites can be separated in three compositional groups: sites 4 and 5 show the higher concentration of chlorine (>8800 mg/l) and lithium (~60 mg/l), and the lower concentration of bicarbonate (<5 mg/l), which indicate that there is a minor influence of meteoric water. Conversely, sites 2 and 3 show the lowest concentration of chlorine (<4200 mg/l) and lithium (~24 mg/l), and the highest concentration of bicarbonate (>100 mg/l), which indicates a higher amount of mixing with meteoric water. The chemistry of site 6 shows a moderate degree of mixing with meteoric water.

IV.6. Silica precipitation rate

The environmental conditions measured at site 3, where the silica precipitation rate experiment was developed, are summarized in Table 9. At the beginning of the experiment, the wind velocity was measured between 3.7 and 7.5 m s^{-1}, and the wind direction was predominantly east, at every time of slides collection. The empirical average evaporation rate is 0.17 ml/min.

Table 9. Environmental conditions at the site of silica precipitation experiment (site 3).

Position	Distance from pool (m)	Water flow (m s^{-1})	Humidity (%)	Wind velocity (m s^{-1})	Water temperature (°C)
P1	0.74	0.0025	64.2 - 89	3.7 - 6.3	72.4
P2	3.24	0.0039	124	5.1 - 7.2	66.2
P3	6.84	0.0021	88.9 - 111.7	3.4 - 6.1	62.7
P4	9.84	0.0024	32 - 45.2	4.8 - 7.5	57.4

The experiment carried out along the discharge channel of a bubbling hot pool indicates that sinter precipitates at an average rate of 0.9 mg day^{-1} slide^{-1}, considering both parallel and perpendicular slides. The silica precipitation rate is significantly higher in slides that are placed perpendicular to the water flow (1.2 mg day^{-1} slide^{-1}) than in those set parallel to it (0.46 mg day^{-1} slide^{-1}). The calculated silica precipitation rate at each position along the discharge channel is detailed in APPENDIX V.

The distance between the pool and the slides influence the water temperature, and the amount of silica precipitation, as shown in Figure 19. The precipitation rate on slides parallel to water flow show higher precipitation rate in position 1 and 4, and lower precipitation rate in position 2 and 3, although this pattern cannot be recognized in January-October samples. On slides perpendicular to the water flow, the precipitation rate tend to be higher in positions 2 and 3, and lower in positions 1 and 4, although this pattern is only clear in January-March and January-October samples.
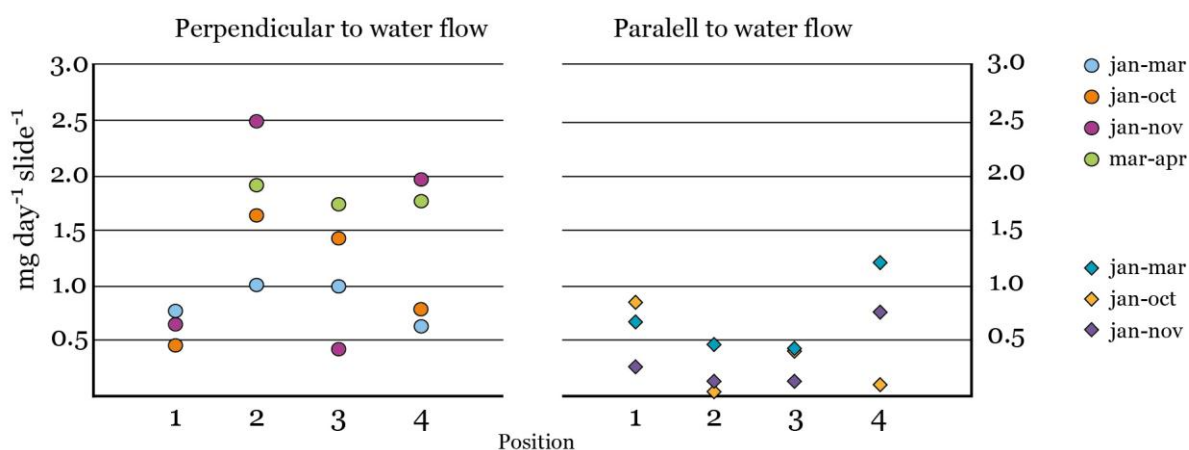
Figure 19. Silica precipitation rate for the different samples placed at the four positions along the site of experiment discharge channel. Right and left vertical axes are in the same units. Samples are labeled according to the month of their placement in site and the month of collection.

Precipitation occurred preferentially in the sub-aerial zones of the slide where the precipitate crust is mainly composed of white silica. Poorly developed orange-colored Fe and As-rich crust is found at the water-air interface and in sub aquatic areas, where organic material is more abundant (Figure 20). This newly deposited siliceous sinter shows a microscopic botryoidal morphology, composed of amalgamated opal-A microspheres (Figure 21).

In perpendicular slides, silica precipitation occurs almost exclusively on the pool-wards face of the slide, which is the side facing the water flow. The only exceptions are the slides from position 4, where silicification of microbial mat occurs also at the back side of the slide. This leads to a higher precipitate weight measured in the slides form position 4.

Sinter is vertically laminated and massive in samples 2, 9 and 10 months old; incipient spicular texture development is observable in samples that are 15 months old.
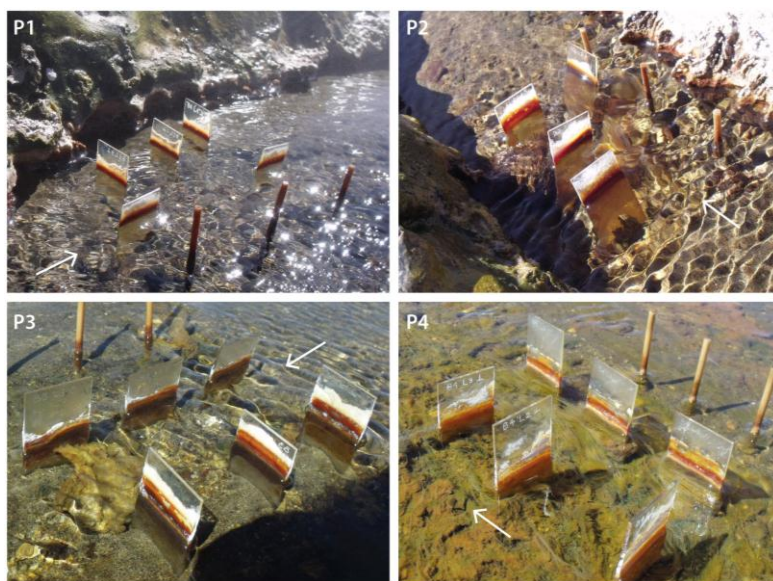
Figure 20.Glass slides two months after the beginning of the silica precipitation experiment at site 3. The precipitate consists of a white crust formed under sub aerial conditions and mainly composed of amorphous silica, a reddish horizon formed at the air-water interface, and a brownish microbial mat plus minor halite crystals and silica crust formed under sub-aquatic conditions. Note the increasing amount of biological material from position 1 to 4. Glass slides are ~3 cm wide.
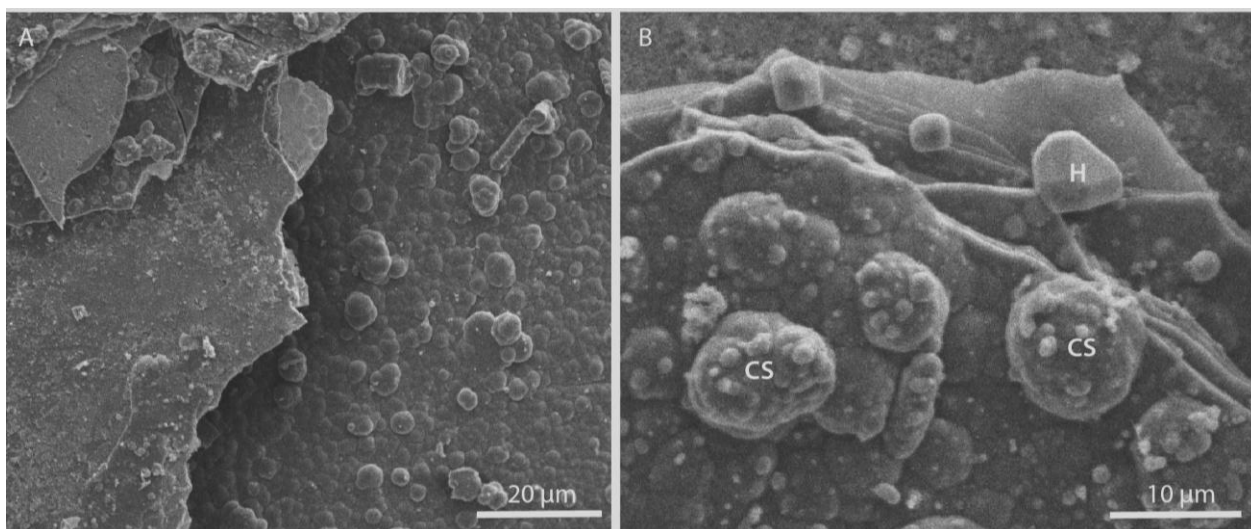
Figure 21. SEM images of opal-A morphology in a slide from position 3 of the silica precipitation experiment. A: vertically laminated deposit and botryoidal clusters of opal-A spheres. B: Opal-A coalesced spheres (CS) and halite crystals (H).

CHAPTER V   DISCUSSION

Siliceous sinter formation is a common process that occurs in the discharge zones of alkali-chloride and silica-saturated thermal waters that are commonly associated with high temperature geothermal systems (Fournier and Rowe, 1966; Ellis and Mahon, 1977; White *et al.*, 1992; Fournier *et al.*, 1994; Nicholson, 1988; Herdianita *et al.*, 2000; Guido *et al.*, 2002; Pirajno, 2010). Sinter textures are closely related to the hydrodynamic and environmental conditions under which silica precipitates, and are greatly influenced by the microbiota that thrives in the thermal waters (Cady and Farmer 1996; Campbell *et al.* 2001; Lowe *et al.* 2001; Lowe and Braunstein 2001; Lynne *et al.*, 2003; Guidry and Chafetz 2003a, Schinteie *et al*, 2007).

In this chapter, the detected variations in opal-A morphology and crystallinity in the El Tatio sinter deposits are compared to other sinter deposits from New Zealand. As well, the influence of chemical variations of thermal waters on the mineralogy of newly forming El Tatio sinter is discussed, along with the influence of environmental and hydrodynamic conditions over the observed sinter textures.

V.1. Mineralogy and chemistry of the El Tatio siliceous sinter deposits

The siliceous sinter deposits from El Tatio are mainly constituted by individual and amalgamated nano- and micro-spheres that correspond to opal-A. Bumpy micro-spheres formed by smaller amalgamated micro-spheres are recognized in few samples. Similar bumpy spheres are reported by Lynne *et al.* (2005) in Opal Mound Sinter. In the diagenetic sequence of Opal Mound, botryoidal clusters of amalgamated opal-A micro-spheres increase their bumpiness to from bumpy microspheres that subsequently reorganize and decrease in size to from clusters of nano-spheres which correspond to opal-A/CT (Lynne *et al.*, 2005). Thus, the bumpy spheres identified in the El Tatio sinters correspond to a transitional phase from opal-A to opal-A/CT, and evidence the presence of a slightly more mature phase than opal-A. Nevertheless, the El Tatio sinters are in an early stage of diagenetic maturation, according to the results of this work, which is confirmed by the shape of the diffraction bands in the XRD traces (FWHM of

7.8 to 12.5 °2Ɵ). This is in agreement with previous studies at El Tatio, where minor occurrence of more mature silica phases such as opal-A/CT and opal-CT has been reported (García-Valles *et al.*, 2008).

Silica phase crystallinity is determined by XRD analysis of sinter samples, by calculating the FWHM value. The phase that initially precipitates is the least mature silica phase, opal-A, whose typical FWHM values vary between 6 and 8°2Ɵ (Lynne and Campbell, 2003, 2004; Lynne *et al.*, 2005). Opal-A can undergo a series of processes that change one silica phase into another, eventually transforming into quartz, the most mature silica phase. Through this process, the FWHM value decreases as silica phase maturity increases, reaching <0.15 °2Ɵ (Figure 22; Cady and Farmer, 1996; Campbell *et al.*, 2001; Guidry and Chafetz, 2003; Lynne and Campbell, 2003; Lynne and Campbell, 2004; Lynne *et al.*, 2005).

Studies in other sinters from Opal Mound, Steamboat Springs (U.S.A.) and Sinter Island (New Zealand) show that this diagenetic maturation process does not directly relate to the age of the deposit, and can be accelerated by post-depositional processes such as acidic steam overprinting and thermal water injection (Lynne *et al.*, 2006, 2007). Experimental studies show that the FWHM value increases when sinter is exposed to fumarolic steam condensate (from 7.2 to 8.6 °2Ɵ; Lynne *et al.*, 2006).

The analyzed sinter samples from El Tatio show an extremely low degree of structural order, evidenced by the high FWHM values (8 – 12.5 °2Ɵ). High FWHM values are expected, as sinter deposits are mainly formed by the least mature silica phase, opal-A. Nevertheless, for El Tatio sinters the FWHM values are higher than those typically reported for USA and New Zealand sinters. A mineralogical study of El Tatio sinters by García-Valles *et al.* (2008) have also reported high FWHM values (up to 10 °2Ɵ), suggesting that these values are increased by the simultaneous occurrence of silica phases (opal-A and/or opal-A/CT) and other crystalline phases (halite, sylvite, realgar, sassolite and/or teruggite). This would be in agreement with the high FWHM values observed in this study, where silica co-exists with other mineral phases such as cahnite, flower-like and needle like aggregates.
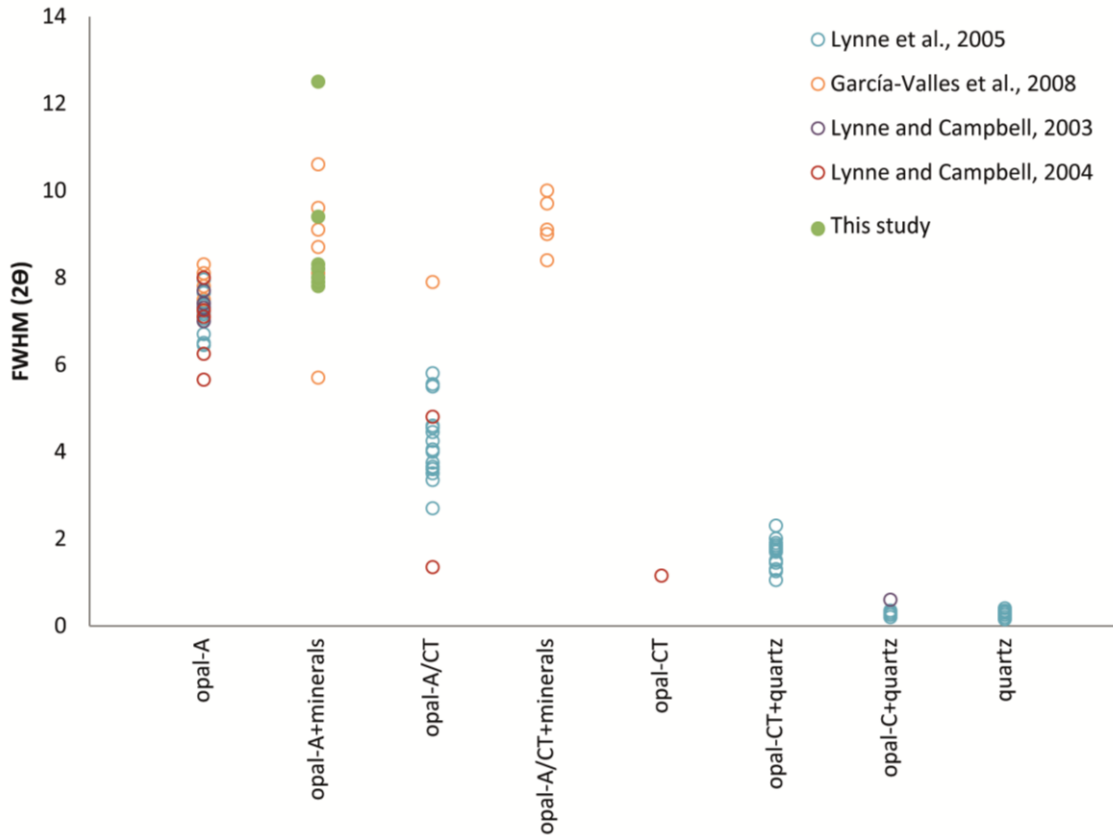
Figure 22. Full Width at Half Maximum (FWHM) values of the different silica phases of siliceous sinter deposits. El Tatio sinters (this work and García-Valles *et al*., 2008) show higher FWHM values compared to Opal Mound sinters, USA (Lynne *et al*., 2005), and Orakei Korako, Waiotapu, Te Kopia and Umuruki sinters, New Zealand (Lynne and Campbell, 2003, 2004).

However, another possible and more likely explanation for the high FWHM values of the El Tatio sinters is the incorporation of cations into the silica structure, increasing the structural disorder of the silica phase (Figure 23). This is supported by the SEM-EDS analyses of opal-A micro-spheres that show detectable amounts of calcium and sodium. The incorporation of cations into the silica structure might be promoted by fast silica precipitation due to high evaporation rate, and/or high cooling rate due to low environmental temperatures.

The analyzed sinter samples from El Tatio show an extremely low degree of structural order, evidenced by the high FWHM values (8 – 12.5 °2ɵ). High FWHM values are expected, as sinter deposit is mainly formed by the least mature silica phase, opal-A. Nevertheless, El Tatio sinters FWHM values are higher than those typically

reported for USA and New Zealand sinters. A mineralogical study of El Tatio sinters by García-Valles *et al.* (2008) have also reported high FWHM values (up to 10 °2θ), suggesting that these values are increased by the simultaneous occurrence of silica phases (opal-A and/or opal-A/CT) and other crystalline phases (halite, sylvite, realgar, sassolite and/or teruggite). This would be in agreement with the high FWHM values observed in this study, where silica coexists with other mineral phases such as cahnite, flower-like and needle like aggregates.
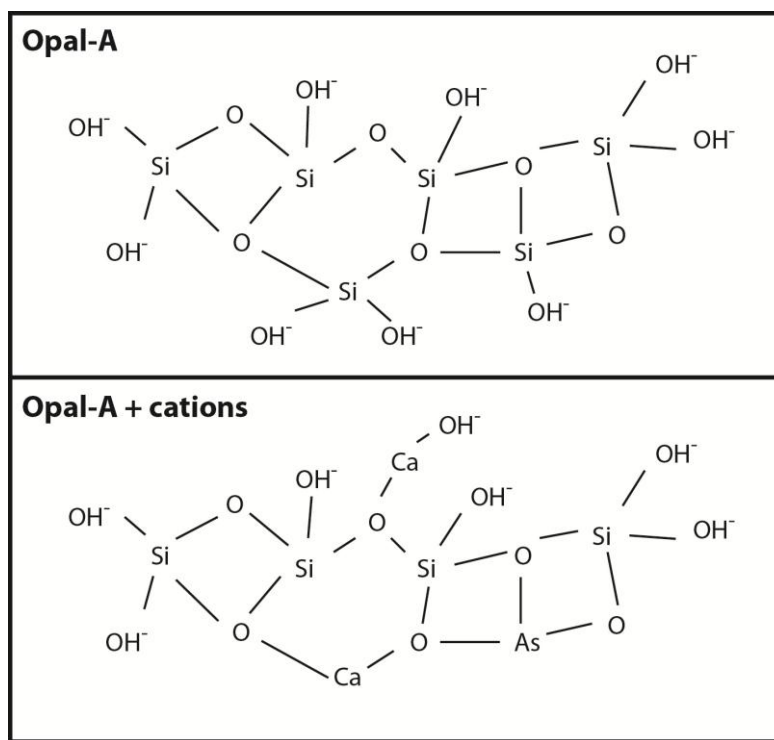
Figure 23. Schematic diagram of the atomic arrangements of pure
opal-A (up) and cations incorporated into the opal-A structure (down).

The highest FWHM vale is measured in sample M3B (12.5 °2θ), which also shows the highest concentration of calcium (7.26 wt% CaO) and arsenic (>2000 ppm). This sample also shows the highest concentration of iron (3.16 wt% total iron as Fe_2O_3) and the lowest value of XRD maximum intensity (174 counts/seconds). It has been previously documented that iron absorbs radiation at the Cu X-ray emission wavelength, which affects the resulting XRD trace, decreasing the maximum peak intensity (Lynne, 2007). However, a change in the peak intensity would not affect the FWHM value.

The mineralogy of the El Tatio siliceous sinters is also characterized by the common presence of accessory crystalline phases such as halite, gypsum and cahnite. The occurrence of these minerals is related to the high concentration of sodium, calcium, sulfur, arsenic and boron in El Tatio thermal waters. Their precipitation is possible because the sinter formation process occurs mainly by evaporation to dryness, while their preservation requires that no wetting occurs after their precipitation.

The occurrence of cahnite ($Ca_2B[OH]_4[AsO_4]$) in sample M6.4 is suggested by the presence of crystals that show the same chemistry and morphology under SEM observation, but were not detected by XRD. The presence of cahnite at El Tatio is not surprising, as other arsenic minerals such as teruggite ($Ca_4MgAs_2B_{12}O_{28} \cdot 20H_2O$) and nobleite ($CaB_6O_{10} \cdot 4H_2O$) have been previously reported at El Tatio (Rodgers *et al*, 2002b, García-Valles *et al*., 2008). Teruggite, nobleite and cahnite are also found in borate deposits in Turkey and Argentina, where its formation is directly linked to boron-rich thermal waters or salar brines (Helvaci and Alonso, 2000).

Calcium and arsenic-rich minerals are found filling cavities and constituting laminations within the sinter deposits. The infilling of cavities consists of needle-like crystals and/or tetrahedral crystals (cahnite). The fact that the two phases occur growing with each other in some cavities indicates that they most likely co-precipitated from the same fluid. This secondary fluid requires to be highly enriched in calcium and arsenic (and boron), which can be attributed to evaporation the primary thermal water, followed by a subsequent precipitation of silica. This highly concentrated water, enriched in calcium and arsenic, would infiltrate down the sinter deposit through the primary porosity, and precipitate out the observed arsenic and calcium minerals in cavities and micro fractures. This process would explain arsenic borates occurring as cavity infill, yet it does not explain the continuous laminations formed by these minerals found in sample M3B.

Nevertheless, this secondary fluid, responsible for the precipitation of the borates, would also be enriched in chloride and sodium after the precipitation of silica at the surface of the deposit. Precipitation of halite should occur after the precipitation of

calcium and arsenic borates, because halite solubility (~40 g per 100 g of water, at 25 °C; Petrucci *et al.*, 2002) is higher than the solubility of boric acid and sodium borates (5 - 25 g per 100 g of water, at 25 °C; Blasdale and Slansky, 1939), which are considered to be similar to calcium and arsenic borates, since there is no available data for these phases. However, no halite crystals were observed in the borate-infilled cavities, which can indicate that the precipitation of halite occurred in a stratigraphically deeper horizon, or that the halite did precipitate with the borates but was washed out from the borate-infilled cavities.

Regarding the bulk chemical composition of the El Tatio sinters, they show a SiO_2 content between 41 and 85 wt%, which is considerably lower than other documented sinters in USA, New Zealand and Japan (Table 1), this would be influenced by the high content of other elements and compounds in El Tatio sinter samples, which reach up to 17 wt%. The common occurrence of accessory minerals constituted by elements such as Ca, S, Na, Cl, As and B is possible due the high content of these elements in the thermal waters, and the sinter formation process through evaporation to dryness, which allow the precipitation of extremely soluble minerals. Nevertheless, the sum of all the analyzed elements and compounds of all the samples in this study varies between 56 and 88 wt% (Table V.1 in APPENDIX I), which may indicate a high content of volatile compounds, such as interstitial water, in the sinter samples. However, the amount of available sample precluded Loss On Ignition measurements.

Apart from SiO_2, the chemical composition of El Tatio sinter deposits is characterized by calcium and aluminum, followed by iron, sodium, and chlorine (Table 7). The high contents of calcium are in agreement with the occurrence of gypsum and cahnite. Moreover, calcium content is higher in sample M3, where cahnite was detected by XRD analysis and SEM observations. Likewise, sodium and chlorine content is most likely linked to the frequent occurrence of halite in almost all samples. The contents of aluminum and at least part of the other elements are probably linked to lithic material incorporated in the sinter deposit, such as detrital fragments of plagioclase, amphiboles and micas (also detected by XRD analysis and observed by SEM).

Iron is probably the only element linked with the particular coloration of some sinters from El Tati, since the samples taken from sites 4 and 5 are white and show a lower iron concentration compared to those from sites 2, 3 and 6, where red laminations and/or red crust are observed at the water-air interface. Hydrous ferric oxides have been reported to occur at El Tatio by Alsina *et al.* (2008, 2013), yet they were not identified and characterized in this work.

The average content of iron of El Tatio sinters (3.2 wt% Fe_2O_3) is higher than that of Atiamuri, Champagne Pool, Ohaaki and Tokaanu in New Zealand (0.36 wt% average Fe_2O_3) and Yellowstone National Park (0.58 wt% average Fe_2O_3) in U.S.A., according to the data of Nicholson and Parker (1990), Yokoyama *et al.* (2004) and Fournier *et al.* (1994).

Regarding the trace element composition, El Tatio sinter deposits are highly enriched in boron and arsenic, with an average content of ~4 wt% and ~1 wt%, respectively. The content of these elements is probably linked to cahnite or other arsenic-rich borates occurring in the sinter samples. Nevertheless, high contents of arsenic and boron are observed in samples M2.1, M3.2, M3B and M2.3, where cahnite was not identified by SEM observation nor using XRD. This can be interpreted as arsenic-rich borates are common at El Tatio sinters, but still in amounts low enough to be undetectable by XRD analysis (<2 %).

The results of this study indicate that sinter chemistry and water chemistry are closely linked, especially when the processes leading to sinter formation are related to evaporation to dryness, since all components in water must precipitate out when water reaches complete evaporation. The high calcium, boron, sulphur and arsenic contents of El Tatio thermal waters result in the precipitation of evaporitic minerals such as halite, gypsum and cahnite. Nevertheless, the variations detected in the concentration of these elements between the thermal waters from the analyzed sites are not reflected in the abundance of accessory minerals in the associated sinter deposits. For example, cahnite was detected in sites 3 and 6, even though the thermal water from site 3 is mixed with

meteoric water, and thus its arsenic, boron and calcium content is lower than the thermal water from site 6, which are not diluted, and yet cahnite is present in both sites.

However, it is likely that variations in thermal water chemistry occurred through time, mainly due to the effect of meteoric water dilution, considering the fact that the deep hydrothermal reservoir is at equilibrium. Thus, the effect of a higher meteoric influence in thermal water chemistry is expected to be related to rainfall during the South American Summer Monsoon (November to March according to Zhou and Lau, 1998). Chemistry variations as a function of time were monitored in site 3; most elements show variations of less than 10 %, but boron and sulphur show higher variations (45 % and <80 % respectively).However, the content of these elements in site 3 is always lower than in sites 4, 5 and 6, which belong to the group of thermal springs less affected by meteoric influence.

Even though the measured chemical variations of thermal waters are relatively small, the water from which arsenic borates precipitated as continuous laminations (M3B, APPENDIX IV, Figure IV.5B, G) must have a much higher content of boron, calcium and arsenic. This higher concentration can be related to thermodynamic changes in the deep geothermal system, or evaporation processes that increases concentration of all elements in solution. To fully understand the origin of the arsenic borates identified in El Tatio sinter deposits further studies are needed, e.g., constrain the variation in the boron, calcium and arsenic contents of thermal waters over longer timescales, determine the thermodynamic conditions under which the precipitation of these minerals occur, and elucidate their isotopic signature and fractionation processes (e.g., stable isotopes of B)

V.2.The El Tatio high-altitude sinters: a comparison with low-altitude siliceous sinter deposits

Silica precipitation under El Tatio's extreme environmental and altitude conditions has been scarcely studied. For example, Channing and Butler (2007) show that experimental sub-freezing, cryogenic precipitation of silica from sodium-chloride

and silica-rich solutions produce a characteristic sinter micro-texture defined as particles that exhibit branching, swellings and are commonly terminated in "tear-drops", folded sheets and structurally complex particles. These experimentally-produced particles show a great resemblance with the textures observed in sinter samples from the Yellowstone National Park, in USA (Channing and Butler, 2007), which is located at a lower altitude (~2500 m above sea level; thermal waters at 93 °C, with silica concentration of 750 ppm SiO_2).

In this study, we report a different micro texture that might have an origin related to sub-zero temperatures and high altitude (>4200 m above sea level): silica platelets (Figure 15B, Figures IV.2 and IV.11 in APPENDIX IV). The formation of this textural type begins with silica precipitation to form an individual micron-scale lamination. Sub-zero environmental temperature leads to the freezing of interstitial water in this recently formed silica layer, increasing the volume of water and thus fracturing the recently formed silica layer. The rise of the environmental temperature leads to unfreezing and disarticulation of the broken silica platelets, which can be re-cemented by subsequent silica precipitation. The scarcity of this texture can be explained by cementation of silica platelets to generate a wider massive silica lamination. The high altitude conditions allow the great atmospheric oscillation that leads to the night-day freezing-unfreezing cycles (Figure 24).

Similar "sheet or flake-like amorphous silica particles" formed by freezing of silica rich solutions have been described by Iler (1979). The formation of ice crystals induce the polymerization of colloidal silica in the solution surrounding the ice particles, leading to the formation of irregular shaped silica flakes between the flat surfaces of ice crystals (Iler, 1979). However, these silica flakes are 20 – 30 Å in diameter (Iler, 1979), and thus, are considerably smaller than the 15 – 30 μm diameter silica platelets identified in samples M2.1 and M5.

Micro-columns and ridges are observed at the surface of El Tatio geyserite deposits formed around eruptive pools. These sinter textures can be partially biotically and partially abiotically produced, because silicified microbes were observed in sample

M3, while they were not detected in sample M4. A mixture of two abiotic processes might originate this sinter texture. (1) The first corresponds to locally differential precipitation rates originated by ice particles. The freezing of the thermal water at sub-zero temperature conditions, leads to the concentration of all dissolved components in water in the surroundings of the ice particles, which locally enhance the precipitation of silica. The locally differential silica precipitation would originate a topographic difference between the surfaces that have ice particles above and those that lack ice.
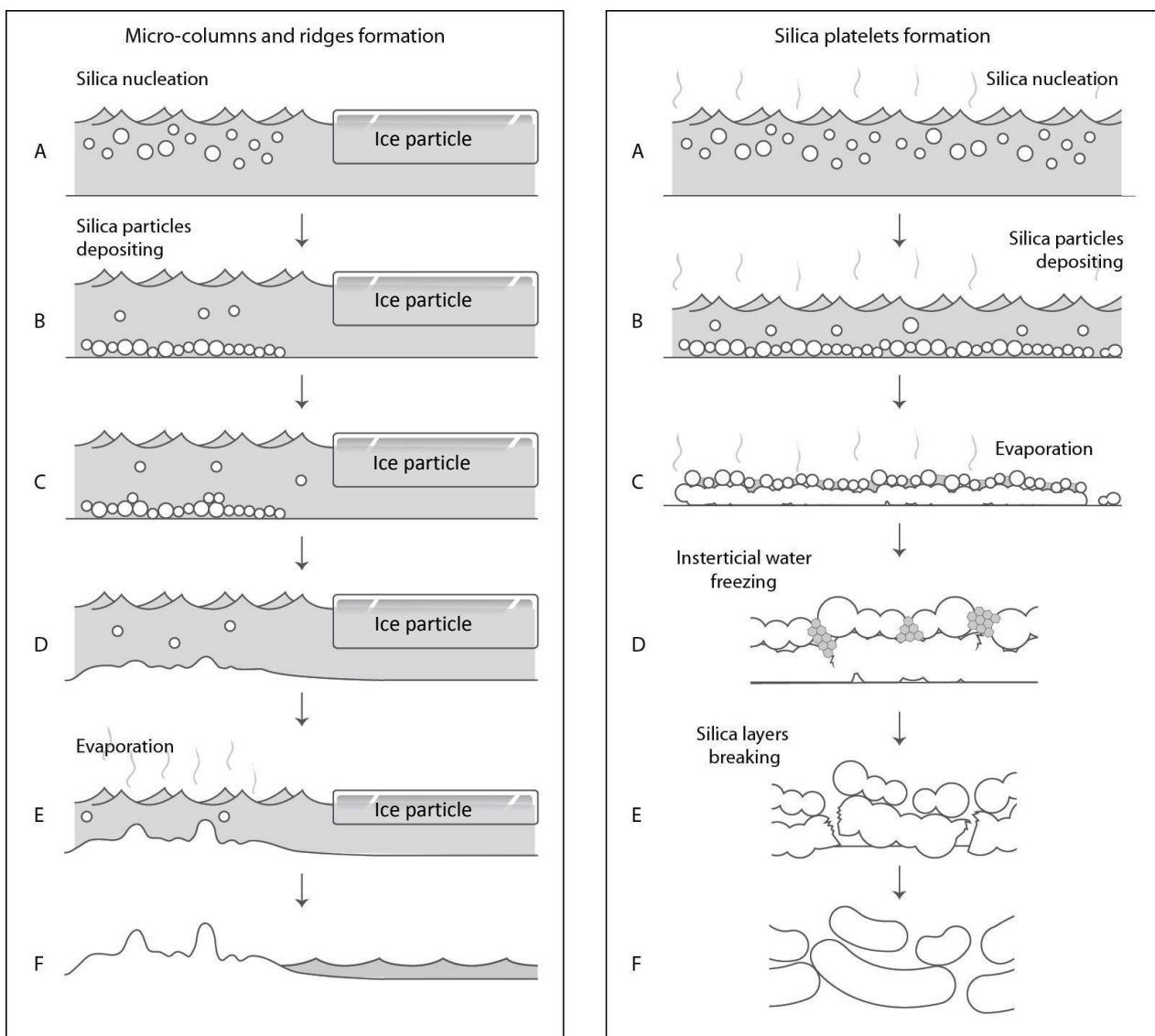
Figure 24. Formation of freezing related textures at El Tatio geothermal field. Left image: Micro columns and ridges formation is influenced by two processes: 1) the increase precipitation rate in the surroundings of an ice particle, and 2) by the contrast in evaporation rates between topographically-high and -low zones. Right image: Silica platelets formation is related to the freezing of interstitial water that leads to the rupture and disarticulation of individual silica layers.

(2) The second possibility is linked to the contrast in evaporation rates between topographically-high and -low sites. According to Lynne and Boudreau (2012), topographically-high zones easily reach full evaporation, which may not be attained at topographically-low sites, where water remains between eruptive events. This leads to a higher precipitation rate at topographically-high zones, due to complete evaporation. Then, the origin of micro-column and ridge texture is related to a mixture of both processes, since the formation of ice particles in the cooled thermal water can generate a topographically high zone that is more favorable to show high silica precipitation rate, because it reaches complete evaporation.

Regarding microbial textures observed in the El Tatio sinters, the occurrence of silicified microbial filaments is common. They are usually 1 - 5 µm in diameter and thus are associated with mid - to - high temperature settings (35 – 90 °C; Cassie, 1989, Cady and Farmer, 1996). However, the co-existence of spicular sinter texture and mid-temperature microbial filaments (~1.5 µm diameter) in sample M3 is unique. In this case, the sinter sample was taken from a splash zone at a near-vent area of site 3, where the pool temperature ranges from 82 to 84 °C and the surgence is usually gentle with few eruptive events and overflowing. These infrequent splashing events are considered to be responsible for spicular texture formation and are related to boiling.

The occurrence of mid-temperature filaments at near vent setting, instead of high temperature microbes, is most likely related to the boiling temperature at high altitude, which is lower that at low altitude, and reaches only 86 °C at 4200 meters high. If water droplets at 86 °C are released from the pool in an eruptive event related to boiling, they cool fast enough before they land over the sinter deposit and the temperature they reach is cool enough to support mid-temperature microbial filaments. Therefore, at El Tatio, and probably in other high altitude sinter deposits in Chile and elsewhere, geyserite textures documented as indicatives of near vent and high temperature can coexist with microbial communities typical of mid-temperature settings. Thus, at high altitude, it is more accurate to interpret near vent settings based on sinter textures (e.g., spicular, columnar or bulbous digitate textures).

However, the fact that the eruptive events are infrequent would also explain the occurrence of mid-temperature microbes. In fact, eruptive events occur every ~10 minutes at site 4, which would allow the high temperature water to cool to <59 °C. This would cause lower water temperature most of the time, allowing the proliferation of mid-temperature microbes. Then, when eruptions occur, the water temperature would rise, but not enough to kill the microbes.

The occurrence of microbial filaments of variable diameter in the same setting (~1 and ~10 μm diameter filaments in sample M3.2, and 2.5 and ~5 μm diameter filaments in sample M4.1) can be related to variations in the water temperature through time or to microbial adaptation to the variations of environmental conditions, which have been previously suggested by Franks (2012). However, more studies are needed to elucidate the effect of water temperature variations, freezing conditions and other physic-chemical characteristics of the thermal water over the microbiota that thrive in El Tatio springs.

Silica laminations, noticeable from the hand-scale to the micro-scale, are found in the El Tatio sinters, as well as in most sinters from other geothermal fields: Yellowstone National Park, in USA, Rotokawa, in New Zealand, Krisuvik, in Iceland (e.g. Lowe and Braunstein, 2001, Schinteie *et al*, 2007, and Konhauser *et al.*, 2001). Silica laminations are related to periodic wetting and drying events caused by overflowing or splashing and subsequent cooling and evaporation to dryness. Wave surges and fluctuating water level supply sinter surfaces with thermal water, allowing dissolved silica to become oversaturated and deposit as continuous layers (Schinteie *et al.*, 2007). Porous layers are interpreted to form at an initial wet state in which opal-A spheres suspended in water aggregate and/or coalesce and then gravitationally deposit over the surface.

Massive layers are interpreted to form at a subsequent drying state, in which water evaporation increases the silica concentration and oversaturation enhances silica deposition and increases the precipitation rate. Nevertheless, infiltration of silica-saturated water in this primary porosity might lead to the precipitation of silica cement in void spaces and the transformation of porous layers into massive layers (Jones and Renaut, 2003, Cady and Farmer, 1996). Thus, an interpretation of the number of wetting

and drying events that formed a particular sequence of porous and massive laminations cannot be determined.

Based on the experimental rate of precipitation of silica obtained for the El Tatio geothermal field (2.5 mg day^{-1} slide^{-1}= 1.8 kg year^{-1} m^{-2}), a rough estimation can be done of the time that would be necessary to form the large siliceous sinter deposits in that location. Considering that opal-A siliceous sinter deposits have an average density of 2 g/cm^3, and that at El Tatio sinter covers an approximate area of 2 km of length and 500 m wide, to a depth of 3 m. Then there are 6,000 kg/m^2 of sinter deposited at El Tatio. If the experimentally determined precipitation rate of 1.8 kg/m^2·year was constant through time, then it would take ~3,300 years to form the whole sinter deposits currently found in this area.

This calculation has many limitations, such as: (1) the amount of silica that currently occurs at El Tatio could be overestimated, but no data of the precise extent or depth of the siliceous sinter deposits is available for this area, (2) it is possible that the precipitation rate varies through time, given that the silica concentration of thermal water might fluctuate, e.g. because of meteoric influence; and also considering that sinter deposition is not continuous through time, as hot spring can stop due to the sealing of the vent, (3) the experimental precipitation rate only takes into account the sub-aerial precipitation, and it is known that there is sub-aqueous precipitation, e.g. site 6 shows sub-aqueous precipitation of silica in the discharge channel, (4) erosion and dissolution are not taken into account. Nevertheless, this calculation gives a minimal estimation of the time since when this particular geothermal field has been active, discharging near neutral alkali-chloride waters, as the El Tatio sinters have not been dated.

Our experimental study of silica precipitation at El Tatio also provides clues to evaluate the effects of particular environmental conditions on sinter formation, in this case a high-altitude system with large atmospheric temperature oscillations. Silica precipitation rate is closely related to environmental factors such as evaporation rate, water waves and wind when it occurs sub-aerially (e.g. Handley *et al.*, 2005), although

chemical characteristics of thermal water, in particular silica saturation, plays an important role in silica deposition (e.g. Tobler *et al.*, 2008).

According to our experimental data, the sub-aerial silica precipitation at El Tatio occurs at an average rate of 0.9 mg·day^{-1}·slide^{-1} (~0.14 mm·month^{-1}·slide^{-1}) considering the slides located perpendicular and parallel slides to water flow, but is considerably higher in perpendicular slides (2.5 mg·day^{-1}·slide^{-1}). This is partly related to the amplitude of waves that provides silica-rich water for silica precipitation through evaporation. Higher waves occur over the perpendicular slides, which offer more resistance to the water flow. Additionally, physical erosion of silica particles may occur in the parallel slides due to the higher velocity of water that flow around them. Erosion may also occur in the back side of perpendicular slides precluding the silica accumulation, which is observed in all the slides collected through the experiment.

Silica precipitation rate has been experimentally measured at Reykjanes and Svartsegi, Iceland (Tobler *et al.*, 2008), where sub-aqueous precipitation rate ranges from 10 to 304 kg·m^{-2}·year^{-1}, in a spring at pH ~7 and 42 - 75 °C, similar to El Tatio site 3, where slides were positioned along the discharge channel that show a range of temperature from 72 to 57 °C. The precipitation rate at Reykjanes and Svartsegi is two orders of magnitude higher than that measured at El Tatio. This might be related to the silica content of thermal waters (250 - 695 mg/l at Reykjanes and Svartsegi versus 147 mg/l at El Tatio), and to the extreme freezing conditions, which enhance the silica precipitation rate at Reykjanes and Svartsegi.

Experimental studies have been undertaken also at Champagne Pool, Waiotapu, New Zealand (pH=5.5; T=75°C), where sub-aerial silica precipitation occur at a rate of 0.2 to 1.9 mg·day^{-1}·slide^{-1} (= 1 to 10 kg·year^{-1}·m^{-2}; Handley *et al.*, 2005), which is comparable to the rates obtained at El Tatio, although Champagne Pool is slightly acidic and show higher silica concentration (362 mg/l; Pope *et al*, 2004).

It is important to note that in this study, the precipitation rate experiment was undertaken at a site where thermal waters are diluted due to meteoric water influence.

Yet, precipitation rates are slightly lower than those obtained at Champagne Pool, where silica concentration in thermal water is double to that of the site of experiment at El Tatio. Therefore, it can be hypothesized that silica accumulation rate is enhanced by the high evaporation rate related to wind, aridity and high solar radiation at El Tatio. To confirm this, the same silica precipitation experiment should be developed at, for example, site 4, where silica concentration of thermal water is similar to that of Champagne Pool (285 mg/l).

CHAPTER VI   CONCLUSIONS

The study of thermal water and associated sinter deposits at the El Tatio geothermal field in northern Chile provides new insights into the characteristics of siliceous sinter deposits formed in the Andean context, and explores the influence of the chemical composition of thermal waters, along with the environmental and hydrodynamic conditions, over sinter textures, mineralogy and chemistry.

El Tatio's thermal water chemistry is dominated by high concentrations of silica, chlorine, arsenic and boron, and the environmental conditions of its location are characterized by the high altitude, high evaporation rates and thermal oscillation. These characteristics conform an ideal setting to study the relation of environmental conditions and physico-chemical characteristics of thermal water with the nature of their siliceous sinter deposits.

The El Tatio sinters are mainly constituted by micro- and nano-scale opal-A spheres, and show a very low degree of structural order. FWHM values range from 7.8 to 12.5 and this parameter is increased by the incorporation of cations in the silica structure. This may be enhanced by the high silica precipitation rate due to the effect of (1) cations in the thermal waters, that increase the inter-particle bonding, and (2) low environmental temperature that lead to increased evaporation rates and/or high cooling rates.

Crystalline phases are common in El Tatio sinters, especially halite and gypsum. Calcium and arsenic-rich minerals, some of which are considered an arsenic borate called cahnite, are found filling cavities and constituting laminations within the sinter deposits. Their occurrence in the sinter deposits is possible due to the full evaporation of high-sodium, sulfur, arsenic and boron thermal waters. The occurrence of arsenic borates has been previously reported at El Tatio (García-Valles *et al.* 2008; Rodgers *et al.* 2002b), although their origin in geothermal fields has not been studied.

El Tatio sinters show a relatively high content of sodium, chlorine and calcium, which are linked to the occurrence of halite, gypsum and calcium-arsenic borates. They also show a relatively high content of iron and aluminum. The first is possibly associated with the occurrence of hydrous ferric oxides, as have been reported by Alsina *et al.* (2008, 2013), yet were not observed in this study, while the second is attributed to lithic material blown into the sinter deposit.

Regarding the trace elements, arsenic and boron show the highest content, and are related to cahnite or other arsenic borates such as teruggite and nobleite, reported by García-Valles *et al.* (2008) and Rodgers *et al.* (2002b). The occurrence of these minerals is related to the particular thermal water chemistry of this geothermal field: 125 to >300 mg/l of calcium, 40 to >100 mg/l of boron, and 18 to >30 mg/l of arsenic. The chemical composition of thermal waters plays an important role in the El Tatio sinter chemistry because sinter formation is mainly sub-aerial and driven by evaporation to dryness.

Distinctive macro- and micro-textures identified in the El Tatio sinters are related in some cases to ambient temperatures, while others are linked exclusively to water temperature and hydrodynamics. Silica platelets formation is attributed to freezing-unfreezing events that occur daily at El Tatio, as sub-zero temperature is common at night, while day temperatures usually rises enough to produce unfreezing. Microbial textures are also common in El Tatio sinters, as is in most studied sinters in USA and New Zealand (e.g. Braunstein and Lowe, 2001; Smith *et al.*, 2003; Mountain *et al.*, 2003). Yet, the co-existence of spicular texture with mid-temperature microbial filaments is an interesting finding, because geyserite is related to eruptive near-vent settings which are usually high temperature, where the water temperature is too high to support life, or at least high enough that only high-temperature microbes can tolerate (Cassie, 1989; Cady and Farmer, 1996). Nevertheless, the lower boiling temperature at high altitude would allow the co-existence a boiling-related texture and mid-temperature microbes. Thus, at El Tatio and other high altitude geothermal fields, the interpretation of near-vent settings should be done based on sinter textures. However, infrequent eruptive event would also explain the co-existence of these two characteristics.

These characteristics contrast with those typical of New Zealand and USA sinters, and highlight the importance of understanding the particular mineralogical and textural characteristics of andean sinters to successfully use them in geothermal exploration. The integrative study of siliceous sinter deposits at active geothermal fields, that include mineralogical and textural determinations along with thermal water characterization and experimental silica precipitation rate measurements, provides new insights about the nature of siliceous sinter deposits in the Andean context, and might have great significance for the study of hydrothermal systems on Earth, and for planetary exploration of the Solar System.

REFERENCES

Alpers, C., Whittemore, D. O., 1990. Hydrogeochemistry and stable isotopes of ground and surface waters from two adjacent closed basins, Atacama Desert, northern Chile. Applied Geochemistry 5, 719–734.

Alsina, M.A., Saratovsky, I., Gaillard, J-F., Pastén, P.A., 2007. Arsenic speciation in solid phases of geothermal fields **in** Barnett, M. O. and Kent, D. B. (eds.). Developments in Earth and Environmental Sciences, 7.

Alsina, M. A., Zanella, L., Hoel, C., Pizarro G. E., Gaillard, J-F., Pastén, P.A., 2013. Arsenic speciation in sinter mineralization from a hydrothermal channel of El Tatio geothermal field, Chile. Journal of Hydrology (in press).

Aravena, D., Lahsen, A., 2013. A geotermal favorability map of Chile, preliminary results. Transactions of the Geothermal Resources Council 2013, Nevada, USA (in press).

Arnórsson, S., 2000. Chemical reactions and chemical equilibria **in** Arnórsson, S. Isotopic and chemical techniques in geothermal exploration, development and use: sampling methods, data handling, interpretation. International Atomic Energy Agency. Vienna, 351 p.

Blasdale, W. C., Slansky, C. M., 1939. The solubility curves of boric acid and the borates of sodium. Contribution from the chemical laboratory of the University of California.

Braunstein, D.G., 1999. The role of hydrodynamics in the structuring and growth of high-temperature (>73 °C) siliceous sinter at neutral to alkaline hot springs and geysers, Yellowstone National Park. Ph.D. Thesis, Stanford University, 163 p.

Braunstein, D., Lowe, D.R., 2001. Relationship between spring and geyser activity and the deposition and morphology of high temperature (>73 ◦C) siliceous sinter, Yellowstone National Park, Wyoming, U.S.A. Journal of Sedimentary Research71, 747–763.

Cady, S.L., Farmer, J.D., 1996. Fossilization processes in siliceous thermal springs: trends in preservation along thermal gradients **in** Bock, G.R., Goode, J.A. (eds.), Evolution of Hydrothermal Ecosystems on Earth (and Mars?). Proceedings of the CIBA Foundation Symposium 202. Wiley, Chichester, U.K., 150–173.

Campbell, K.A., Sannazzaro, K., Rodgers, K.A., Herdianita, N.R., Browne, P.R.L., 2001. Sedimentary facies and mineralogy of the Late Pleistocene Umukuri silica sinter, Taupo Volcanic Zone, New Zealand. Journal of Sedimentary Research 71, 727–746.

Campbell, K.A., Buddle, T.F., Browne, P.R.L., 2004. Late Pleistocene silica sinter associated with fluvial, lacustrine, volcaniclastic and landslide deposits at Tahunaatara, Taupo Volcanic Zone, New Zealand. Transactions of the Royal Society of Edinburgh: Earth Sciences 94, 485–501.

Cassie, V. 1989. A taxonomic guide to thermally associated algae (excluding diatoms) in NewZealand. Bibliotheca Phycologica 78, 161–255.

Channing, A., Butler, I.B., 2007. Cryogenic opal-A deposition from Yellowstone hot springs. Earth and Planetary Science Letters 257, 121 – 131.

Coira B., Davidson J., Mpodozis C., Ramos V (1982). Tectonic and magmatic evolution of the Andes of northern Argentina and Chile. Earth-Science Reviews 18, 303-332.

Cusicanqui, H., Mahon, W.A.J., y Ellis, A.J., 1975. The geochemistry of the El Tatio Geothermal Field, northern Chile. Proceedings, Second United Nations Symposium on the Development and Use of Geothermal Resources, San Francisco, 703–711.

DGA data, 2010. Metodología para la estimación de recarga de cuencas altiplánicas y precordilleranas de vertiente pacífica en el norte de Chile, XV, I, II y III Regiones. Ministerio De Obras Públicas, Dirección General de Aguas.

Downs, R.T., Hall-Wallace, M. (2003). The American Mineralogist Crystal Structure Database. American Mineralogist 88, 247-250.

Ellis, A. J. and Mahon, W.A.J., 1977. Chemistry and geothermal systems. Energy Science and Engineering: Resources, Technology, New York, 372 p.

Farmer, J.D. 1996. Hydrothermal systems on Mars: an assessment of present evidence, p. 273-299. In Bock, G.R. and Goode, J.A. (eds.), Evolution of Hydrothermal Ecosystems on Earth (and Mars?), CIBA Foundation Symposium 202. John Wiley and Sons, Chichester.

Farmer, J.D. 2000. Hydrothermal systems: doorways to early biosphere evolution. Geological Society of America Today 10, 2-9.

Fournier, R.O., Rowe, J.J., 1966. Estimation of underground temperatures from the silica content of water from hot springs and steam wells. American Journal of Science 264, 685– 697.

Fournier, R.O., Kennedy, B.M., Aoki, M., Thompson, J.M., 1994.Correlation of gold in siliceous sinters with $^3He/^4He$ in hot spring waters of Yellowstone National Park. Geochimica et Cosmochimica Acta 58, 5401–5419.

Franks, M. A., 2012. Archaea at the El Tatio Geyser Field: community composition, diversity, and distribution across hydrothermal features and geochemical gradients. Ph. D. Thesis. University of Texas, 183p. U. S. A.

García-Valles, M., Fernández-Turiel, J.L., Gimeno-Torrente, D., Saavedra-Alonso, J., Martínez-Manent, S., 2008. Mineralogical characterization of silica sinters from the El Tatio geothermal field, Chile. American Mineralogist 93, 1373–1383.

Giggenbach, W.F., Gouguel, R.L., 1989. Collection and analysis of geothermal and volcanic water and gas discharges, Department of Scientific and Industrial Research, Chemistry Division, Petone, New Zealand, 172 p.

Guido, D.M., de Barrio, R.E., Schalamuk, I.B., 2002. La Marciana Jurassic sinter: implications for exploration for epithermal precious-metal deposits in Deseado Massif, southern Patagonia, Argentina. Institution of Mining and Metallurgy Transactions Section B: Applied Earth Science 111, 106–113.

Guidry, S.A., Chafetz, H.S., 2003a. Anatomy of siliceous hot-springs: examples from Yellowstone National Park, Wyoming, U.S.A. Sedimentary Geology 157, 71–106.

Guidry, S.A., Chafetz, H.S., 2003b. Depositional facies and diagenetic alteration in a relict siliceous hot spring accumulation: examples from Yellowstone National Park, U.S.A. Journal of Sedimentary Research 73, 806–823.

Guidry, S.A., Chafetz, H.S., 2003c. Siliceous shrubs in hot springs from Yellowstone National Park, Wyoming, U.S.A. Canadian Journal of Earth Sciences 40, 1571–1583.

Hampton, W. A., White, G. P., Hoskin, P. W. O., Browne, P. R. L., Rodgers, K. A., 2004. Cinnabar, livingstonite, stibnite and pyrite in Pliocene silica sinter from Northland, New Zealand. Mineralogical Magazine 68, 191–198

Handley, K. M., Campbell, K. A., Mountain, B. W., Browne, P. R. L., 2005. Abiotic–biotic controls on the origin and development of spicular sinter: in situ growth experiments, Champagne Pool, Waiotapu, New Zealand. Geobiology 3, 93–114.

Handley, K.M., Campbell, K.A. 2011.Character, analysis and preservation of biogenecity in terrestrial siliceous stromatolites from geothermal settings **in** Tewari,V.C., Seckbach, J. (eds.), Stromatolites: Interaction of Microbes with Sediments, Cellular Origin, Life in Extreme Habitats and Astrobiology 18, 359–381

Hauser, A., 1997. Catastro y caracterización de las fuentes de aguas minerales y termales de Chile. SERNAGEOMIN, Boletín 50, 90 p, Santiago, Chile.

Helvaci, C., Alonso, R. N., 2000. Borate Deposits of Turkey and Argentina; A Summary and Geological Comparison. Turkish Journal of Earth Sciences 9, 1-27.

Herdianita, N.R., Browne, P.R.L., Rodgers, K.A., Campbell, K.A., 2000. Mineralogical and textural changes accompanying ageing of silica sinter. Mineralium Deposita 35, 48–62.

Hinman, N. and Lindstrom, R.F., 1996. Seasonal changes in silica deposition in hot spring systems. Chemical Geology 132, 237–246.

Hunter, R.J., 1993.Introduction to Modern Colloid Science. Oxford University Press, New York, 338 p.

Huttrer, G. W., 1995. The status of world Geothermal Power production 1990-1994. Proceedings World Geothermal Congress, Florence, Italy, 1995, 1, 3-13.

Iler, R. K., 1979. The chemistry of silica: solubility, polimerization, colloid and surface properties and biochemistry. Wiley, New York, 866 p.

Jones, B., Renaut, R.W., 2003. Hot spring and geyser sinters: the integrated product of precipitation, replacement and deposition. Canadian Journal of Earth Science 40, 1549-1569

Jones, B., Renaut, R.W., Rosen, M.R., 1997. Biogenicity of silica precipitation around geysers and hot-spring vents, North Island, New Zealand. Journal of Sedimentary Research 67, 88–104.

Jones B, Renaut RW, Rosen MR.,2000. Stromatolites forming in acidic hot-spring waters, North Island, New Zealand.Palaios15, 450–75.

Jones, B., Renaut, R.W., Rosen, M.R., 2001. Microbial construction of siliceous stalactites at geysers and hot springs: examples from the Whakarewarewa Geothermal Area, North Island, New Zealand. Palaios 16, 73–94.

Jones, B., Renaut, R.W., Rosen, M.R., Ansdell, K.M, 2002. Coniform stromatolites from geothermal systems, North Island, New Zealand. Palaios 17, 84–103.

Jones, B., Renaut, R.W., Rosen, M.R., 2003. Silicified microbes in a geyser mound: the enigma of low-temperature cyanobacteria in a high-temperature setting. Palaios 18, 87–109.

Konhauser, K.O. and Ferris, F.G.,1996. Diversity of iron and silica precipitation by microbial mats in hydrothermal waters, Iceland: implications for Precambrian iron formations. Geology 24, 323–326.

Konhauser, K.O., Phoenix, V.R., Bottrell, S.H, Adams, D.G., Head, I.M., 2001. Microbial-silica interactions in Icelandic hot spring sinter: possible analogues for some Precambrian siliceous stromatolites. Sedimentology 48, 415–433.

Konhauser, K. O., Jones, B., Reysenbach, A., Renaut, R.W., 2003. Hot spring sinters: keys to understanding Earth's earliest life forms. Canadian Journal of Earth Science 40, 1713-1724

Kraft, M.D., Michalski, J.R., Sharp, T.G., 2003. Effects of pure silica coatings on thermal emission spectra of basaltic rocks: considerations for martian surface mineralogy. Geophysical Research Letters 30, 1944-8007.

Krauskopf, K. B., 1956. Dissolution and precipitation of silica at low temperatures: Geochimica et Cosmochimica Acta 10, 1–26.

Lahsen, A., 1976. Geothermal exploration in Northern Chile - Summary. Circum-Pacific Energy and Mineral Resources. American Association of Petroleum Geologists 25, 169-175.

Lahsen, A., 1986. Origen y potencial de energía geotérmica en los Andes de Chile, **in** Frutos, J., Oyarzún, R., Pincheira, M. (eds.), Geología y Recursos Minerales de Chile. Universidad de Concepción, Chile, 923 p.

Lahsen, A., 1988. Chilean Geothermal Resources and their possible utilization. Geothermics 17, 401-410.

Landrum, J.T.; Bennett, P.C.; Engel, A.S.; Alsina, M.A.; Pastén, P.A.; Milliken,K., 2009. Partitioning geochemistry of arsenic and antimony, El Tatio Geyser Field, Chile. Applied Geochemistry24, 664-676.

Lowe, D.R., Anderson, K.S., Braunstein, D., 2001. The zonation and structuring of siliceous sinter around hot springs, Yellowstone National Park, and the role of thermophilic bacteria in its deposition, **in** Reyesenbach, A.-L., Voytek M., Mancinelli, R. (eds.), Thermophiles: Biodiversity, Ecology, and Evolution. Kluwer Academic/Plenum Publishers, New York, 143–166.

Lowe, D.R., Braunstein, D., 2003. Microstructure of high-temperature (>73 °C)siliceous sinter deposited around hot springs and geysers Yellowstone National Park: the role of biological and abiological processes in sedimentation. Canadian Journal of Earth Sciences 40, 1611–1642.

Lynne, B.Y., Campbell, K.A., 2003. Diagenetic transformations (opal-A to quartz) of low- and mid-temperature microbial textures in siliceous hot-spring deposits, Taupo Volcanic Zone, New Zealand. Canadian Journal of Earth Sciences 40, 1679–1696.

Lynne, B.Y., Campbell, K.A., 2004. Morphologic and mineralogic transitions from opal-A to opal-CT in low-temperature siliceous sinter diagenesis, Taupo Volcanic Zone, New Zealand. Journal of Sedimentary Research 74, 561–579.

Lynne, B.Y., Campbell, K.A., Moore, J.N., Browne, P.R.L., 2005. Diagenesis of 1900-year-old siliceous sinter (opal-A to quartz) at Opal Mound, Roosevelt Hot Springs, Utah, U.S.A. Sedimentary Geology 179, 249-278.

Lynne, B.Y., Campbell, K.A., Perry, R.S., Moore, J, Browne, P.R.L., 2006. Acceleration of sinter diagenesis in an active fumarole, Taupo Volcanic Zone, New Zealand. Geology 34, 749–752.

Lynne, B.Y., 2007. Diagenesis of Siliceous Sinter Deposits in the U.S.A. and New Zealand. PhD Thesis. University of Auckland, 189p., New Zealand.

Lynne, B.Y., Campbell, K.A., James, B., Browne, P.R.L., Moore, J.N., 2007. Tracking crystallinity in siliceous hot-spring deposits. American Journal of Science 307, 612–641

Lynne, B.Y., Campbell, K.A., Moore, J.N., Browne, P.R.L., 2008. Origin and evolution of the Steamboat Springs siliceous sinter deposit, Nevada, U.S.A. Sedimentary Geology 210, 111–131.

Lynne, B.Y., 2012. Mapping vent to distal-apron hot spring paleo-flow pathways using siliceous sinter architecture. Geothermics 43, 3–24.

Makrides, A.C., Turner, M., Slaughter, J., 1980. Condensation of silica from supersaturated silicic acid solutions. Journal of Colloid and Interface Sciences 73, 345–367.

McCollom, T.M., Hynek, B.M. 2005. A volcanic environment for bedrock diagenesis at Meridiani Planumon Mars. Nature 438, 1129-1131.

McKenzie E. J., Brown K. L, Cady S. L., CampbellK. A., 2001. Trace metal chemistry and silicification of microorganisms in geothermal sinter, Taupo Volcanic Zone, New Zealand. Geothermics 30, 483-502.

Michalski, J.R., Kraft, M.D., Sharp, T.G., Williams, L.B., Christensen, P.R., 2005 Mineralogical constraints on the high silica martian surface component observed by TES. Icarus174,161–177.

Mountain, B.W., Benning, L.G., Boerema, J., 2003. Experimental studies on New Zealand hot spring sinters: Rates of growth and textural development. Canadian Journal of Earth Sciences 40, 1643–1667.

Nicholson, K., 1988. Geothermal deposits in ancient terrain as a tool in epithermal gold exploration: Examples from Scotland. Proceedings 10th New Zealand Geothermal Workshop, 1988.

Nicholson, K., and Parker,R. J., 1990.Geothermal sinter towards a diagnostic signature and a sinter geothermometer. Procceedings 12th New Zealand Geothermal workshop, 97-102.

Piper, A. M. 1957. A graphic procedure in the geochemical interpretation of water analysis. United States Geological Service. Ground Water Note 12.

Pirajno, F., 2010. Porphyry systems; fossil and active epithermal systems. In: Hydrothermal processes and mineral systems. Geological Survey of Western Australia, Perth, Australia, 422-485 p.

Petrucci, R. H., Harwood, W S., Herring, G., 2002. General Chemistry: Principles and Modern Applications. 1160p.

Pope, J. G., McConchie, D. M., Clark, M. D., Brown, K. L., 2004.Diurnal variations in the chemistry of geothermal fluids after discharge, Champagne Pool, Waiotapu, New Zealand. Chemical Geology 203, 253-272.

Preston, L. J., Genge, M. J., 2010. The Rhynie Chert, Scotland, and the search for life on Mars. Astrobiology 10, 549–560.

Renaut, R.W., Jones, B., Rosen, M.R., 1996. Primary silica oncoids from Orakeikorako hot springs, North Island, New Zealand. Palaios 11, 446–458.

Rimstidt, J.D., Cole, D.R., 1983. Geothermal mineralization I: the mechanism of formation of the Beowawe, Nevada, siliceous sinter deposit. American Journal of Science 283, 861–875.

Rodgers, K. A., Cook,K. L., Browne, P. R. L., Campbell, K. A. 2002. The mineralogy, texture and significance of silica derived from alteration by steam condensate in three New Zealand geothermal fields. Clay Minerals 37, 299–322

Rodgers, K.A., Greatrex, R., Hyland, M., Simmons, S.F., Browne, P.R.L. 2002b.A modern, evaporitic occurrence of teruggite $Ca_4MgB_{12}As_2O_{28}.18H_2O$, and nobleite, $CaB_6O_{10}.4H_2O$, from the El Tatio geothermal field, Antofagasta Province, Chile. Mineralogical Magazine 66, 253–259.

Rodgers, K.A., Browne, P.R.L., Buddle, T.F., Cook, K.L., Greatrex, R.A., Hampton, W.A., Herdianita, N.R., Holland, G.R., Lynne, B.Y., Martin, R., Newton, Z., Pastars, D.,

Sannazarro, K.L., and Teece, C.I.A., 2004. Silica phases in sinters and residues from geothermal fields of New Zealand. Earth Science Reviews 66, 1-61.

Schinteie, R., Campbell, K.A, Browne, P.R.L, 2007. Microfacies of stromatolitic sinter from acid-sulphate-chloride springs at parariki stream, Rotokawa Geothermal Field, New Zealand. Palaeontologia Electronica 10, 33p

Smith, B.Y., Turner, S.J., Rodgers, K.A., 2003. Opal-A and associated microbes from Wairakei, New Zealand: the first 300 days. Mineralogical Magazine 67,563–579.

Squyres, S.W., Arvidson, R.E., Ruff, S., Gellert, R., Morris, R.V.,Ming, D.W., Crumpler, L., Farmer, J.D., Marais, D.J., Des Yen,A., McLennan, S.M., Calvin, W., Bell, J.F., III, Clark, B.C.,Wang, A., McCoy, T.J., Schmidt, M.E., and de Souza, P.A., Jr., 2008.Detection of silica-rich deposits on Mars. Science 320, 1063–1067.

Tobler, D.J., Stefansson, A., Benning, L.G., 2008. In situ grown silica sinters in Icelandic geothermal areas. Geobiology 6, 481-502.

Walter, M.R., 1976. Hot-springs sediments in Yellowstone National Park. In: Walter, M.R. (ed.), Stromatolites: Amsterdam. Elsevier, Developments in Sedimentology, 489–498.

Walter, M.R., Des Marais, D., Farmer, J.D., Hinman, N.W., 1996. Lithofacies and biofacies of mid-Paleozoic thermal spring deposits in the Drummond basin, Queensland, Australia. Palaios 11, 497–518.

White D. E, Brannock, W. W. Murata, K. J.,1956.Silica in hot-spring waters.Geochimica et Cosmochimica Acta 10, 27-59.

White, D.E., 1992. The Beowawe Geysers, Nevada, before geothermal development.U.S. Geological Survey Bulletin 1998, 1 –19.

Yokoyama T., Sato Y., Maeda, Y., Tarutani, T., Itoi, R., 1993. Siliceous deposits formed at geothermal water I. the major constituents and existing states of iron and aluminium. Geochemical Journal 27, 375-384.

Yokoyama, T., Taguchi, S., Motomura, Y., Watanabe, K., Nakanishi, T., Aramaki, Y., Izawa, E., 2004.The effect of aluminum on the biodeposition of silica in hot spring water: Chemical state of aluminum in siliceous deposits collected along the hot spring water stream of Steep Cone hot spring in Yellowstone National Park, USA. Chemical Geology 212, 329-337.

Zhou, J., and Lau, K.M., 1998. Does a monsoon climate exist over South America? Journal of Climate 11, 1020-1040.

APPENDICES

APPENDIX I: Chemistry of El Tatio sinter samples

Table I.1. El Tatio sinters chemistry: main elements. DL=detection limit

	Unit	DL	M2.1	M2.3	M3B	M3R	M3.2	M4.2	M5	M6.4
Cl	%	0.01	1.54	2.67	0.2	0.71	0.48	0.47	0.56	0.14
Total S	%	0.01	0.11	0.06	0.07	0.08	0.13	0.04	0.02	0.05
SiO_2	%	0.01	64.15	59.58	41.08	8.1	70.09	73.25	85.04	77.63
Al_2O_3	%	0.01	0.62	5.85	0.76	0.81	3.86	0.97	0.67	1.98
$Fe_2O_{3(T)}$	%	0.01	0.87	2.88	3.16	18.75	1.53	0.44	0.23	1.73
MnO	%	0.001	0.235	0.146	1.093	0.811	0.184	0.013	0.006	0.043
MgO	%	0.01	0.22	0.79	1.64	0.24	0.63	0.08	0.06	0.27
CaO	%	0.01	3.46	2.83	7.26	8.59	3.72	0.38	0.56	2.07
Na_2O	%	0.01	2.17	3.36	0.55	0.7	1.6	0.72	0.96	0.79
K_2O	%	0.01	0.54	1.12	0.31	0.49	0.91	0.5	0.43	0.39
TiO_2	%	0.001	0.042	0.335	0.036	0.06	0.186	0.034	0.025	0.089
P_2O_5	%	0.01	0.04	0.07	0.04	0.02	0.04	0.02	0.01	0.01
Total	%	0.01	72.35	76.97	55.93	38.57	82.75	76.4	87.99	85.01

Table I.2. El Tatio sinter samples chemistry: minor and trace elements. DL=detection limit

	Unit	DL	M2.1	M2.3	M3B	M3R	M3.2	M4.2	M5	M6.4
Sc	ppm	1	< 1	5	< 1	1	3	< 1	< 1	2
Be	ppm	1	14	8	51	268	4	21	7	37
V	ppm	5	13	77	14	21	37	16	16	22
Cr	ppm	20	< 20	20	< 20	< 20	< 20	< 20	< 20	< 20
Co	ppm	1	1	5	6	8	3	< 1	< 1	1
Ni	ppm	20	< 20	< 20	< 20	< 20	< 20	< 20	< 20	< 20
Cu	ppm	10	50	110	90	50	220	20	30	< 10
Zn	ppm	30	40	80	140	410	50	< 30	< 30	< 30
Ga	ppm	1	5	12	6	8	6	238	92	54
Ge	ppm	1	9	5	20	13	6	3	8	6
As	ppm	5	>2000	315	>2000	>2000	694	177	334	>2000
Rb	ppm	2	94	112	63	48	110	121	71	67
Sr	ppm	2	328	265	521	910	295	43	41	181
Y	ppm	2	< 2	8	12	151	5	< 2	< 2	< 2
Zr	ppm	4	19	94	8	28	48	7	6	23
Nb	ppm	1	5	6	4	5	4	3	3	3
Mo	ppm	2	< 2	3	3	2	6	< 2	< 2	< 2
Ag	ppm	0.5	0.6	1.2	< 0.5	0.6	2.4	0.8	0.6	< 0.5
In	ppm	0.2	<0.2	<0.2	< 0.2	< 0.2	<0.2	<0.2	<0.2	< 0.2
Sn	ppm	1	< 1	1	< 1	< 1	5	< 1	< 1	< 1
Sb	ppm	0.5	> 200	>200	> 200	> 200	>200	>200	>200	> 200

Continue Table I.2. El Tatio sinter samples chemistry: minor and trace elements. DL=detection limit

	Unit	DL	M2.1	M2.3	M3B	M3R	M3.2	M4.2	M5	M6.4
Cs	ppm	0.5	754	602	553	77.4	909	926	514	881
Ba	ppm	3	103	241	197	360	209	27	17	64
La	ppm	0.1	1.7	13.5	3.8	29.6	8.4	1.7	1.3	3.6
Ce	ppm	0.1	3.4	27.6	7.4	56.6	16.9	3.3	2.4	7.3
Pr	ppm	0.05	0.41	3	0.86	7.61	1.79	0.35	0.25	0.78
Nd	ppm	0.1	1.3	11.2	3.9	38.7	6.9	1.3	0.9	3
Sm	ppm	0.1	0.3	2.2	1.1	13	1.3	0.2	0.2	0.6
Eu	ppm	0.05	0.06	0.49	0.18	2.17	0.3	0.06	<0.05	0.1
Gd	ppm	0.1	0.3	1.8	1.5	20.7	1.2	0.2	0.2	0.5
Tb	ppm	0.1	< 0.1	0.3	0.3	4	0.2	< 0.1	< 0.1	< 0.1
Dy	ppm	0.1	0.3	1.5	1.8	25.8	1	0.2	0.1	0.4
Ho	ppm	0.1	< 0.1	0.3	0.4	5.2	0.2	< 0.1	< 0.1	< 0.1
Er	ppm	0.1	0.2	0.8	1	14.8	0.5	0.1	< 0.1	0.2
Tm	ppm	0.05	< 0.05	0.12	0.13	2.13	0.07	<0.05	<0.05	< 0.05
Yb	ppm	0.1	0.1	0.8	0.8	12.8	0.5	< 0.1	< 0.1	0.2
Lu	ppm	0.04	< 0.04	0.15	0.11	1.82	0.08	<0.04	<0.04	< 0.04
Hf	ppm	0.2	0.4	2.6	0.3	1	1.3	< 0.2	< 0.2	0.5
Ta	ppm	0.1	0.3	0.5	0.2	0.1	0.3	0.2	0.2	0.2
W	ppm	1	4	4	6	51	4	5	12	9
Tl	ppm	0.1	1.6	1.2	5.8	12.8	5	2.3	1	1.3
Pb	ppm	5	< 5	12	10	56	9	5	< 5	9
Bi	ppm	0.4	< 0.4	< 0.4	0.6	< 0.4	< 0.4	< 0.4	< 0.4	< 0.4
Th	ppm	0.1	1.3	6	0.8	0.8	3	0.7	0.5	1.4
U	ppm	0.1	0.3	2	0.3	0.5	1	0.4	0.4	0.9
Li	ppm	1	140	199	133	52	78	66	55	37

APPENDIX II. Available published data on sinter geochemistry.

The following data correspond to the geochemistry of various siliceous sinter deposits around the world, which is given as a comparison to the compositions of the El Tatio siliceous sinter deposits.

Table II.1. Selected New Zealand sinters elemental chemistry from Nicholson and Parker (1990).

sample ID	SiO_2 wt%	TiO_2 wt%	Al_2O_3 wt%	Fe_2O_3 wt%	MnO wt%	MgO wt%	CaO wt%	Na_2O wt%	K_2O wt%	P_2O_5 wt%
A4	89.16	0.01	0.53	0.55	<0.01	0.11	0.11	0.46	0.01	<0.01
A5	88.82	0.01	1.14	0.14	0.02	0.08	0.11	0.23	0.08	<0.01
CP1	60.27	0.04	0.26	0.18	<0.01	0.10	0.04	0.12	0.13	<0.01
CP3	63.19	0.04	1.42	0.34	0.01	0.06	0.04	0.07	0.14	<0.01
CP4	80.85	0.05	1.91	0.39	0.01	0.08	0.06	0.12	0.24	0.01
CPE	79.60	0.06	2.00	0.11	0.02	0.10	0.06	0.12	0.31	0.01
CPD	78.69	0.06	1.97	0.30	0.02	0.08	0.06	0.09	0.28	<0.01
OP2	43.75	0.02	0.41	0.14	0.26	0.75	28.08	0.34	0.09	0.01
OP4	90.06	0.06	2.52	0.55	<0.01	0.10	0.33	0.80	0.61	0.01
T1	91.87	0.03	1.00	0.34	0.01	0.12	0.12	0.27	0.16	0.01
T12	87.18	0.04	1.18	0.39	0.01	0.11	0.21	0.57	0.14	0.01
T13	93.12	0.07	1.94	0.71	0.01	0.26	0.40	0.72	0.43	<0.01
T77/1	89.42	0.02	0.60	0.30	0.04	0.06	0.09	0.21	0.08	0.01
T103/1	92.96	0.04	1.36	0.46	<0.01	0.09	0.09	0.11	0.25	<0.01
T105/1	92.58	0.02	0.67	0.31	<0.01	0.04	0.10	0.29	0.15	0.01

A=Atiamuri; CP=Champagne Pool; OP=Ohaaki Pool; T=Tokaanu Springs

Table II.2. Selected New Zealand sinters trace elements chemistry from Nicholson and Parker (1990).

sample ID	As ppm	Ba ppm	Cr ppm	Cu ppm	La ppm	Nb ppm	Ni ppm	Pb ppm	Rb ppm	Sr ppm	Th ppm	V ppm	Y ppm	Zn ppm	Zr ppm
A4	<1	12	10	23	22	2	<1	11	14	7	5	<1	1	5	3
A5	<1	39	6	<1	22	1	<1	8	12	9	3	5	4	6	9
CP1	147	17	17	<1	3	1	<1	11	5	5	<1	<1	1	<1	7
CP3	214	19	26	<1	3	<1	5	6	3	5	<1	6	2	<1	7
CP4	128	51	8	<1	4	1	<1	7	10	11	<1	51	3	<1	15
CPE	115	51	8	3	3	2	2	6	11	9	2	51	3	<1	15
CPD	134	50	12	<1	3	2	<1	5	10	11	<1	4	4	<1	21
OP2	246	30	<1	<1	10	1	5	4	16	684	<1	<1	<1	5	12
OP4	5	91	10	10	8	2	<1	12	47	34	5	5	5	16	33
T1	49	13	12	<1	17	<1	<1	12	30	28	5	10	<1	3	7
T12	60	13	13	<1	15	2	<1	6	16	64	<1	10	<1	3	8
T13	76	12	10	5	48	<1	<1	18	86	118	<1	16	<1	18	16
T77/1	33	<1	11	<1	13	1	<1	6	12	25	<1	<1	<1	<1	4
T103/1	26	20	12	<1	19	2	<1	7	39	34	<1	9	2	<1	8
T105/1	55	15	9	<1	14	1	<1	6	23	28	<1	<1	<1	<1	3

A=Atiamuri; CP=Champagne Pool; OP=Ohaaki Pool; T=Tokaanu Springs

Table II.3. Taupo Volcanic Zone sinters (New Zealand) chemistry from Mckenzie *et al.* (2001).

sample ID	SiO$_2$ wt%	Fe$_2$O$_3$ wt%	MnO wt%	CaO wt%	SO$_3$ ppm	As ppm	Sb ppm
TK1	70.60	8.85	2.63	2.35	349	1646	349
TK2	88.10	0.82	0.05	0.41	56	80	160
TK3	85.70	0.40	0.05	0.52	2070	143	494
OHK	88.10	0.08	0.00	0.26	1100	18	245
WKFP11	82.60	0.10	0.01	0.48	194	bd	157
WKB116	81.20	0.21	0.01	0.63	151	bd	211
WKMD	86.40	0.74	0.03	0.30	617	938	bd
WKEB	89.00	0.25	0.02	0.51	284	13	160
WKT	39.30	0.28	0.30	36.40	751	99	bd

TK=Tokaanu; OH=Ohaaki; WK=Wairakei; WKT= Waikite

Table II.4. Steep Cone Sinter (USA) chemistry from Yokoyama *et al.* (2004).

sample ID	SiO$_2$ wt%	Al$_2$O$_3$ wt%	Fe$_2$O$_3$ wt%	CaO wt%	Na$_2$O wt%	K$_2$O wt%
YNP1	71.86	6.27	0.21	0.42	2.6	0.93
YNP2	83.45	3.16	0.07	0.15	1.42	0.51
YNP3	92.88	0.99	0.03	0.05	0.52	0.16
YNP4	92.94	0.18	0.01	0.08	0.56	0.1
YNP5	90.37	0.28	0.03	0.09	0.89	0.16
YNP6	93.58	0.18	0.02	0.08	0.68	0.12

Table II.4. Kyushu sinters (Japan) chemistry from Yokoyama *et al.* (1993).

sample ID	SiO$_2$ wt%	Al$_2$O$_3$ wt%	Fe$_2$O$_3$ wt%	MgO wt%	CaO wt%	Na$_2$O wt%	K$_2$O wt%
H-1	91.79	1	0.61	0.086	0.10	0.36	0.25
H-2	60.42	0.59	29.70	0.33	1.61	0.83	0.21
H-3	77.98	4.57	6.47	0.42	0.68	0.78	0.91
H-4	40.06	5.55	46.03	0.095	0.17	0.96	0.51
H-5	89.45	0.53	0.48	0.019	0.06	0.19	0.073
O-1	73.51	7.95	1.48	0.14	1.83	1.7	0.29
O-2	86.27	3.01	0.85	0.47	0.65	0.64	0.52
O-3	63.05	7.91	9.00	0.16	0.84	1.73	1.16
O-4	70.73	8.42	0.10	0.033	1.75	1.17	0.31
T-1	65.67	10	0.44	0.13	3.30	1.09	1.15
M-1	76.60	7.87	0.10	0.073	1.12	1.36	0.032
F-1	74.26	2.52	2.37	4.78	1.37	1.11	0.7
F-2	80.27	2.89	4.50	0.53	0.70	1.63	0.67
F-3	90.08	0.44	0.76	0.063	0.45	0.58	0.23
F-4	86.45	0.88	4.95	0.13	0.44	0.71	0.41

H=Hachobaru; O=Ohtake; T=Takigami; M=Makizono; F=Fushime

Additional information, regarding Kyushu sinter samples coloration is reported in Yokoyama et al., 1993. Sinter samples can be divided into four types as follows. Type I: white-gray (H-1, H-S and F-3); type II: black (H-2, H-4and F-4); type III: (H-3, O-3, F-1 and F-2); type IV (O-1, O-2, O-4, T-1 and M-1)

Table II.5. El Tatio (Chile) sinters chemistry from Landrum *et al.* (2009).

sample ID	Al_2O_3	MnO	CaO	Na_2O	B	As	Sb	Cu	Sr	V
	wt%	wt%	wt%	wt%	ppm	ppm	ppm	ppm	ppm	ppm
ETGF-O	0.34	0.06	0.52	0.93	929.66	1003.93	2398.67	27.96	64.84	10.19
ETGF-W	0.85	0.01	1.63	2.80	2897.08	2000.36	7293.42	36.22	143.70	28.02
ETGF-R	1.20	0.52	2.20	0.84	1102.62	20528.08	3494.51	10.80	231.32	50.94
ETGF-T	0.15	0.01	0.28	0.39	999.93	420.30	5503.55	68.00	315.43	37.19

Table II.6. Yellowstone National Park (USA) sinters chemistry from Fournier *et al.* (1994).

sample ID	Fe2O3	As	Sb	Cu	Pb	Zn	Ag	Hg	Au
	wt%	ppm	ppm	ppm	ppm	ppm	ppm	ppm	ppm
YF01	0.57	3	1.6	3	2	10	<0.2	6.1	6
YF03	0.29	6	6	5	2	3	<0.2	0.25	10
YF02	0.29	11	3.4	6	2	2	<0.2	57	19
YF13	1.00	7	5.6	5	6	29	<0.2	90	6
YF14	0.29	20	5.4	2	<1	3	0.8	4.5	160
YF15	0.29	120	8.2	3	1	2	<0.2	0.14	2
YF16	0.29	9	2.8	4	1	4	<0.2	0.16	3
YF17	0.14	12	4	2	<1	1	<0.2	5.5	4
YF07	1.14	60	150	4	2	6	<0.2	34	1615
YF08	0.14	11	13.4	2	<1	<1	0.7	1.5	40
YF09	1.14	750	51	3	8	27	<0.2	3	18
YF12	0.14	5	2.6	2	1	1	<0.2	1.4	12
YF12y	0.14	640	9.6	1	8	<1	<0.2	4	9
YF18	0.14	1	1.2	2	<1	<1	<0.2	0.11	8
YF18b	0.14	1	1.2	1	1	<1	<0.2	0.34	6
YF18w	0.14	4	5.4	1	<1	<1	<0.2	0.27	38
YF19	4.00	1120	24	1	2	44	<0.2	0.06	13
YF21w	0.86	24	47	4	4	2	<0.2	2.7	3
YF21y		890	18			<1	<0.2		27
YF22	2.86	2	1.4	1	2	<1	<0.2	4.7	8

Red values correspond to hot spring deposits that show a SiO_2 content lower than 50%, which is due that the deposit correspond to a sinter-travertine or a sinter with extremely high iron content. In all cases, the values were not used for average, minimum and maximum elemental concentrations of Table 1.

APPENDIX III: Petrography of El Tatio sinter samples

Sample M2.1

The sample is composed by thin (<0.1 mm) near horizontal laminations, which show light to dark brown coloration under transmitted light. Laminations follow topographic surfaces. Sinter deposit is built over a crystal-rich tuff boulder. Incipient columns are also observed (Figure III.1.)
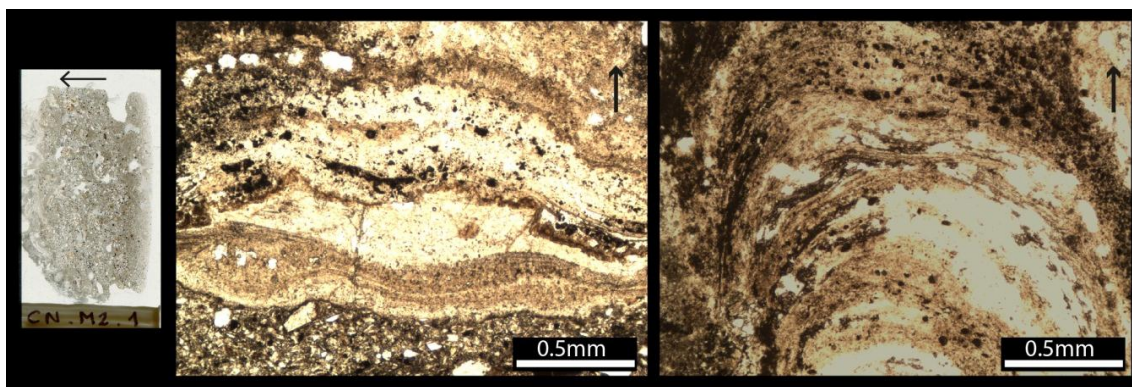

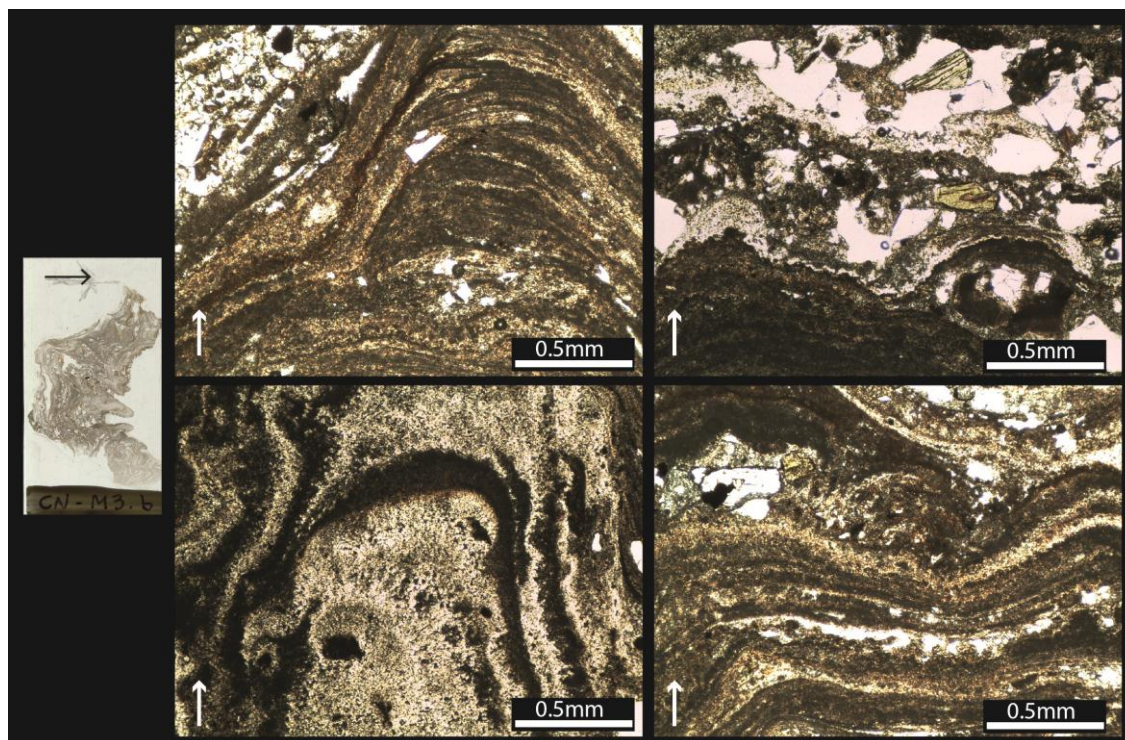Figure III.1. Photomicrographs of sample M2.1 thin section under transmitted light. The arrows indicate the upwards direction.

Sample M3B

Figure III.2. Photomicrographs of sample M3B thin section under transmitted light. The arrows indicate the upwards direction.

The sample is composed by thin (<0.1mm) laminations, which are light to dark brown colored. Laminations are discontinuous and commonly form millimetric columns (Figure III.2). Amphibole and quartz crystal fragments are common and usually accumulate in concavities formed by bumpy laminations.

Sample M3.2

The sample is composed by thin (<0.1 mm) light to dark brown laminations, which are colored. Laminations are usually discontinuous and form columns (Figure III.3). Crystal fragments are common as well as void spaces (porosity).
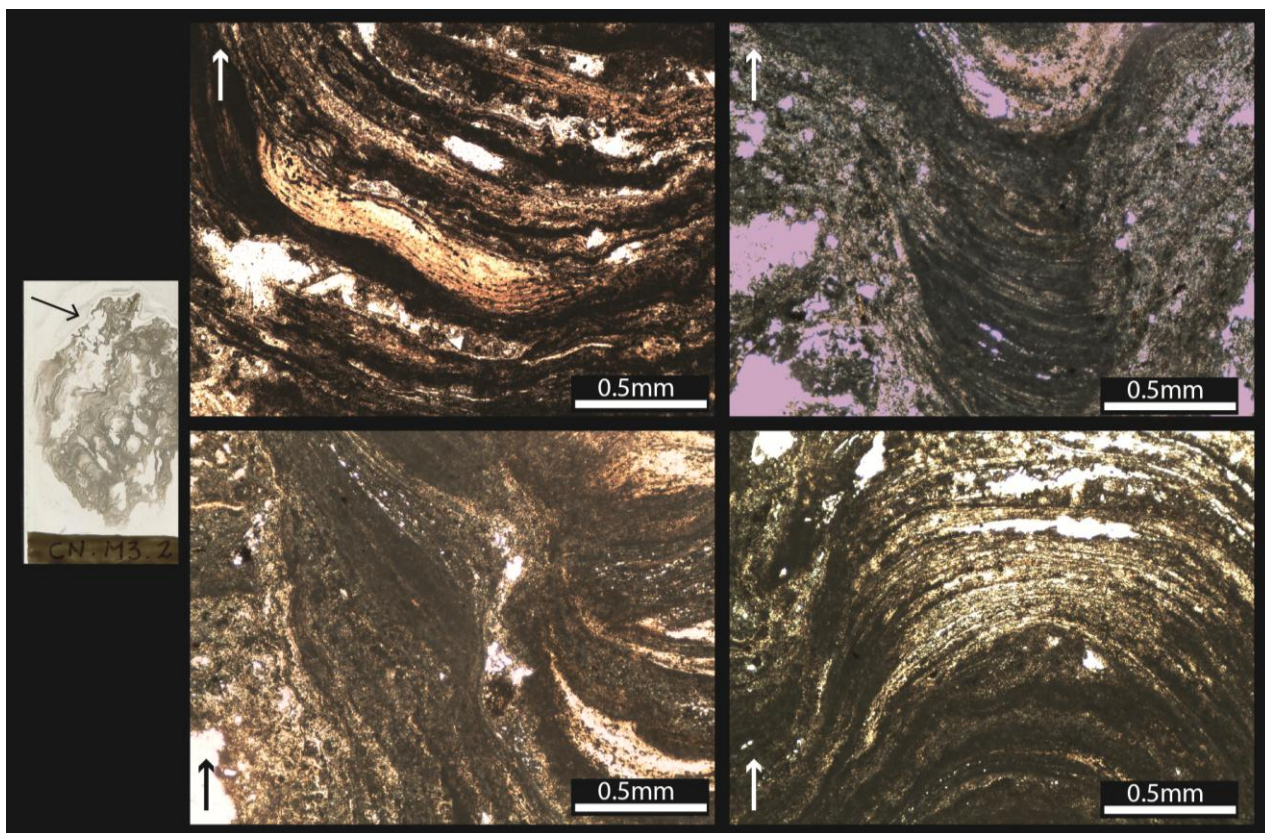

Figure III.3. Photomicrographs of sample M3B thin section under transmitted light. The arrows indicate the upwards direction.

Sample M4.1

The sample is composed by thin (<0.1mm) near horizontal laminations, which show light to dark brown coloration. Sinter laminations grade from base to top to a massive porous deposit that incorporate crystal fragments (Figure III.4)
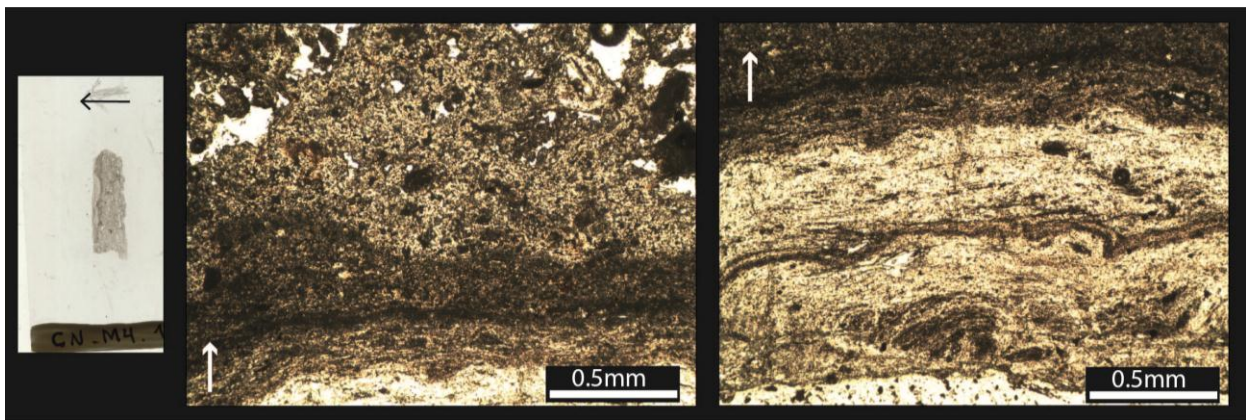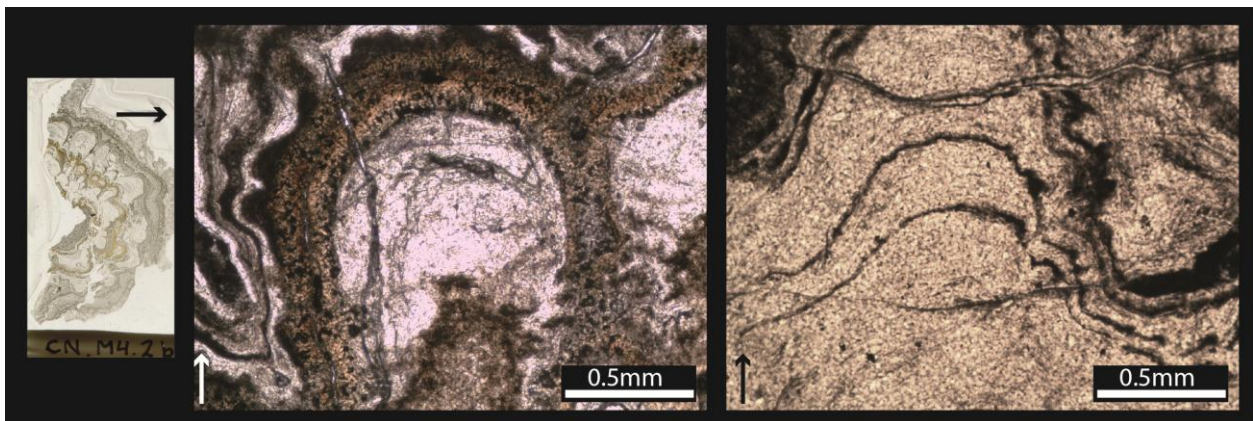
Figure III.4. Photomicrographs of sample M3B thin section under transmitted light. The arrows indicate the upwards direction.

Sample M4.2

The sample is composed by three generations of millimetric columns that are separated by near horizontal laminations (Figure III.5). Individual laminations are <0.1mm width and are light to dark brown colored.

Figure III.5. Photomicrographs of sample M3B thin section under transmitted light. The arrows indicate the upwards direction.

Sample M5

The sample is composed by thin (<0.1-0.2 mm) laminations, which are light to dark brown colored. Laminations are recognizable in the poolwards direction (Figure III.6) and in the upwards direction (Figure III.7) Rhythmic cycles of dark brown thin massive continuous laminations followed by light brown wider laminations are observed in the poolwards direction. Laminations in the upwards direction are wavy and discontinuous. Crystal fragments are also incorporated in the sinter deposit.
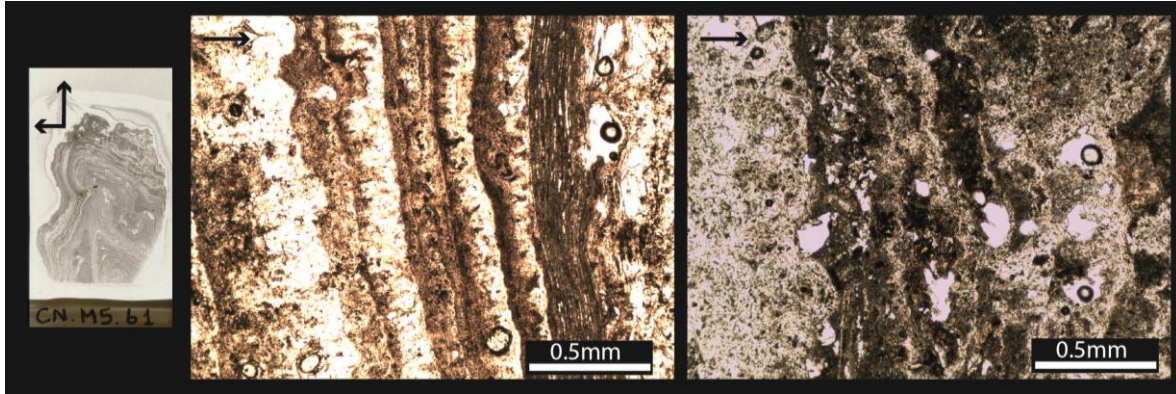
Figure III.6. Photomicrographs of sample M3B thin section under transmitted light. The thin section is approximately horizontal and the black arrows indicate the poolwards direction.
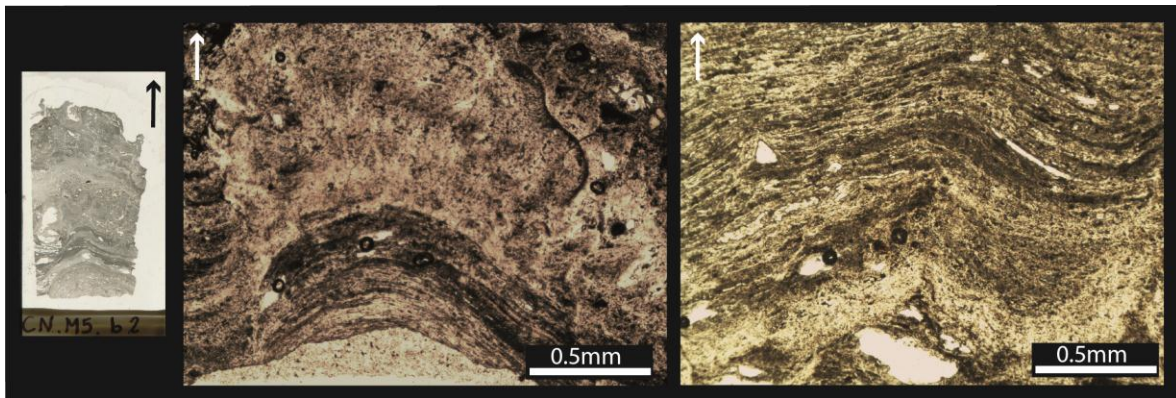

Figure III.7. Photomicrographs of sample M3B thin section under transmitted light. The thin section is approximately vertical and the black arrow indicate the upwards direction.

Sample M6.4

Sinter deposit is formed by continuous, discontinuous sometimes convoluted laminations. They show light brown to dark brown and orange coloration. Silica ~0.1 mm diameter oncoids are identified between silica laminations. Incipient columns/spicules are common at the center of the deposit although the surface of and upper most part is massive (Figure III.8.).
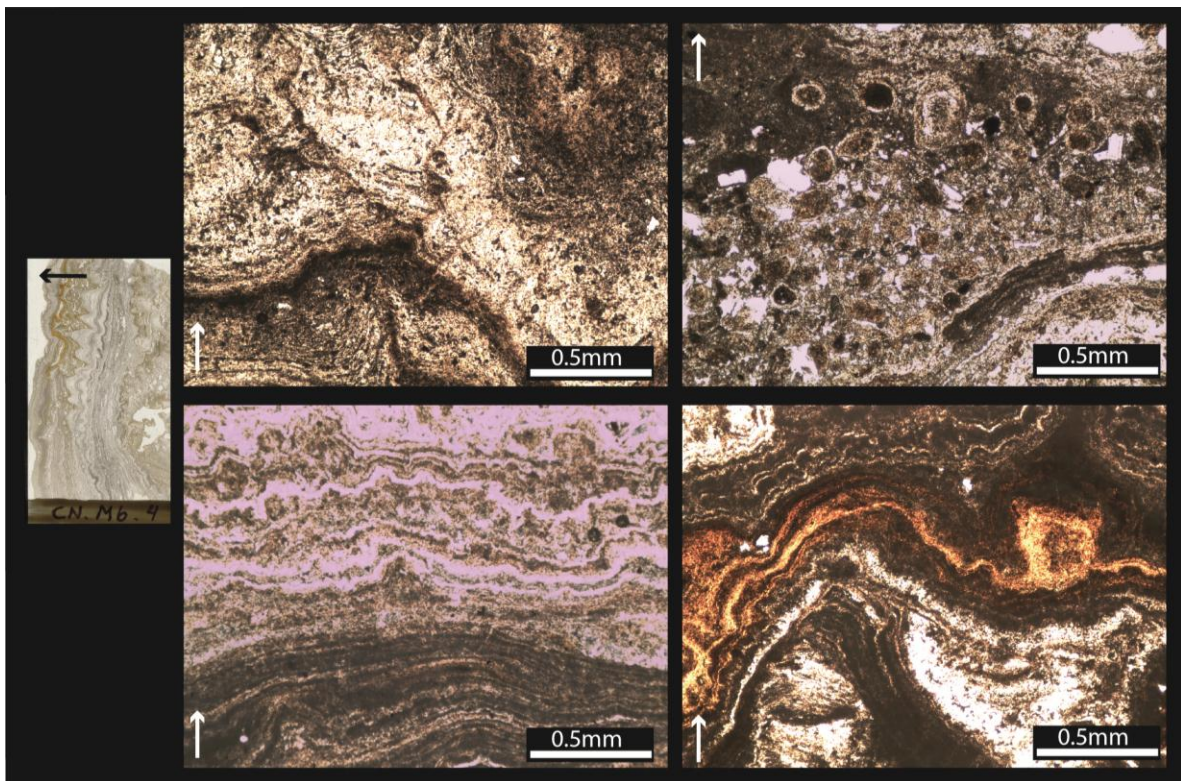
Figure III.8. Photomicrographs of sample M3B thin section under transmitted light. The thin section is approximately vertical and the black arrow indicate the upwards direction.

APPENDIX IV: Sampling sites and SEM samples characterization

Site 2

Location: 601057E/7529545N

Site description: The feature is an eruptive boiling pool. Water discharges through a NW oriented fracture, its temperature is 86.1 °C and pH is 7.4.
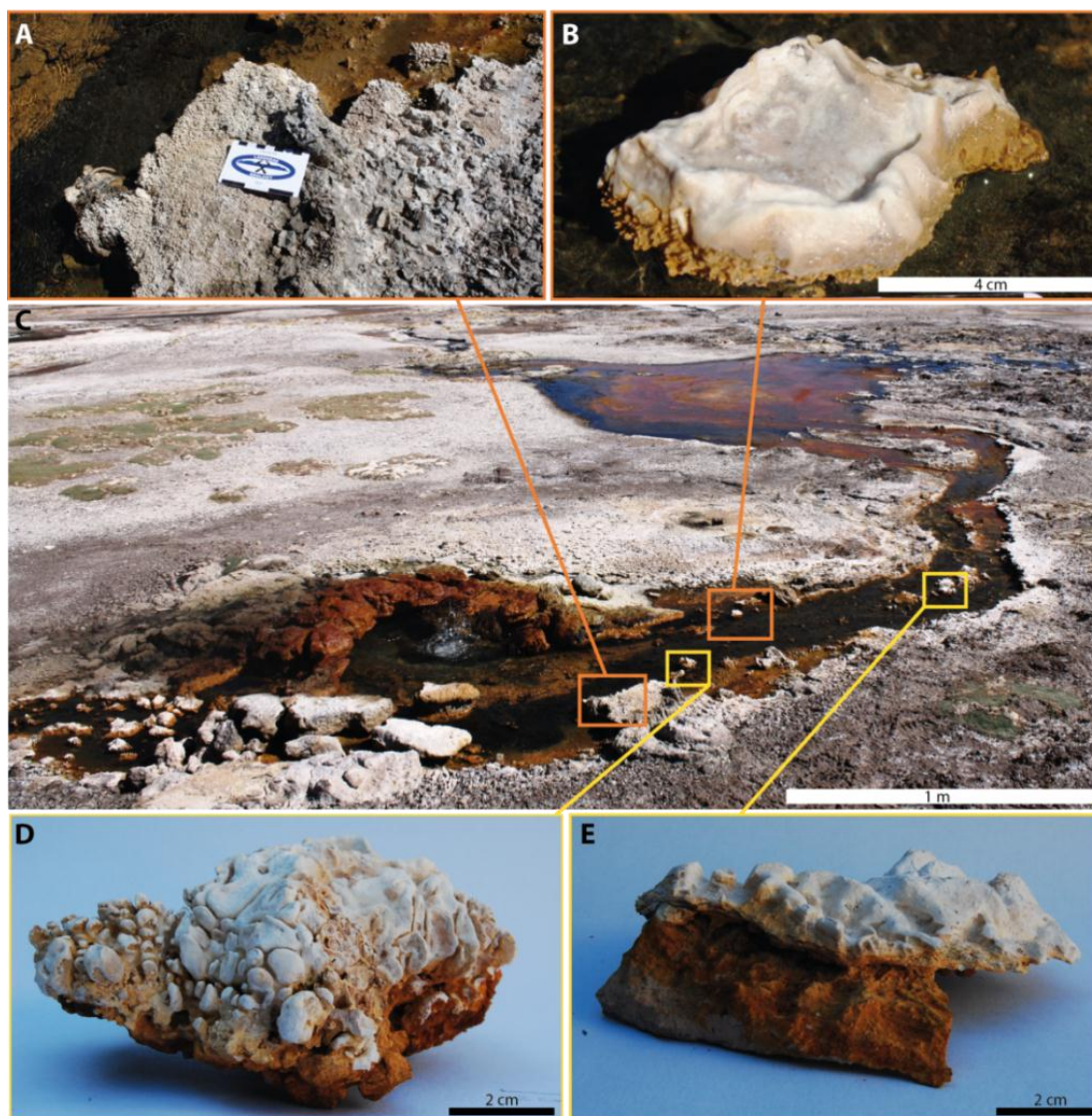

Figure IV.1. Site 2: Eruptive boiling pool with two discharge channels. A: columnar texture on the pool rim. B: sinter island with cup-like rims. C: Site 2 overview and samples location. D: Sample M2.1, it corresponds to a sinter island that shows columns and ranges. E: Sample M2.3, it correspond to a sinter island that show lily-pad texture and horizontal laminations.

The pool discharges into two channels with opposed direction. One of them diffusely flows because of artificial blocking. The other one is well defined with sinter rims that show digitate texture and have a sandy bottom. Sinter islands form in this channel over rock fragments. They show columnar texture when located near the vent, and lily-pad

texture, cup-like shapes or horizontal laminations when situated more distant from the vent (Figure IV.1). Silica oncoids are observed in areas adjacent to the hot pool and discharge channel.

At this site, two samples were taken, one from the near vent area in the discharge channel and the other from the discharge channel, 1.5 m away from the pool.

Sample M2.1

Macroscopic description: Sample corresponds to a small sinter island located in the discharge channel, near the vent. The island is constituted by a thin, laminated sinter deposit over a tuff boulder. Sinter deposit shows columnar texture, with convex laminations inside columns. Merged columns are present in the upper part of the boulder. The color of the sinter deposit varies from yellowish at the base to white at the top (Figure IV.1D).

SEM characterization: A finely convex laminated sinter composed by convex massive and porous layers, formed by coalesced smooth rounded opal-A spheres (Figure IV.2). Massive layers are 1-2 μm in width and show smooth surfaces (Figure IV.2B, C); porous layers are 2-30 μm in width (Figure IV.2C, D), their porosity is given by the void space between opal-A spheres. Opal-A spheres are usually 0.15-5 μm in diameter (Figure IV.2A). At the surface of the sinter deposit, silica platelets can be identified, they are formed by broken silica layers usually are cemented together (Figure IV.2E). The surface of the column top is constituted by smooth massive layers, and shows a soft depression at the center, where aggregated opal-A spheres and opal-A platelets form ridges. Gypsum crystals are found on column top, embedded into silica layers.
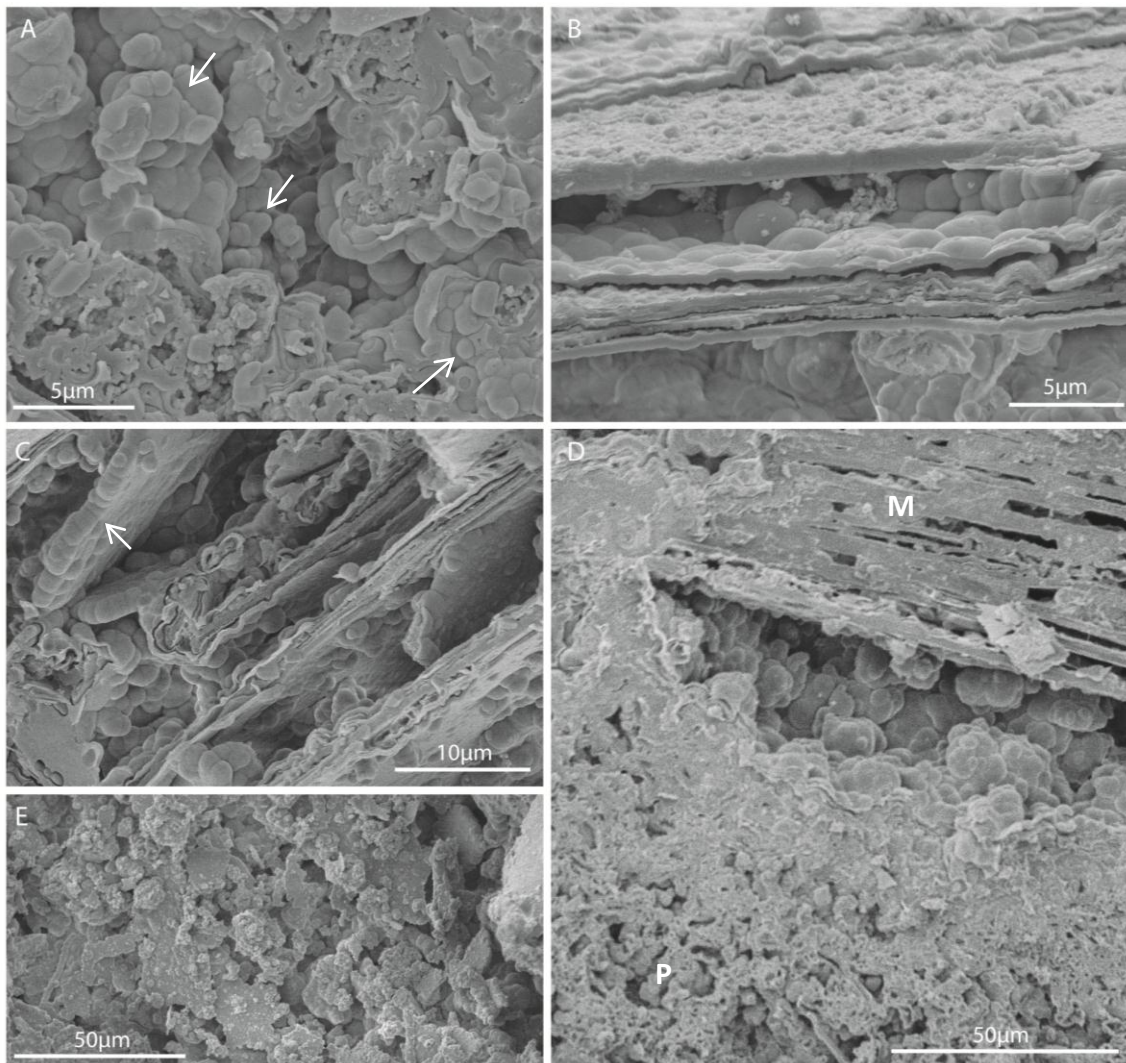
Biotic components: Not found.

Figure IV.2. SEM images show the main micro-textures and silica morphology of sample M2.1. A: Aggregates of smooth opal-A spheres (arrows). B: Massive and porous silica layers formed by coalesced smooth opal-A spheres. C: Coalesced opal-A spheres forming layers (the arrow indicates an individual silica layer formed by opal-A spheres). D: overview of massive (M) and porous (P) silica layers. Massive thin silica laminations also show porosity due to void spaces between them. E: Silica platelets deposited pseudo-horizontally in the uppermost sinter surface.

Sample M2.3

Macroscopic description: Sample corresponds to a small sinter island in the discharge channel, located a couple of meters away from the vent. White fragile sinter grows over lithic substrate and shows digitate texture and fine horizontal laminations.

SEM characterization: Laminated sinter deposit is built over lithic or crystal fragments and is formed by massive 0.2-30 μm width layers and porous 10-100 μm width layers (Figure IV.3E). At a micro scale, layers are approximately horizontal, with small irregularities. Porous layers are sometimes formed by coalesced smooth ~8 μm diameter opal-A spheres (Figure IV.3A, B and C) and others by microbial filaments replaced by

0.3-0.6 μm diameter opal-A spheres (Figure IV.3C-D). The contact between massive and porous layers is usually sharp and planar. Halite crystals are common and occur over massive silica layers (Figure IV.3D).
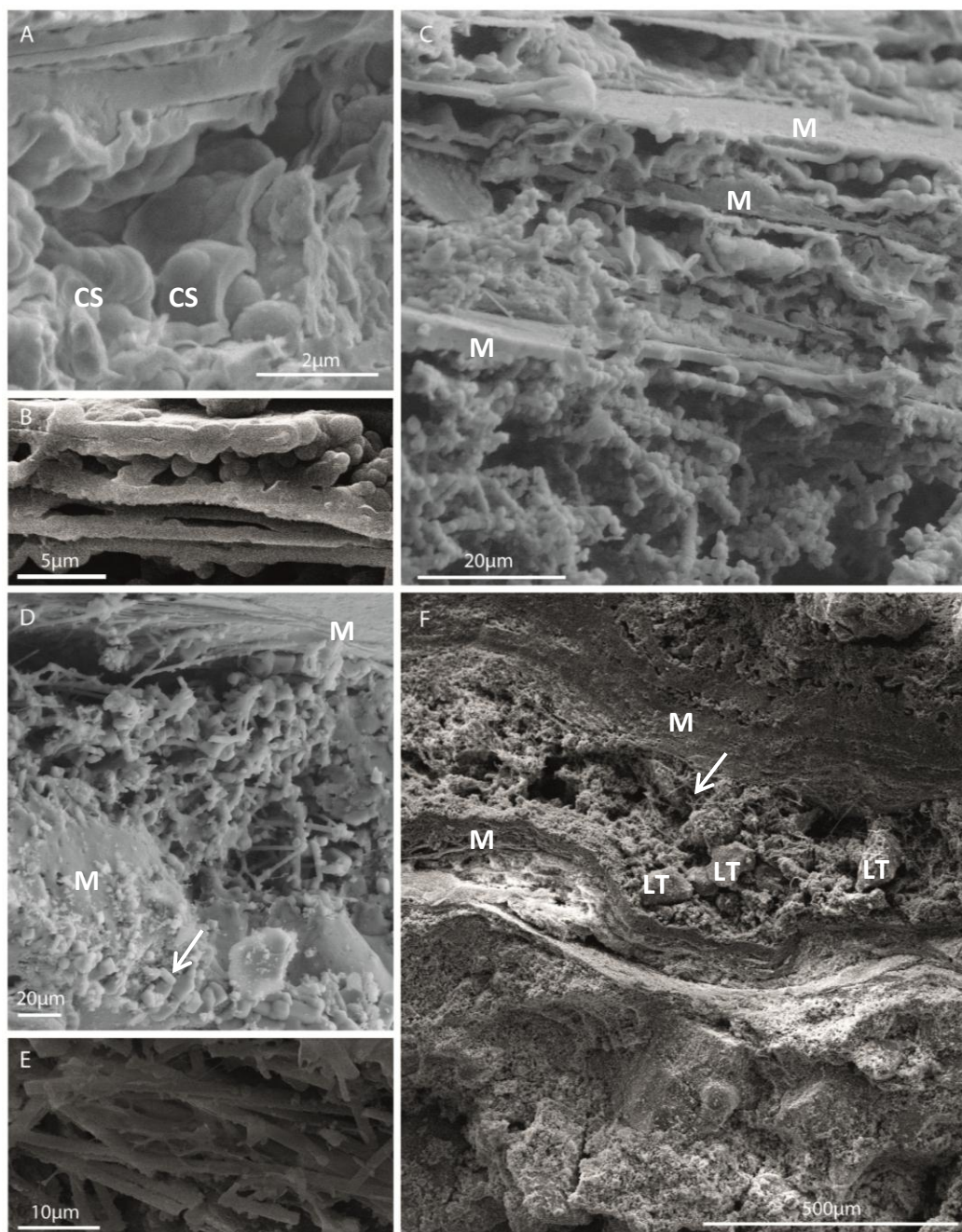

Figure IV.3. SEM images show the main micro-textures and silica morphology of sample M2.3. A-B: Coalesced smooth opal-A spheres (CS) forming silica layers. C: Porous microbe-rich layers (P) and massive silica layers (M). D: Microbial filaments between two massive silica layers (M). The arrow indicates cubic halite crystals. E: Oriented microbial filaments. F: overview of lithic (LT) and microbe-rich layer between massive silica layers (M). The arrow indicates ~2 μm diameter microbes.

Biotic components: tubular microbial filaments are usually ~2.5 μm diameter they occur in porous layers, and are randomly oriented forming networks (Figure IV.3C, D and E).

Site 3

Location: 601023E/7529497N

Site description: The feature is a bubbling hot pool that discharges on only one well defined channel that opens up at 6m length and then forms sinter terraces a few centimeters high (Figure IV.4D). Pool water temperature is 82.3 °C and pH is 6.5. Gas bubbles are observed in the pool and emerging from the rim in the discharge channel.
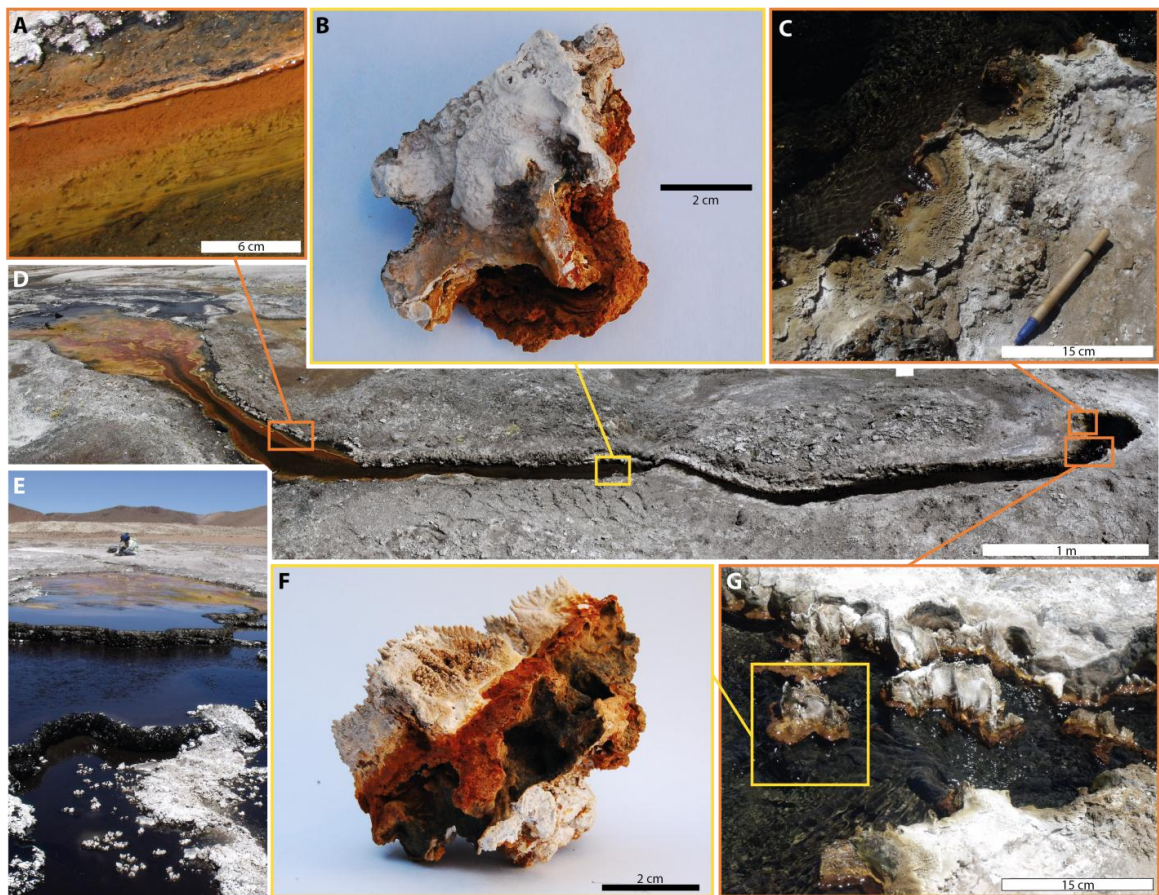

Figure IV.4. Site3: Bubbling hot pool with one well defined discharge cannel. A: Discharge channel where green colored streamers thrive in ~70°C water. B: Sample M3.2, taken from the channel rim; it shows laminations and red colored crust in water-air interface. C: Sinter with splash texture formed in the pool rim (~82°C water). D: General view of site 3. G: Distal area, where palisade (black microbial mats) thrives and sinter terracettes form. F: Sample M3; it corresponds to a sinter island at the beginning of the discharge channel, it shows spicular texture and red coloration at the water-air interface. G: Beginning of the discharge channel, where sample M3.2 was taken from.

Sinter deposit is white-gray in general, shows digitate lily-pad texture on pool rim and near vent discharge channel rim (Figure IV.4C, G). White fragile salty crusts are present in near pool overflow areas. The channel has a sandy bottom and begins with clear

water. Four meters away from the pool, the channel broadens and orange microbial mats begin to develop, streamers are present in the center of the channel (Figure IV.4A) while orange and green bubble-mats develop around them. Further away appears black microbial mat forming sinter terraces where unsilicified grass grows (Figure IV.4E).

In this site, two samples were taken, one from near vent area at the beginning of the discharge channel and the other from the discharge channel rim, about 3.5 m away from the pool.

Sample M3

Macroscopic description: Sample is a small sinter island located at the beginning of the discharge channel (Figure IV.4G). White to tan sinter spicules forming ranges develop above water level (Figure IV.4F). Spicules show internal convex laminations. At water-air interface, a red crust covers white sinter. In sub aqueous areas, the island is composed by <1 mm thick, convoluted laminations of white hard sinter and friable reddish brown and dark green material, the outer surface is dark green and shows nodules.

SEM characterization: The spicule surface shows ~10 µm width radiating columns (Figure IV.5A). White spicules show silicified microbial filaments (Figure IV.5B-C) it heir surface, and are composed of 5-10 µm width aggregates formed by merged opal-A spheres (Figure IV.5E and I). Opal-A spheres are 0.5-3 µm diameter. Prismatic gypsum crystals are present on top of the spicules and have radiating morphologies (Figure IV.5D and E). Blocky 0.5-3 µm size halite crystals occur on the sinter surface (Figure IV.5E). The internal structure of the spicules is formed by intercalations of porous (usually microbial rich) layers and massive silica layers (Figure IV.5B). One continuous layer formed by tetrahedral Ca and As crystals is identified (Figure IV.5G). Some tetrahedral crystals show etched pits although others are in more advanced stages of dissolution. Dissolved tetrahedral crystals are found forming spicule layers. Reddish brown laminations are composed of Si, As and Fe-rich bladed crystals that usually form spherical flower-like aggregates (Figure IV.5H).

Biotic components: 0.8-3 μm diameter microbial filaments replaced by smooth 0.5 μm diameter opal-A spheres are present in spicule surface and in spicule internal laminations (Figure IV.5B-C).
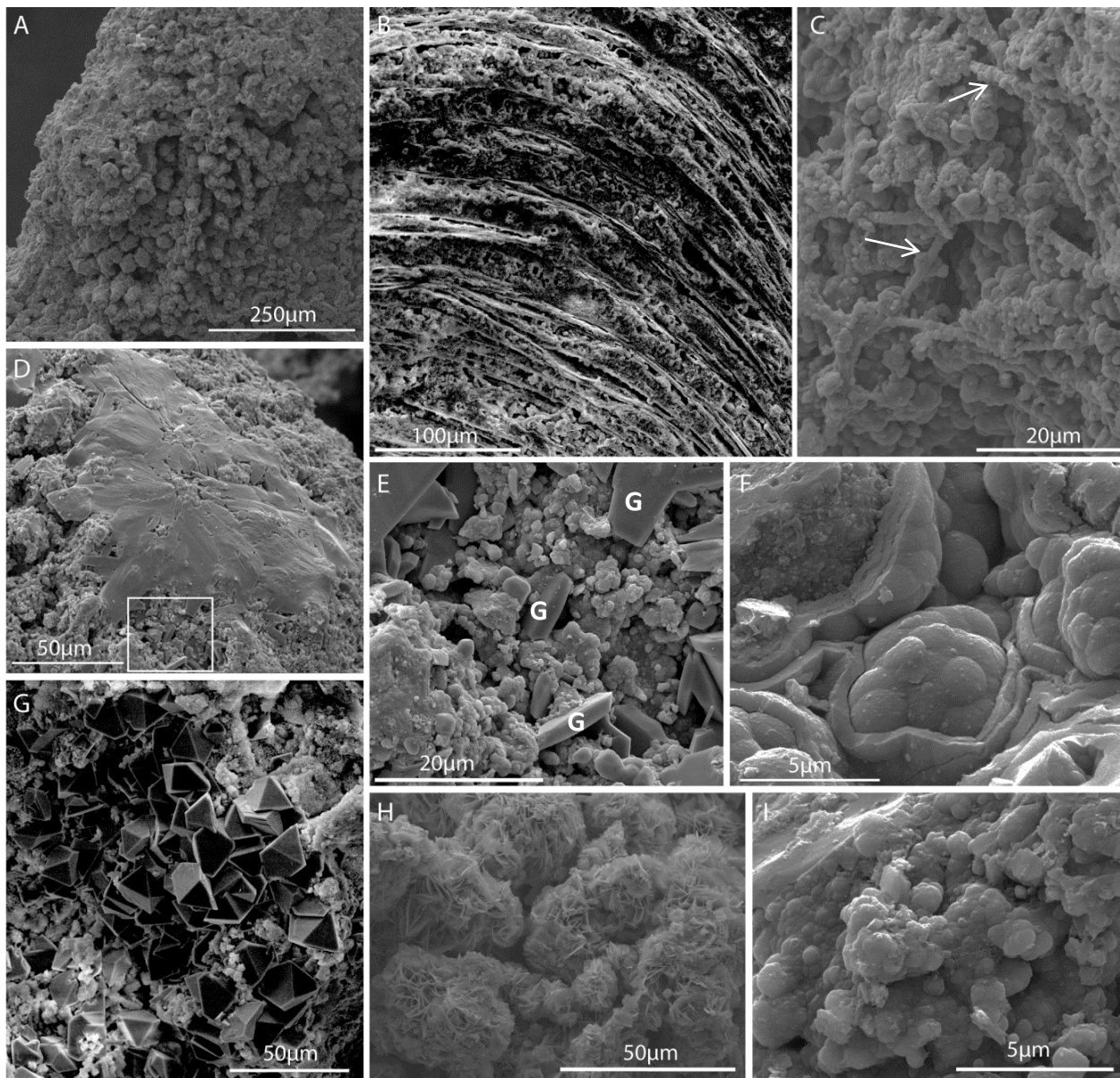

Figure IV.5. SEM images show the main micro-textures and silica morphology of sample M3. A: Micro-columns formed at the surface of sinter deposit. B: Spicule internal laminations that show opal-A spheres between them. C: Silicified microbial filaments (arrows) at the surface of sinter deposit. D: gypsum crystals at the top of a spicule. The white box indicates the location of (E). E: Gypsum crystals (G) and opal-A spheres simultaneously precipitated, close up form (D). F and I: coalesced opal-A spheres. G: tetrahedral crystals (cahnite) horizon between silica laminations in a spicule. H: Flower-like crystals-rich horizon.

Sample M3.2

Macroscopic description: Sample is taken from the discharge channel rim, from a non-splashing, fast flowing area. Sample corresponds to a thin layered friable white sinter rim, and show rare spicules on the surface. At water-air interface, a red crust develops over white sinter (Figure IV.6G).

SEM characterization: Sinter is mainly composed of merged opal-A spheres (0.2-1 μm diameter) that form bumpy microspheres 3-5 μm diameter (Figure IV.6J). Smooth rounded opal-A spheres (0.2 μm diameter) are found replacing microbial filaments and plant material. Sinter is composed by massive layers and porous layers. Massive layers are formed by merged opal-A spheres and typically thinner than porous layers; individual massive layers are usually 0.3 μm in diameter (Figure IV.6H). Porous layers are rich in microbial filaments and are usually thicker, with 100 μm in diameter. Sinter deposit is constructed over lithic or mineral fragments colonized by filamentous microbes, and lithic- and microbe-rich layers are common inside the deposit (Figure IV.6A). Blocky halite crystals with 0.04-2.2 μm side are common within the deposit (Figure IV.6I). Smooth rounded 0.5-1 μm diameter silica spheres are found deposited over coalesced spheres or massive sinter is common (Figure IV.6G), and smaller 0.1μm silica spheres are found filling primary porosity spaces.

Biotic components: microbial filaments encrusted by 0.15-0.22 μm diameter silica spheres, can be found aligned, parallel to each other (Figure IV.6C) or randomly oriented, forming networks (Figure IV.6B). Thin microbial filaments (0.6-1.5 μm diameter) occur randomly oriented or aligned parallel to each other, whereas thicker microbial filaments (~10 μm diameter) usually occur aligned parallel to each other (Figure IV.6D). Plant material casts are found between laminations, and are partially infilled by smooth 0.15 μm diameter silica spheres. Silicified 2 μm diameter pollen spores and spore casts are abundant in one massive sinter layer (Figure IV.6E).
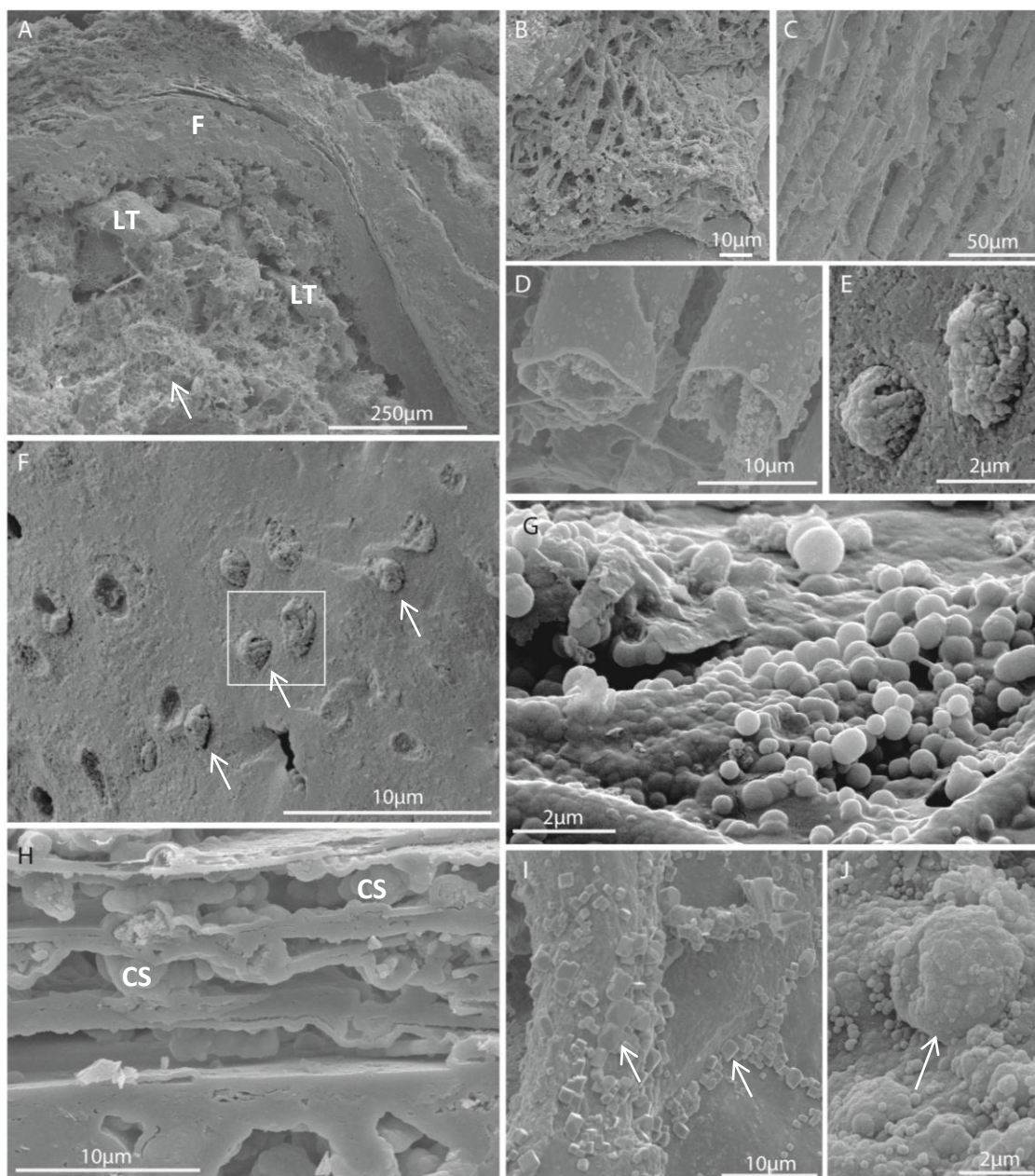
Figure IV.6. SEM images show the main micro-textures and silica morphology of sample M3.2. A: Massive convex silica layer (M) over lithic- (LT) and microbe-rich (arrow) layer (~1 μm diameter). B: Randomly oriented microbial filaments. C Aligned microbial filaments. D: ~10 μm diameter microbial filaments. E: Silicified pollen particles. F: overview of massive silica layer with encrusted pollen particles (Po). Boxed area corresponds to (E). G: Newly deposited opal-A spheres. H: coalesced opal-A spheres (CS) forming massive silica laminations. I: halite crystals (arrows). J: 3μm diameter bumpy microspheres.

Site 4

Location: 601932E/7530315N

Site description: The feature is an eruptive cyclic boiling pool (Figure IV.7). The cycle begins with no water inside the pool, water level starts rising slowly until the pool is filled to the top and then water level descends again leaving the pool completely dry

again. When the pool is empty steam comes out through the vent, and when it is full, water is vigorously boiling and splashing the nearest areas. Cycle duration is approximately 5 minutes. Water temperature in the pool is 82.7 °C and its pH is 7.3. The associated sinter deposit is white colored and shows columnar texture over the walls of the pool, and in near vent areas. Columnar sinter texture occurs in near vent areas (Figure IV.7E). Further away from the vent, the sinter deposit is massive with low ridges and laminations over a horizontal area next to the pool (Figure IV.7D). At this site, two samples were taken, one from the vent wall and the other from the flat area further away from the vent.

Figure IV.7. Site 4: Cyclic boiling pool. A: Site 4 actively boiling pool and full of water. B: Site 4 pool overview and samples location; picture shows the moment when the pool is almost completely dry. C: Columnar texture occurring in vertical walls of the pool. D: Sample M4.1 shows horizontal laminations and low ridges. E: Sample M4.2 shows porous columnar textures.

Sample M4.1

Macroscopic description: Sample is taken from the vent rim, 50 cm away from the vent. Sample corresponds to white porous laminated sinter that shows incipient terracettes on the upper surface (Figure IV.7D).

SEM characterization: Sinter deposit is formed by massive and porous layers (Figure IV.8A). Massive layers are formed by coalesced 0.2-1 µm diameter opal-A spheres (Figure IV.8C). Abundant lithic fragments are found between laminations, and at the base and top of the deposit (Figure IV.8B), crystal fragments are found coated by silica and encrusted in massive layers (Figure IV.8E)
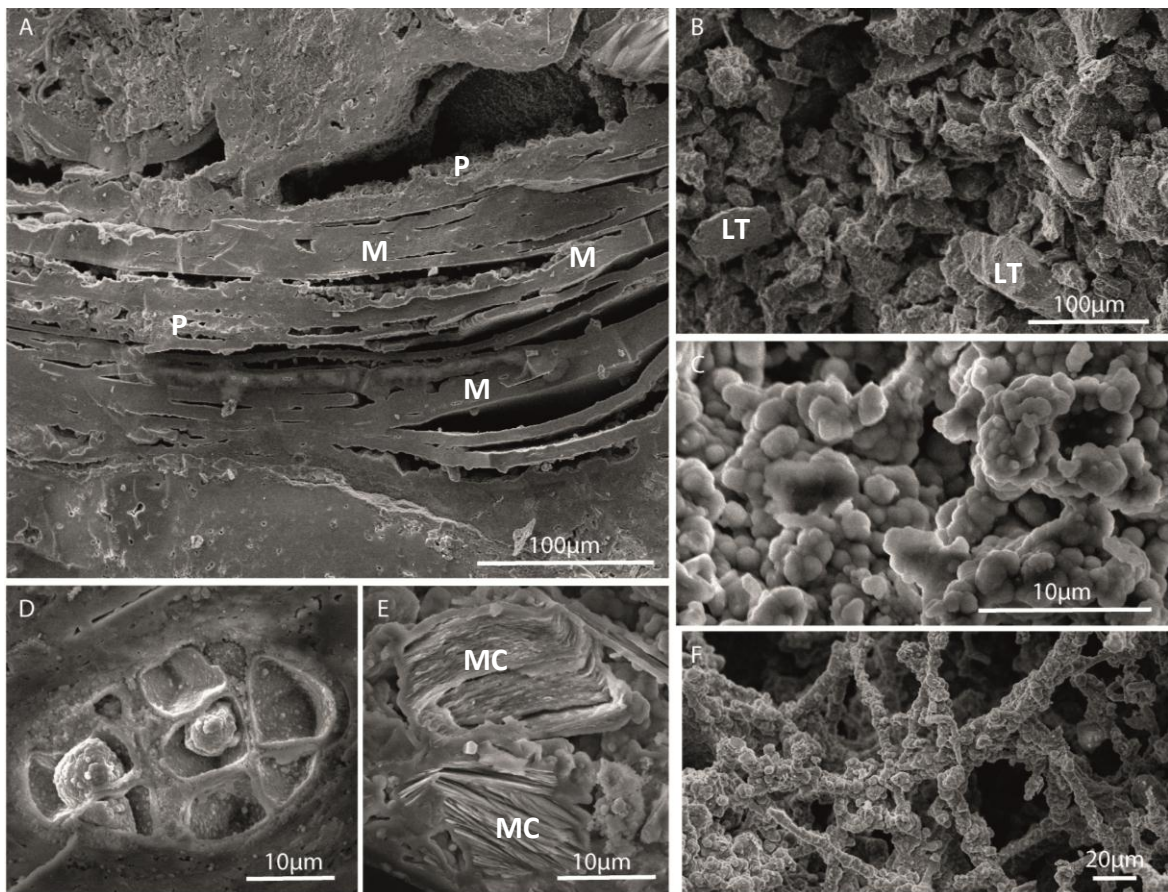
Figure IV.8. SEM images show the main micro-textures and silica morphology of sample M4.1. A: Overview of massive (M) and porous (P) silica layers. B: Lithic fragments (LT) coated by silica precipitate. C: Coalesced opal-A spheres. D: Silicified pollen particles. E: Mica crystals (MC) coated by massive silica. F: Silicified 2.5 µm diameter filamentous microbes.

Biotic components: 2.5 µm diameter microbial filaments are found in sinter laminations, organized randomly oriented, forming networks, these filaments are usually encrusted

by smooth ~0.2 μm diameter opal-A spheres (Figure IV.8F). Another group of 4-5 μm diameter spheres is recognized on the surfaces of massive laminations. Pollen particles are also found (Figure IV.8D).

Sample M4.2

Macroscopic description: Sample is taken from the vent rim, in a splashing zone. Sample corresponds to white sinter composed of columns that are up to 1cm high, usually <0.5 cm in diameter, their surface show ridges and pits, usually each column displays a central pit at column top. Columns are made of vitreous convex laminations; a vertical profile shows several layers of vitreous white to transparent laminated columns at the base, followed by continuous layers of opaque cream vitreous laminations at the top.

SEM characterization: Columns interior is formed by concentric massive opal-A layers 0.3 mm in thickness. Columns surface shows coalesced 1-5 μm diameter opal-A spheres (Figure IV.9C, F) that form isolated 20-30 μm diameter columns and merged columns that form ranges (Figure IV.9A, B).

The surface of macroscopic columns vertical sides also show radiating 200 μm high and 100μm diameter columns, that narrow towards the top (Figure IV.9E). Concentric radiating elongated gypsum crystals are found at the top of the columns (Figure IV.9G). Halite crusts show cubic cleavage and occur on the column surface, over silica spheres (Figure IV.9D).

Biotic components: Silicified pollen spores and plant material (Figure IV.9H, I) are found in columns surface.
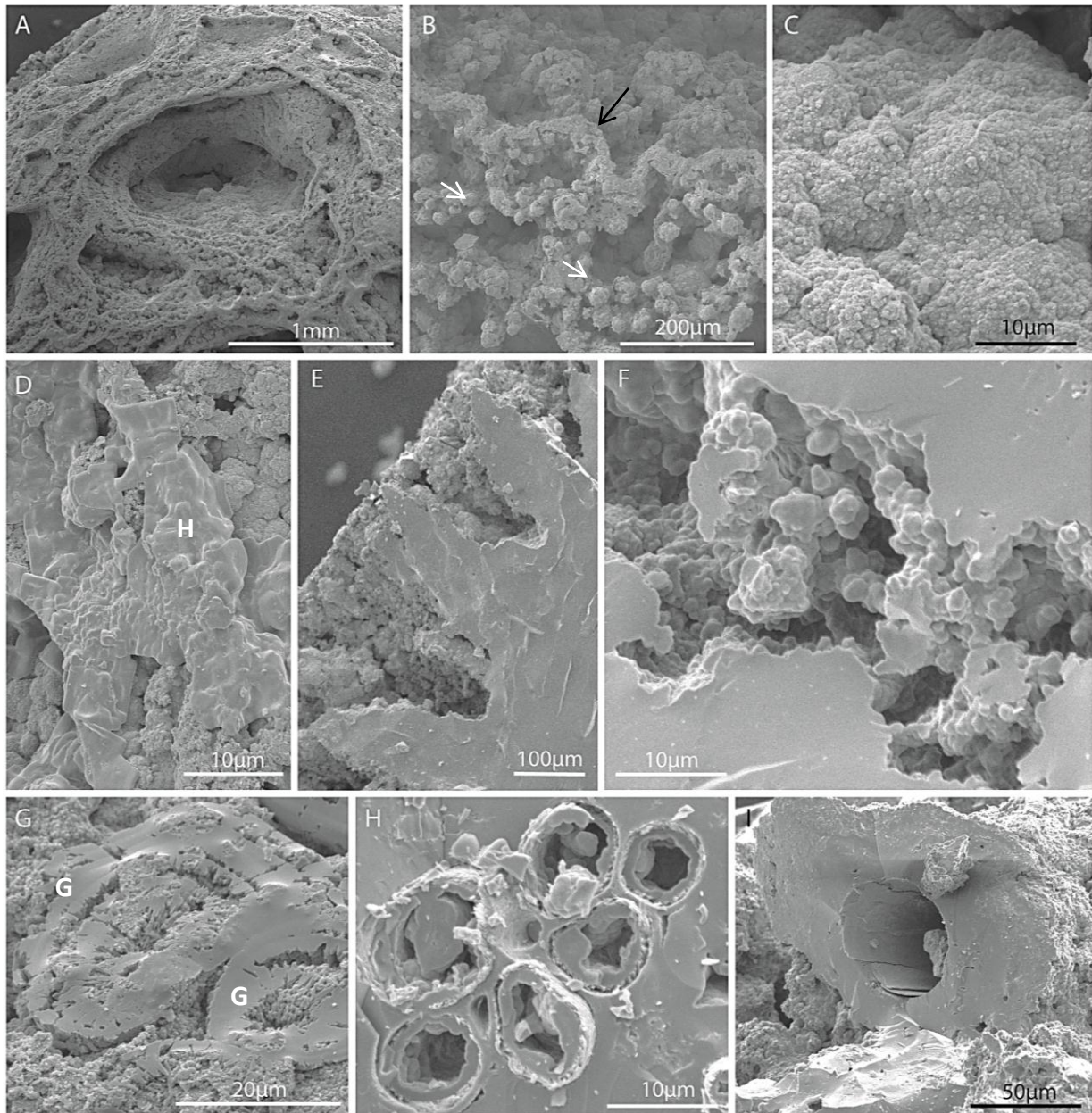
Figure IV.9. SEM images show the main micro-textures and silica morphology of sample M4.2. A: Column surfaces showing ridges and a central pit. B: Ridges (black arrow) and micro-columns (white arrows) at the surface of a macro column. C: Coalesced opal-A spheres forming a massive deposit. D: Halite crust (H) at the surface of a column. E: Radiating micro-columns at the side of a macro-column. F: Coalesced opal-A spheres forming the massive sinter deposit. G: Concentric radiating elongated gypsum crystals (G). H, I: Plant material incorporated in the sinter column.

Site 5

Location: 602406E/7530528N

Site description: The feature is a non-boiling, non-bubbling, non-surging hot pool. The temperature of the water is 76.9 °C and the pH is 7.1.

Figure IV.10. Site 5: Quiet non-boiling pool. A: Silicification of plant material (arrow). B: Digitate lily-pad texture on the pool rim (arrows). C: Site 5 ov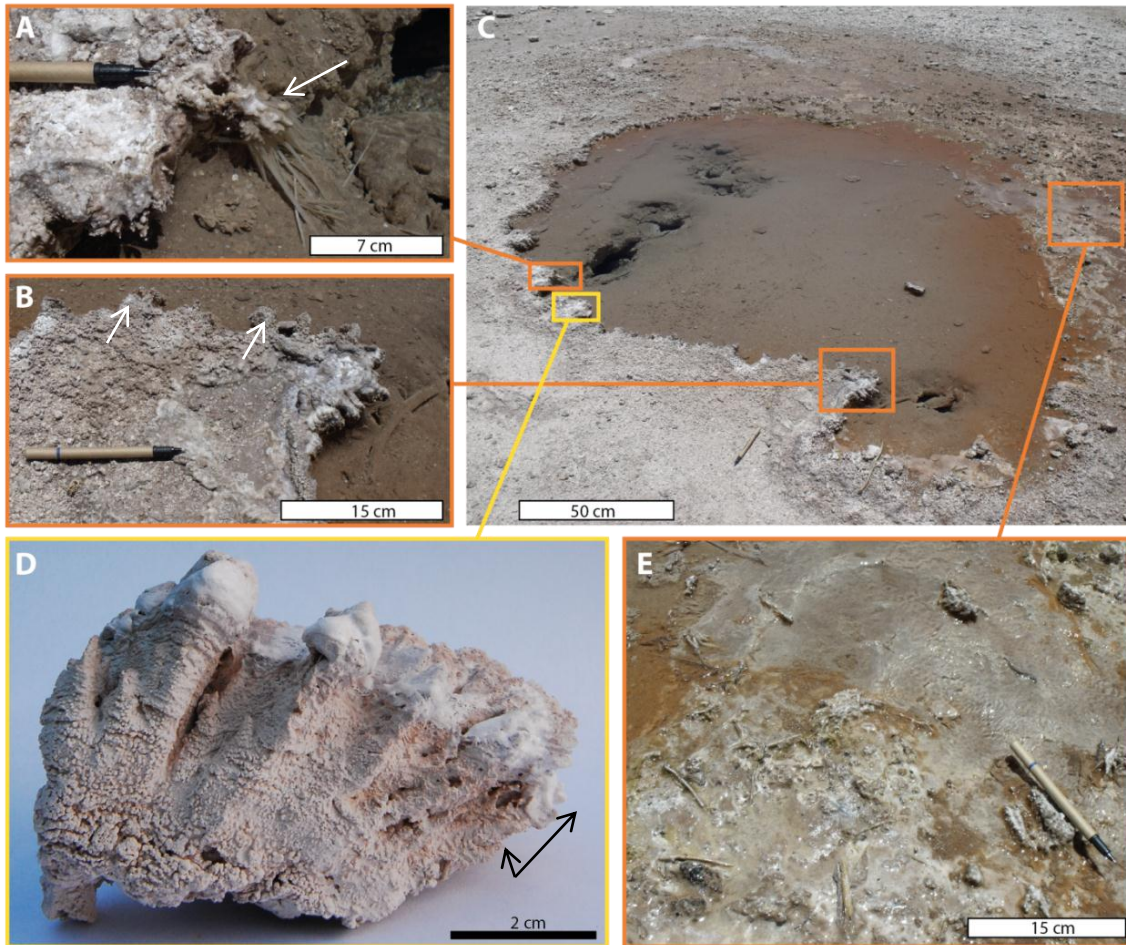erview and samples location. D: Sample M5; it was taken from the pool rim and show digitate lily-pad texture (the larger arrow indicates the upwards direction, while the smaller arrow indicates the poolwards). E: Overflowing area with terracettes and silicified plant material.

A white sinter deposit forms a digitate lily-pad rim at one side of the pool, while water flows through the other side forming a silicified crust with terracettes, sinter islands, and silica oncoids further away. Abundant plant material grows around the pool and is partially silicified when in contact with water (Figure IV.10).

Sample M5

Macroscopic description: Sample is taken from the digitate lily-pad pool rim. Sample corresponds to white vitreous sinter that shows spicular and digitate lily-pad textures. The growth of sinter deposit by laminae stacking is both horizontal, towards the pool, and vertical, increasing the height of the spicules and ranges. Thinner spicules grow in

sub-aquatic areas. Thin laminations occur at the base of the sinter deposit. Internal laminations are gray and white; ranges and spicules show convex laminations.

SEM characterization: Spicules are built by coalesced 0.2-1 µm diameter opal-A spheres, silica platelets (Figure IV.11F, G) and silicified microbial filaments. Macroscopic spicules have a rough, not smooth surface, with micro-spicules and ranges (Figure IV.11A); unlike columns in sample M4.2, no pits were identified. Abundant halite crusts that show cubic cleavage (Figure IV.11J) and scarce prismatic gypsum crystals occur on the surface of the spicule.

Pool-wards laminations are composed of 2-3.3 µm width massive layers and 2 to >200 µm width porous layers (Figure IV.11B). Massive layers are formed by merged opal-A spheres that are 1-1.5 µm in diameter (Figure IV.11D), and are usually less abundant and thinner than porous layers. Porous layers are formed by a network of microbial filaments, and are usually thicker and much more abundant (Figure IV.11E).

Biotic components: 1.5 µm diameter microbial filaments are found on spicule surface, forming networks (Figure IV.11E); ~ 1 µm diameter filaments occur inside massive silica layer and in porous filament-rich layers, forming networks. Filaments are usually encrusted by smooth ~ 0.2 µm diameter opal-A spheres.
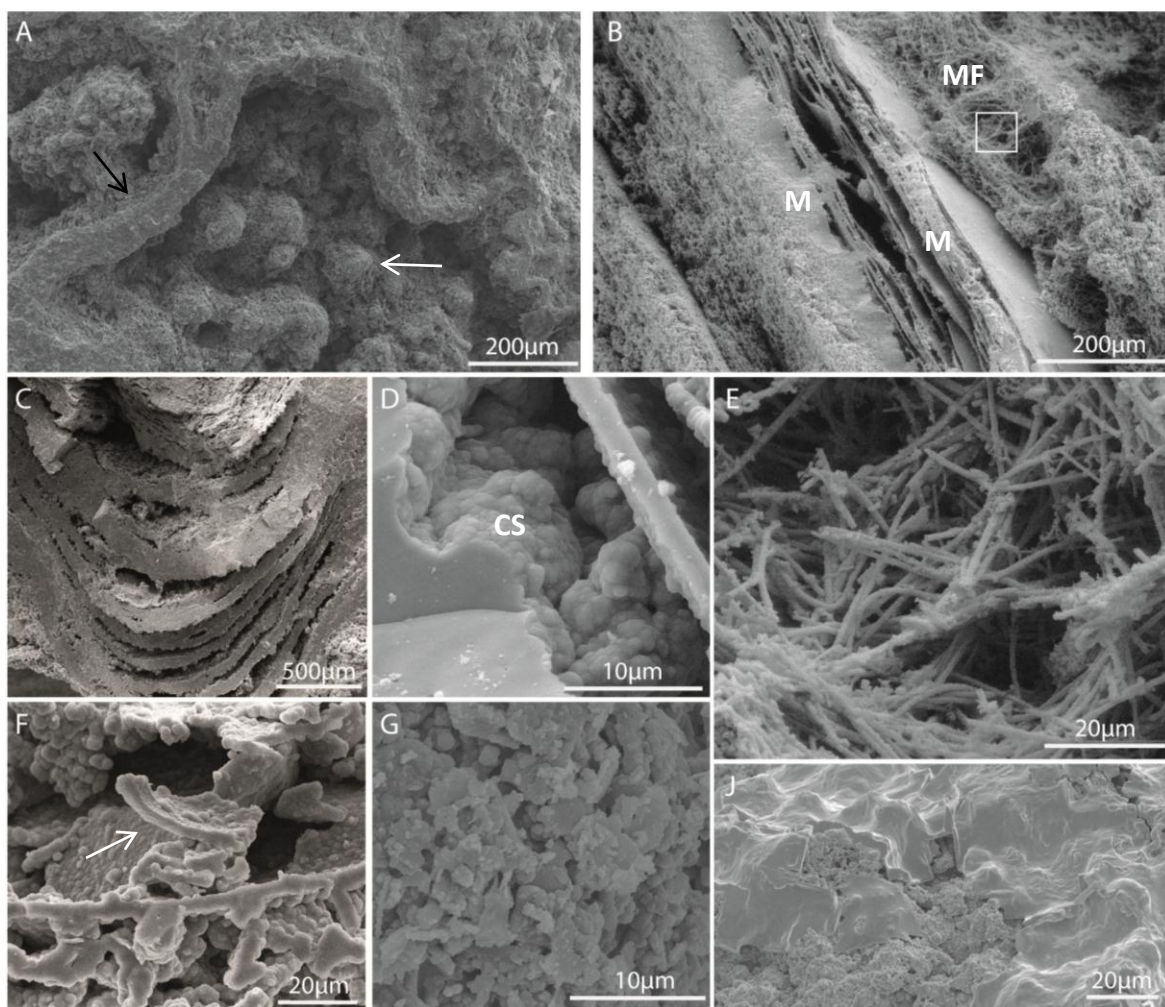
Figure IV.11. SEM images show the main micro-textures and silica morphology of sample M5. A: Overview of the surface of a spicule; micro-spicules (white arrow) and ridges (black arrow) can be identified. B: Microbial filament-rich layers (MF) and massive silica layers (M) in the poolwards laminations. White box indicate the area of (E) C: Concave laminations between two spicules; massive layers and porous layers, usually with no microbes. D: Coalesced opal-A spheres (CS) forming massive silica layers. E: Detail of the ~1 μm diameter microbial filaments from B. F and G: Silica platelets (arrow): J: halite crust at the surface of sinter deposit.

Site 6

Location: 601730E/7528814N

Site description: The feature is a vigorously boiling and bubbling pool that discharges into one well defined channel. Water temperature in the pool is 87.6 °C and its pH is 7.5. Sinter deposit forms a rim around the pool and the discharge channel that show columnar/spicular texture in near vent areas and lily-pad on pool rims. Terracettes form in overflowing areas. Sinter coloration is black in sub-aquatic areas, red in water-air interface and tan in sub-aerial areas (Figure IV.12). In this site, four sinter samples are taken from the pool rim.
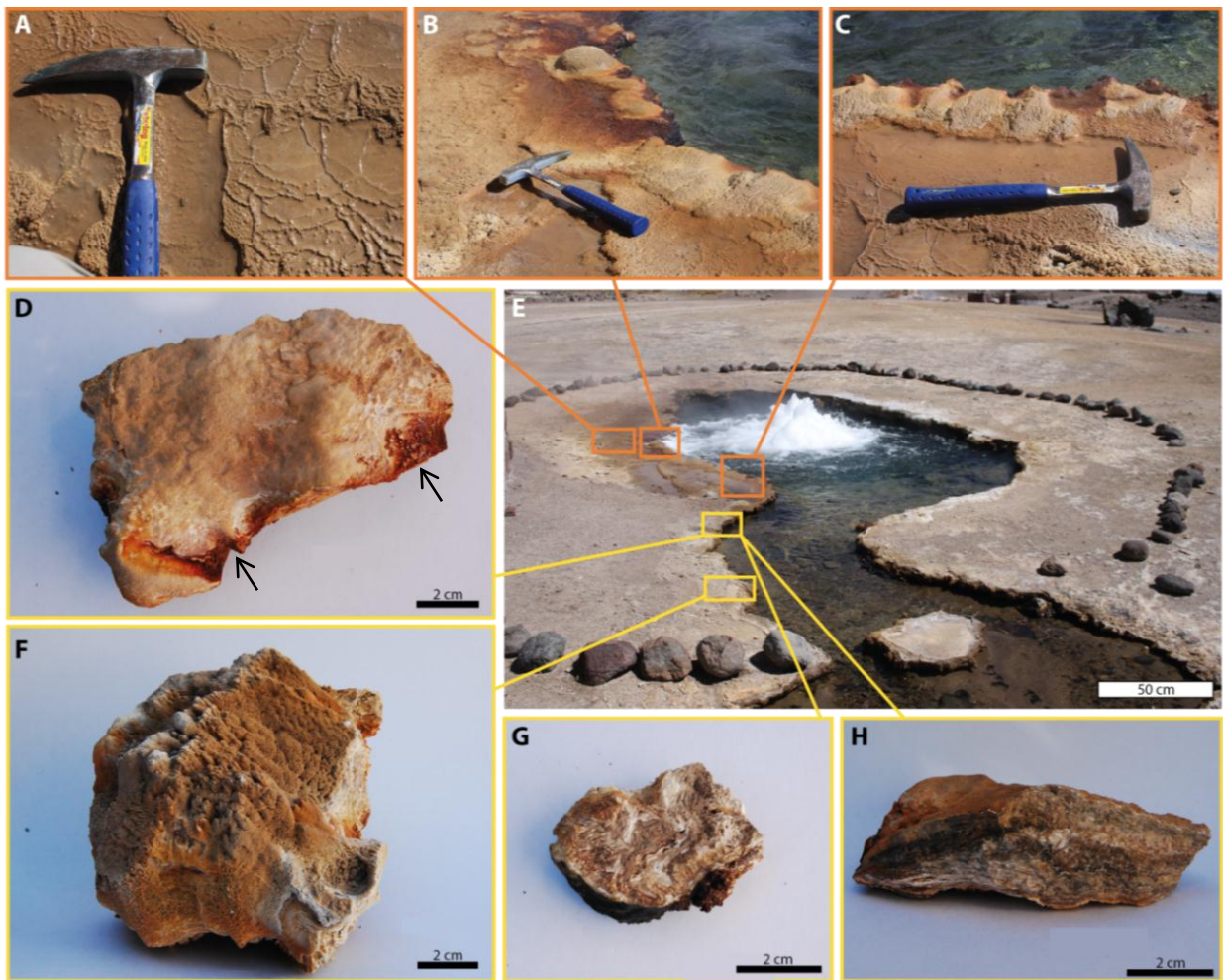
Figure IV.12. Site 6: Vigorously boiling and bubbling pool with reddish and brown sinter deposit. A: Terracettes that form in overflow areas. B and C: Sinter pool rim with columnar splash texture. D: Sample M6.4 that show intense red coloration in the surface at water-air interface (arrows). E: Site 6 overview and samples location. F: Splash texture on the surface of sinter deposit. G: Internal colored laminations of a broken piece of sample M6.4. H: Vitreous horizontal laminations.

Sample M6.4

Macroscopic description: Sample is taken from the pool rim. Sinter shows white, grey, yellow and reddish, irregular, vitreous, <1 mm width laminations. A red crust develops over sinter deposit in water-air interface, while in sub-aquatic areas the crust is black. Millimeter scale high columns occur in sub aquatic areas.

SEM characterization: Black crust and sub-aquatic spicules are made of coalesced rough Si-rich (Figure IV.13B) spheres and As, Si, Ca and Fe-rich spiky spheres (Figure IV.13A). Spiky spheres are ~0.3 µm in diameter and rough spheres are 1.5-6.5 µm in diameter.

Laminations are made of coalesced smooth 1.4-2.3 µm diameter opal-A spheres that form massive layers (Figure IV.13C, D), 1.5-3 µm diameter bumpy opal-A spheres (Figure IV.13E), and flower-like minerals occur in the deposit (Figure IV.13F).
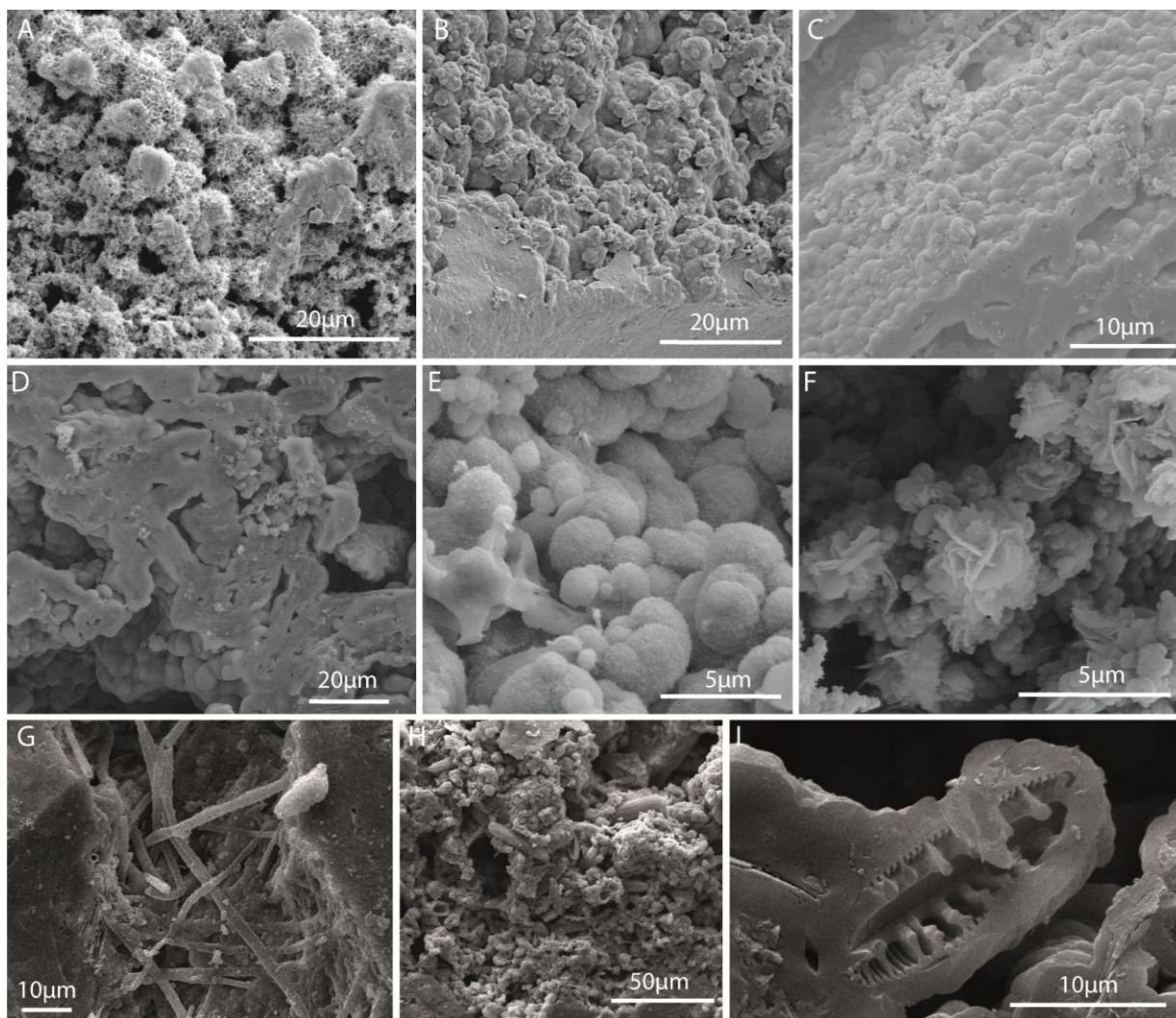
Figure IV.13. SEM images show the main micro-textures and silica morphology of sample M6.4. A: spiky As, Si, Ca, Fe-spheres that occur at the surface of sinter deposit in a sub-aquatic area. B. coalesced rough, not smooth silica-rich spheres that occur in sub-aquatic sinter deposit. C, D and E: coalesced opal-A spheres. F: flower-like aggregates and opal-A spheres. G: microbial filaments. H: Overviewdiatom-rich horizon. I: detail of one diatom.

The deposit is generally massive, with few places where the morphology of constituent phases can be distinguished, although irregular-shaped cavities are common. Cavities can be hollow or filled with different phases: smooth 0.5-1 µm diameter opal-A spheres; parallel-stacked 0.3 µm width, 0.2-3 µm length, lamellar As and Ca-rich crystals ~80 nm width, ~3 µm length acicular radiating crystals; and 5-15 µm width tetrahedral crystals which are usually intergrowth, although one phase cavities can also be recognized.

Massive sinter deposit presents an irregular diatomaceous horizon with abundant diatoms (Figure IV.13H and I) and few places where filamentous microbes can me recognized (Figure IV.13G).

Biotic components: silicified diatoms (Figure IV.13I), and high temperature 3 μm diameter filamentous microbes (Figure IV.13G) are found in the deposit.

APENDIX V. Silica precipitation rate experiment: results, site characterization and setting.

Table V. 1. Silica precipitation rate experiment data

	position	in	out	precipitate weight (mg)	precipitate (mm)	time (months)	precip. per month (mg)	time (days)	precip. per day (mg)
perpendicular to water flow	P1	ene-12	mar-12	52.0	<0.3	2	26.0	68	0.76
	P1	ene-12	oct-12	132.4	1.3	9	14.7	291	0.45
	P1	ene-12	nov-12	207.9	1	10	20.8	322	0.65
	P1	mar-12	nov-12	53.6	0.5	15	3.6	457	0.12
	P2	ene-12	mar-12	68.1	<0.3	2	34.0	68	1.00
	P2	ene-12	oct-12	474.7	2.8	9	52.7	291	1.63
	P2	ene-12	nov-12	798.5	2.8	10	79.9	322	2.48
	P2	mar-12	abr-13	875.1	3	15	58.3	457	1.91
	P3	ene-12	mar-12	66.9	<0.3	2	33.4	68	0.98
	P3	ene-12	oct-12	414.9	2.5	9	46.1	291	1.43
	P3	ene-12	nov-12	136.4	2	10	13.6	322	0.42
	P3	mar-12	abr-13	793.9	2.5	15	52.9	457	1.74
	P4	ene-12	mar-12	42.5	<0.3	2	21.3	68	0.63
	P4	ene-12	oct-12	226.6	1	9	25.2	291	0.78
	P4	ene-12	nov-12	631.4	2.1	10	63.1	322	1.96
	P4	mar-12	abr-13	809.2	2.8	15	53.9	457	1.77
paralel to water flow	P1	ene-12	mar-12	45.6	<0.3	2	22.8	68	0.67
	P1	ene-12	oct-12	247.4	1.8	9	27.5	291	0.85
	P1	ene-12	nov-12	86.4	1.0	10	8.6	322	0.27
	P2	ene-12	mar-12	31.8	<0.3	2	15.9	68	0.47
	P2	ene-12	oct-12	11.2	0.3	9	1.2	291	0.04
	P2	ene-12	nov-12	43.7	<0.3	10	4.4	322	0.14
	P3	ene-12	mar-12	29.2	<0.3	2	14.6	68	0.43
	P3	ene-12	oct-12	117.7	1.5	9	13.1	291	0.40
	P3	ene-12	nov-12	41.8	1.0	10	4.2	322	0.13
	P4	ene-12	mar-12	82.5	<0.3	2	41.3	68	1.21
	P4	ene-12	oct-12	30.4	0.3	9	3.4	291	0.10
	P4	ene-12	nov-12	246.7	0.3	10	24.7	322	0.77

Red values are altered results because of a failure in the experiment development, the glass slides were found out of place.

Site n°3
Date: 17-jan-2012
Altitude:4300 masl
Ambient Temperature: 13.8-14.1°C
Humidity (%): 12.8-14.2
Wind veolcity (m/s): 5.4-8.4
Wind direction: 90E

Table V.2. Site of experiment characterization and environmental conditions

Position	Channel Length (m)	Channel depth - max channel depth (cm)	Channel width (cm)	Wetted area (cm)	Description	Water T (°C)	Wind vel. (min-max) (m/s)	Wind direction	Humidity (%)	Flow rate (m/s)	Evap rate (ml;cm2; min)	Obs
1	0.74	2,0 - 3,6	21	21	well defined channel with sinter rims	72.4	3.7 - 6.3	E 90	64.2 - 89	0.0025	1; 95; 3'04"	T=82,3°C in the pool
2	3.24	2	14	14	well defined channel that narrows in slight curve	66.2	5.1 - 7.2	E 90	124	0.0039	1; 63.6; 4'46"	P1 and P2 evaporation rate experiment done over the channel rim sinter deposit
3	6.84	2	30	51	the channel opens up few centimeters behind	62.7	3.4 - 6.1	E 90	88.9 - 111.7	0.0021	0.5; 16.25; 4'04"	P3 and P4 evaporation rate experiment done over done over a rock
4	9.84	2.5	46	126	streamers in channel center and have broad humid area arround	57.4	4.8 - 7.5	E 90	32 - 45.2	0.0024	0.6; 22.9; 7'09"	